



저작자표시-비영리-변경금지 2.0 대한민국

이용자는 아래의 조건을 따르는 경우에 한하여 자유롭게

- 이 저작물을 복제, 배포, 전송, 전시, 공연 및 방송할 수 있습니다.

다음과 같은 조건을 따라야 합니다:



저작자표시. 귀하는 원저작자를 표시하여야 합니다.



비영리. 귀하는 이 저작물을 영리 목적으로 이용할 수 없습니다.



변경금지. 귀하는 이 저작물을 개작, 변형 또는 가공할 수 없습니다.

- 귀하는, 이 저작물의 재이용이나 배포의 경우, 이 저작물에 적용된 이용허락조건을 명확하게 나타내어야 합니다.
- 저작권자로부터 별도의 허가를 받으면 이러한 조건들은 적용되지 않습니다.

저작권법에 따른 이용자의 권리는 위의 내용에 의하여 영향을 받지 않습니다.

이것은 [이용허락규약\(Legal Code\)](#)을 이해하기 쉽게 요약한 것입니다.

[Disclaimer](#)

**A THESIS**

**FOR THE DEGREE OF DOCTOR OF PHILOSOPHY**

**Dielectric barrier discharge plasma-mediated preparation of metal  
oxide nanostructures for catalytic and biological applications**



**Antony Ananth**

**Major of Energy & Chemical Engineering**

**FACULTY OF APPLIED ENERGY SYSTEM**

**GRADUATE SCHOOL**

**JEJU NATIONAL UNIVERSITY**

**2014. 12**

**Dielectric barrier discharge plasma-mediated preparation of metal oxide nanostructures for catalytic and biological applications**

**Antony Ananth**

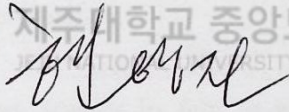
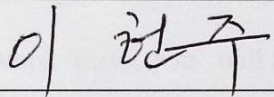
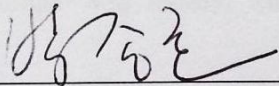
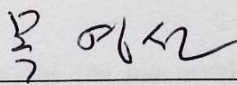
**(Supervised by Professor Dr. Young Sun Mok)**

A thesis submitted in partial fulfillment of the requirement for the degree of

Doctor of Philosophy

2014. 12

This thesis has been examined and approved.

Prof. Dr. Young Jin Hyun Chairman, Thesis Committee Member		Department of Chemical and Biological Engineering, Jeju National University
Prof. Dr. Heon Ju Lee Thesis Committee Member		Department of Energy Engineering, Jeju National University
Dr. Soo-Hyoung Moon Thesis Committee Member		Water Research Center, Jeju Development Corporation
Dr. Jong-Ho Park Thesis Committee Member		Korea Institute of Energy Research
Prof. Young Sun Mok Thesis Committee Member and Supervisor		Department of Chemical and Biological Engineering, Jeju National University

Date:

**Major of Energy & Chemical Engineering  
Plasma Applications Laboratory  
FACULTY OF APPLIED ENERGY SYSTEM  
GRADUATE SCHOOL  
JEJU NATIONAL UNIVERSITY**

## ACKNOWLEDGEMENTS

First and foremost, I thank to the ALMIGHTY for his blessings to carry out the research in this beautiful country. During the ups and downs especially in sickness, he gave me strength and confidence and helped me to overcome the hurdles.

I express my deepest gratitude to my research supervisor Prof. Dr. Young Sun Mok for his excellent guidance, helping tendency at all circumstances and for his student friendly nature. He is a man of inspiration and motivation to approach the life in the most positive ways and to work systematically. I thank Prof. Dr. Hyun and Prof. Sang Baek Lee for their lectures, guidance during conference visits and their ever-loving characters. Dr. M. Sivakumar, Anna University Tiruchirappalli and Dr. G. Arthanareeswaran, NIT Trichy are thanked for their continuous support and personal relationship.

I would like to thank all my friends in Jeju as my living greatly depended on their friendship. Simply saying a word 'thank you' will not be sufficient to them. I remember their great care during my illness and requirements which fills my eyes with tears of gratitude. Mr. Saravanakumar, Mr. Thiyagarajan and family, Mr. Ananthakumar, Dr. Dharaneedharan and family are specially thanked.

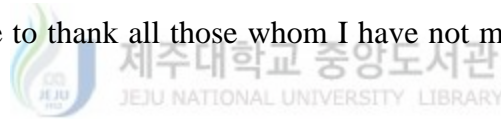
I would like to thank Dr. Gandhi for his invaluable help for the admission in this department and for initial settling. Dr. Karthikeyan and family, Dr. Navaneethan, Dr. Karuppiah and family, Dr. Radhakrishnan, Mr. Alluri, Dr. Saranya, Mr. Ganesh, Mr. Sudhakaran, Mr. Arun, Ms. Sophia, Dr. Umasuthan and family, Ms. Mothi are thanked for their valuable support and friendship.

I feel happy to thank my Korean friends for their lovely nature and creating a lively atmosphere in this laboratory. Dr. Jang Doo Il, Mr. Joe, Mr. Im, Ms. Jwa, Ms. Ko and my Vietnam lab mate Mr. Trinh had created a healthy and positive ambience.

It is my duty to thank the university administration for providing me full tuition fee waiver. I also thank to BK 21 plus fellowship for providing me sufficient funds for my living. I am grateful to the staffs at the research instrumentation center (RIC) in this university for providing the instrument facilities to carry out my research.

It is my pleasure to thank my parents Mr. Antony and Mrs. Regina Mary, brother Stalin and co-brothers, sister Amali and family for their great support and encouragement. My life is for them. I thank with kisses to my wife Ms. Deepika who sacrifices her life for my success.

Finally I would like to thank all those whom I have not mentioned above but helped me in numerous ways.



# CONTENTS

## Abstract

### CHAPTER I INTRODUCTION

1.1	Ruthenium oxide and copper oxide nanostructured materials	1
1.2	Principles of dielectric barrier discharge (DBD) plasma	2
1.3	DBD Plasmas for nanomaterial synthesis	5
1.4	Shape dependent performance of RuO <sub>2</sub> and CuO NMs in catalysis and biology	
	1.4.1 Photocatalytic activity	7
	1.4.2 CO oxidation catalysis using RuO <sub>x</sub> /γ-Al <sub>2</sub> O <sub>3</sub> and CuO/γ-Al <sub>2</sub> O <sub>3</sub>	8
	1.4.3 Antibacterial activity of RuO <sub>2</sub> and CuO NMs	9
1.5	Focus of current research	11
	References	12



2.1	Introduction	23
2.2	Materials used	23
2.3	DBD plasma reactor setup	23
2.4	Synthesis of RuO <sub>2</sub> nanomaterials under DBD plasma	24
2.5	Plasma Synthesis of RuO <sub>2</sub> using different substrates	25
2.6	Synthesis of RuO <sub>2</sub> by conventional methods	26
2.7	Shape dependent photocatalytic activity of RuO <sub>2</sub>	26
2.8	Shape dependent antibacterial activity of RuO <sub>2</sub>	27
	2.8.1 Thiobarbituric acid reactive species (TBARS) assay	28
2.9	Shape dependent CO oxidation using RuO <sub>x</sub> /γ-Al <sub>2</sub> O <sub>3</sub>	28

2.9.1	Syntheses of catalysts	28
2.9.2	Experimental part	29
2.10	Plasma synthesis of CuO nanomaterials	30
2.11	Synthesis of CuO by conventional methods	30
2.11.1	Antibacterial activity of CuO nanomaterials	31
2.11.2	Metal ion release analysis	33
2.12	Shape dependent CO oxidation performance using CuO / $\gamma$ -Al <sub>2</sub> O <sub>3</sub>	33
	References	34

### CHAPTER III RESULTS AND DISCUSSIONS

3.1	<b>Influence of plasma on the morphology of RuO<sub>2</sub></b>	35
3.1.1	Absorbance measurement by UV-visible spectrometer	36
3.1.2	X-ray diffraction study for structural analysis	36
3.1.3	X-ray photoelectron study for surface analysis	37
3.1.4	Surface morphological analysis	39
3.1.5	Morphological confirmation studies by FESEM	41
	3.1.5.1 Morphologies obtained in the absence of plasma	41
	3.1.5.2 Investigation on the effects of plasma treatments	42
3.1.6	Evolution of temperature during plasma reaction and its influence on the morphology	43
3.1.7	Possible chemical reaction mechanism mediated by plasma species	45
3.2	<b>Effect of substrates on the plasma synthesis of RuO<sub>2</sub></b>	48
3.2.1	Structure and composition analysis	48
3.2.2	Morphological studies	49

3.2.2.1	Preparation of RuO <sub>2</sub> NMs using different substrates under Ar plasma	49
3.2.2.2	Preparation of RuO <sub>2</sub> NMs using different substrates under Ar + O <sub>2</sub> plasma	51
3.2.3	Particle size analysis and zeta potential	53
3.2.4	Photocatalytic properties	56
3.3	<b>Alternative way of tailoring the morphology of RuO<sub>2</sub></b>	62
3.3.1	X-ray diffraction study for structural analysis	62
3.3.2	Surface morphological analysis.	63
3.3.2.1	Effect of concentration of NaOH and PEG on the morphological structure of RuO <sub>2</sub> nanomaterials	64
3.3.3	Analysis of functional groups using FT-IR spectroscopy	65
3.3.4	XPS surface chemical analysis	66
3.3.5	Stability of RuO <sub>2</sub> nanomaterials	68
3.3.6	Shape dependent anti-bacterial effects of RuO <sub>2</sub> nanomaterials	68
3.4	<b>Shape dependent CO oxidation performance of RuO<sub>x</sub>/γ-Al<sub>2</sub>O<sub>3</sub></b>	74
3.4.1	Characterization of the catalyst	74
3.4.2	CO oxidation performance of the catalysts	80
3.4.3	Discussions	83
3.5	<b>The DBD Plasma-mediated synthesis of CuO nanomaterials</b>	87
3.6	<b>Shape dependent antibacterial performance of CuO NMs</b>	90
3.6.1	X-ray diffraction study for structural analysis	90
3.6.2	Surface morphological analysis	91

3.6.3	Particle size analysis and surface charge measurement	95
3.6.4	Functional group and surface chemical analysis	96
3.6.5	Results of antibacterial activity	98
3.7	<b>Shape dependent CO oxidation performance of CuO nanomaterials</b>	105
3.8	Summary and Future directions	108
	References	110
<b>CHAPTER IV APPENDICES</b>		
4.1	List of abbreviations used	123
4.2	Calculations used	124
4.3	List of publications in international journals	127
4.4	Patent/s	128
4.5	Contribution to international conferences	129
4.6	Memories	130
4.7	About the author	131



## List of figures

Fig. 1.1	Examples of plasma routes for nanomaterial synthesis.	4
Fig. 1.2	The common dielectric barrier discharge configurations.	5
Fig. 1.3	The schematic representation of voltage vs. charge Lissajous figure representing the power consumption during plasma discharge.	5
Fig. 2.1	Schematic (a) and the laboratory setup (b) of the DBD plasma reactor used for NMs synthesis. (c) shows the photograph of the generated plasma.	24
Fig. 2.2	The experimental setup used for CO oxidation.	30
Fig. 3.1	(a) UV-visible absorbance spectra recorded during and after synthesis of RuO <sub>2</sub> NMs. (b) XRD spectra of RuO <sub>2</sub> NMs: (a) RO AG1 (Ar + H <sub>2</sub> ), (b) RO NP1 (Ar + O <sub>2</sub> ) and (c) RO NR1 (Ar).	36
Fig. 3.2	High resolution core level XPS spectra of Ru 3d and O 1s species for RO AG1 [(a) and (d)], RO NP1 [(b) and (e)] and RO NR1 [(c) and (f)], respectively.	38
Fig. 3.3	Effects of gas composition and concentration of NaOH on the surface morphology of RuO <sub>2</sub> NMs.	40
Fig. 3.4	FESEM surface morphologies of the RuO <sub>2</sub> NMs prepared under non-plasma condition in the presence of Ar + H <sub>2</sub> (a), Ar + O <sub>2</sub> (b) and Ar (c) feed gas.	41
Fig. 3.5	FESEM surface morphological images of wet chemically prepared RuO <sub>2</sub> powders after plasma exposure and when the reactions were started in its wet precipitation state.	43
Fig. 3.6	Temperature-time plots during RuO <sub>2</sub> synthesis.	44
Fig. 3.7	Substrate effects: Characterization results of RuO <sub>2</sub> NMs prepared in the	49

	presence of Ar + O <sub>2</sub> plasma.	
Fig. 3.8	Effect of substrate materials such as (a) copper, (b) silicon, (c) glass and (d) PET on the morphology of RuO <sub>2</sub> NMs in the presence of Ar plasma.	51
Fig. 3.9	Effect of substrate materials such as (a) copper, (b) silicon, (c) glass and (d) PET on the morphology of RuO <sub>2</sub> NMs in the presence of Ar + O <sub>2</sub> plasma.	52
Fig. 3.10	Particle size analysis histogram of RuO <sub>2</sub> NMs grown on various substrates in the absence and in the presence of oxygen.	55
Fig. 3.11	Band gap calculation by plotting $(\alpha hv)^2$ vs. $hv$ corresponding to spherical (a) and sheet-like (b) RuO <sub>2</sub> nanomaterials.	56
Fig. 3.12	The optical emission spectrum of the CFL used for the experiment.	57
Fig. 3.13	The UV-visible absorbance spectra corresponding to photolysis of methylene blue dye.	58
Fig. 3.14	The comparison of the % degradation of methylene blue versus exposure time using spherical (SP 2.5 and SP 5.0) and sheet-like (SH 2.5 and SH 5.0) RuO <sub>2</sub> NMs.	59
Fig. 3.15	The adsorption-desorption isotherm (a) and (c) and the multipoint BET plot (b) and (d) observed for spherical (SP 5.0) and sheet-like (SH 5.0) RuO <sub>2</sub> nanomaterials.	60
Fig. 3.16	X-ray diffraction patterns of SP NPs after heat treatment at different temperatures.	62
Fig. 3.17	FESEM and TEM surface morphology of wet chemically synthesized RuO <sub>2</sub> : SP NPs [(a) and (c)] and SH NPs [(b) and (d)], respectively.	63
Fig. 3.18	The effect of PEG and NaOH concentration on the sheet like morphology of	65

	RuO <sub>2</sub> NMs.	
Fig. 3.19	The FTIR spectra of SP NPS and SH NPs.	66
Fig. 3.20	XPS survey spectrum for RuO <sub>2</sub> (SH NPs).	67
Fig. 3.21	XPS high resolution core level spectra of SP NPs and SH NPs: Ru 3d <sub>3/2</sub> , Ru 3p <sub>3/2</sub> and O 1s.	67
Fig. 3.22	Zeta potential studies and particle size analysis carried out for spherical and sheet-like RuO <sub>2</sub> .	69
Fig. 3.23	The O.D. values measured using UV spectrophotometer representing the bacterial growth curves against different bacteria when interacting with SP NPs and SH NPs at different concentrations.	70
Fig. 3.24	The FESEM surface morphological images of <i>E. tarda</i> and <i>S. iniae</i> taken before and after interaction with SH NPs.	71
Fig. 3.25	Bar charts show the trends of MDA equivalents with increasing concentration of SP NPs, SH NPs and silver nanoparticles.	73
Fig. 3.26	The FESEM surface morphological images of RAWOS (a) and RAWS (b) catalysts. (Abbreviations: RAWOS: RuO <sub>x</sub> /γ-Al <sub>2</sub> O <sub>3</sub> without polymer stabilizer; RAWS: polymer stabilized RuO <sub>x</sub> /γ-Al <sub>2</sub> O <sub>3</sub> ).	74
Fig. 3.27	The TEM images of RAWOS (a) and RAWS (b) catalysts along with the EDX spectra. The composition of the catalyst elements are given inside.	75
Fig. 3.28	Formation mechanism of 1-D RuO <sub>x</sub> in the presence of PEG.	76
Fig. 3.29	The XRD spectra of the catalysts:	77
Fig. 3.30	The FTIR spectra recorded for ALVIR, RAWOS and RAWS catalysts (a-c).	77
Fig. 3.31	High resolution core level Al 2p, Ru 3d and Ru 3p spectra corresponding to	79

	RAWOS (a-c) and RAWS (d-f) catalysts.	
Fig. 3.32	The CO oxidation performance of RAWOS and RAWS catalysts with different concentrations of oxygen.	81
Fig. 3.33	Effect of (a) 2.5 vol. % and (b) 5 vol. % water content on the CO oxidation performance using RAWS and RAWOS catalyst.	82
Fig. 3.34	The CO conversion performance corresponding to (a) RAWOS, (b) RAWS and (c) activity difference between RAWOS and RAWS.	83
Fig. 3.35	The H <sub>2</sub> consumption (TPR) profiles of the RAWOS (a) and RAWS (b) catalysts.	86
Fig. 3.36	The FTIR (a) and XRD (b) spectra of the Ar plasma synthesized CuO nanomaterials.	87
Fig. 3.37	The FESEM images of the Ar plasma synthesized (a), wet chemically synthesized (c) and commercial (d) CuO samples. And (b) shows the particle size distribution of the plasma-mediated CuO NMs.	88
Fig. 3.38	Growth mechanism of CuO in the presence of Ar plasma.	89
Fig. 3.39	The XRD patterns of copper oxide nanomaterials.	91
Fig. 3.40	The FESEM images of the CuO 75, CuO 100 and HYD 150 samples prepared in the absence (a-c) and in the presence (d-f) of PEG surfactant, respectively.	93
Fig. 3.41	Effect of PEG addition on the morphology of CuO NMs.	94
Fig. 3.42	Particle size distribution observed for CuO 75, CuO 100 and HYD 150 (a-c). Typical zeta potential graph obtained for HYD 150 is given in (d).	95
Fig. 3.43	The FTIR spectra correspond to CuO 75, CuO 100 and HYD 150	97

nanomaterials.

Fig. 3.44	The XPS survey spectra of CuO 75, CuO 100 and HYD 150.	97
Fig. 3.45	The high-resolution core level Cu 2p <sub>3/2</sub> (a-c) and O 1s (d-f) XPS spectra of CuO 75, CuO 100 and HYD 150 samples.	98
Fig. 3.46	Photographs show the disc diffusion (zone of inhibition) results of CuO NMs against (a) <i>E. coli</i> and (b) <i>S. iniae</i> .	100
Fig. 3.47	The bar graph shows the value of the inhibition zone against different bacteria by using CuO 75, CuO 100 and HYD 150.	100
Fig. 3.48	Typical 96-well plate assay used to calculate the MIC values of <i>E. coli</i> for the prepared CuO NMs.	101
Fig. 3.49	Bar charts show the trends of MDA equivalents with increasing concentration of CuO NMs.	103
Fig. 3.50	The TEM image of the $\gamma$ -Al <sub>2</sub> O <sub>3</sub> support (a), CuO 75 (b) and CuO 100 (c).	105
Fig. 3.51	The XPS survey spectrum (a) and high resolution core level Cu 2p (b), Al 2p (c) and O 1s (d) spectra of CuO 75/ $\gamma$ -Al <sub>2</sub> O <sub>3</sub> .	106
Fig. 3.52	The CO oxidation performance of CuO 75/ $\gamma$ -Al <sub>2</sub> O <sub>3</sub> and CuO 100/ $\gamma$ -Al <sub>2</sub> O <sub>3</sub> .	107

## List of tables

Table 1	General properties of RuO <sub>2</sub> and CuO	3
Table 2	Composition of the feed gas and the concentrations of precursors	37
Table 3	XPS binding energies of identified species found with Ru.	39
Table 4	Conductivity values of the substrates explored at room temperature.	51
Table 5	Observed morphologies of the RuO <sub>2</sub> NMs obtained by changing the gas composition and the substrate.	54
Table 6	Properties of the nanomaterials measured using Barrett-Joyner-Halenda (BJH) method	60
Table 7	Physisorption results of the catalysts measured by using Barrett-Joyner-Halenda (BJH) method.	80
Table 8	The MIC values of the CuO NMs for the tested bacteria.	99
Table 9	Copper ions measurement in CuO NMs treated bacterial cultures using ICP-OES .	103

## ABSTRACT

One-dimensional nanostructured materials have attracted a great deal of interest owing to their potential applications in various industries. Due to the limitations and cost associated with conventional low-pressure plasma systems, atmospheric pressure plasma techniques such as dielectric barrier discharge (DBD) were investigated as an alternative approach for inducing specific chemical reactions. Ruthenium dioxide ( $\text{RuO}_2$ ) and copper oxide ( $\text{CuO}$ ) nanostructured materials are widely used in supercapacitor electrodes, field emission devices and for catalytic and biological applications. In such applications, size and shape dependent properties of nanomaterials play critical roles in improving the performance. In this research, an attempt was made to prepare one-dimensional  $\text{RuO}_2$  and  $\text{CuO}$  nanomaterials using DBD plasma. It was noted that the morphology of nanomaterials prepared by exposing the precursor to the DBD plasma was found to depend strongly on the characteristics of the substrate, physical properties of the synthesis materials as well as on the composition of the feed gas. The morphologies obtained from the plasma technique were also achieved by the conventional wet chemical methods using polyethylene glycol surfactant. The plasma techniques necessarily avoided the use of surfactant molecules, controlled the product morphology by few experimental variables, and showed the feasibility for scale up. In addition, oxidation state of the materials could be controlled by carefully selecting the plasma feed gas. The spherical and sheet shaped nanomaterials prepared using the above techniques was analyzed for their shape dependent performances in industrially and medically valuable applications such as photocatalysis, carbon monoxide ( $\text{CO}$ ) oxidation and antimicrobial activities. The photocatalytic behavior of spherical and sheet shaped  $\text{RuO}_2$  against methylene blue dye showed an excellent shape dependent catalytic activity in the presence of visible light. The  $\text{CO}$  oxidation using sheet-like  $\text{RuO}_x/\gamma\text{-Al}_2\text{O}_3$  showed the complete conversion

at 175 °C whereas it was achieved only at 200°C using spherical type  $\text{RuO}_x/\gamma\text{-Al}_2\text{O}_3$  and at every experimental temperature, sheet shaped nanomaterials showed increased CO conversion efficiency. Similar shape dependency was also noted when using grain-like and needle like  $\text{CuO}/\gamma\text{-Al}_2\text{O}_3$  at 300 °C. In the above catalytic cases, enhancement in the activity observed to sheet-like nanomaterials was the cumulative effects of increase in the porosity, morphology, catalyst stabilization and dispersion, and changes in the oxidation states. The  $\text{RuO}_2$  and  $\text{CuO}$  nanomaterials were assessed for the shape dependent anti-microbial activities against Gram positive and Gram negative bacteria. In all the cases, sheet like nanomaterials showed more inhibitive effect than spherical or other types. Interaction of nanomaterials with bacteria created an oxidative stress and released the corresponding metal ions and thus the microorganism lost its essential nutrients for survival.



# CHAPTER I

## INTRODUCTION

### 1.1 Ruthenium oxide and copper oxide nanostructured materials

Size and shape effects constitute a peculiar and fascinating aspect of nanostructured materials (for simplicity, nanomaterials or NMs). The effects determined by changing size and shape pertain to the evolution of structural, thermodynamic, electronic, spectroscopic, electromagnetic and chemical features of these finite systems. The properties of a material depend on the type of motion its electrons can execute, which depends on the space available for them. Thus, the properties of a material are characterized by a specific “length scale”, usually on the nm dimension. If the physical size of the material is reduced below this length scale, its properties change and become sensitive to size and shape.

Transition metal oxide NMs such as ruthenium oxide ( $\text{RuO}_x$  where  $x=2$ , predominantly) finds applications in preparing dimensionally stable anodes, thin film resistors and capacitors owing to its unique redox surface chemistry [1]. For instance,  $\text{RuO}_2$  nanorods are reported to increase the Seebeck coefficient in thermoelectric devices [2] and to exhibit enhanced field emission [3]. In addition  $\text{RuO}_x$  is a promising-material both in the context of catalysis [4,5] and energy [6]. For instance, combinations and composites based on metallic ruthenium/-ruthenium oxides are notable for coupling reaction catalysis [7], catalyzing the photochemical reduction of water [8], catalysts for  $\text{N}_2\text{O}$  decomposition [9], selective oxidation of alcohol [10] and oxidation of carbon monoxide (CO) [11-13]. The advantage of  $\text{RuO}_x$  for the above chemical and catalytic reactions is mainly from its low temperature activity but at the same time, its cost hinders its wide usage as an industrial catalyst. On account of the cost associated with it, the uniqueness and the performance of  $\text{RuO}_2$  could not be ruled out.

On the other hand, copper oxide nanomaterials (CuO NMs) [14] are also predominantly used in the above catalysis reactions [15,16], and for preparing sensors [17], high critical temperature superconductors [18] etc. due to its excellent physicochemical properties and cost effectiveness. It is the simplest member in the family of copper compounds and a narrow band gap (1.2 eV) p-type semiconductor which exhibits superior photocatalytic [19] and photovoltaic properties [20]. In addition, its biological and environmental usage such as preparation of antibacterial agent [21-24], in anti-tumor therapy [25], arsenic removal in water treatment [26] etc. are notable. Even though many reports suggest the usage of CuO NMs for a variety of applications, copper and its compounds find its indispensable application as a sterilization agent in water since ancient days. One disadvantage of using CuO for catalytic reactions is its high temperature operation. The RuO<sub>2</sub> and CuO NMs exhibit completely different physicochemical properties and investigation on these materials for selected applications may provide useful results. It is therefore, the reason for choosing the above materials could be well understood. The general properties of the RuO<sub>2</sub> and CuO NMs are listed in Table 1.

## **1.2 Principles of dielectric barrier discharge (DBD) plasma**

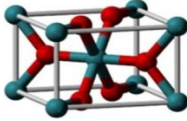
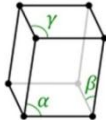
Plasmas are collection of freely moving charged particles which is, on the average, electrically neutral. Plasma discharges are driven by voltage or current sources. The collision between charged and neutral particles results in an ionization which is very important event to sustain the plasma. Different kinds of plasma techniques (Fig. 1.1) are used for variety of operations based on whether it belongs to thermal or non-thermal in nature and operate in vacuum or in atmospheric pressure. The mode of plasma generation, abundance and sustenance of plasma characterizes the design of the given plasma source. One of the plasma techniques which we deal with this research is dielectric-barrier discharges. These are characterized by the

application of one or more insulating layers in the current path between metal electrodes in addition to the discharge space. In such conditions the electrons are not in thermal equilibrium with ions and thus it is called as non-equilibrium (and non-thermal) plasma. The transported charge is proportional to the gap spacing and the permittivity of the dielectric but does not depend on pressure. Electrically induced plasmas are called ‘discharges’ and because of its low gas temperatures, are referred to as cold plasmas. In this case,

$$T_e \gg T_g \text{ and } T_e > T_i > T_g$$

Where, (T is the temperature, e-electrons, g- gas, and i-ions).

**Table 1. General properties of RuO<sub>2</sub> and CuO**

Molecular formula	RuO <sub>2</sub>	CuO
Molecular weight	133.06 g mol <sup>-1</sup>	79.545 g mol <sup>-1</sup>
Density	6.97 g cm <sup>-3</sup>	6.315 g cm <sup>-3</sup>
Appearance	Blue-black solid	Black to brown powder
Boiling point	1200 °C	2000 °C
Crystal structure	Rutile (tetragonal)	Monoclinic, mS8
		
Space group	P42 Imnm	C2/c
Band gap	2.2-2.7 eV	1.2 eV
Solubility in water	Insoluble	Insoluble
Precursor price	100\$/g	70\$/100g

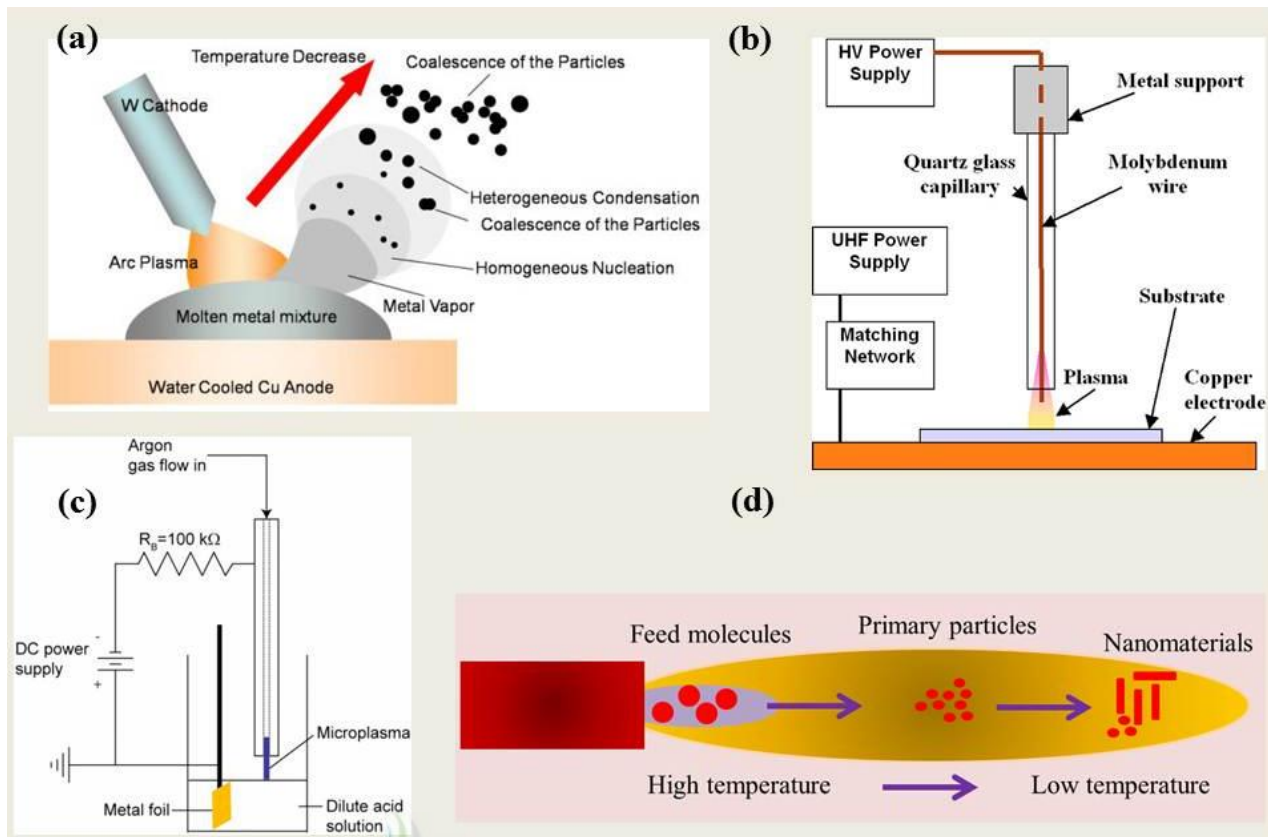


**Figure 1.1** Examples of plasma routes for nanomaterial synthesis. (a) DC arc method (b) self-organization of nanostructures produced by plasma (c) metal nanoparticle synthesis using micro-plasma (d) Gas phase particle formation process in thermal plasma [27-29].

Different types such as planar or cylindrical configurations are common (Fig. 1.2). Closely related are surface discharge configurations in which discharges are initiated at a dielectric surface due to strong electric fields generated by imbedded metal electrodes. The presence of the dielectric(s) precludes dc operation. Although DBD configurations can be operated between line frequency and microwave frequencies the typical operating range for most technical DBD applications lies between 500 Hz and 500 kHz [30]. From the Lissajous (charge-voltage plot) figure created during the plasma generation, the powder consumption can easily be calculated (Fig.1.3, and see the appendix).

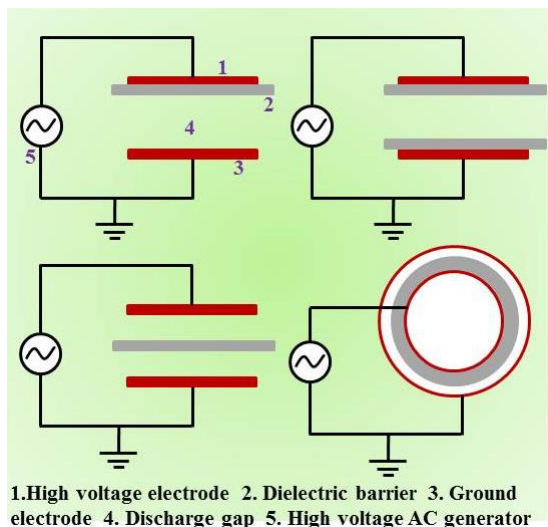


**Figure 1.2** The common dielectric barrier discharge configurations [30].

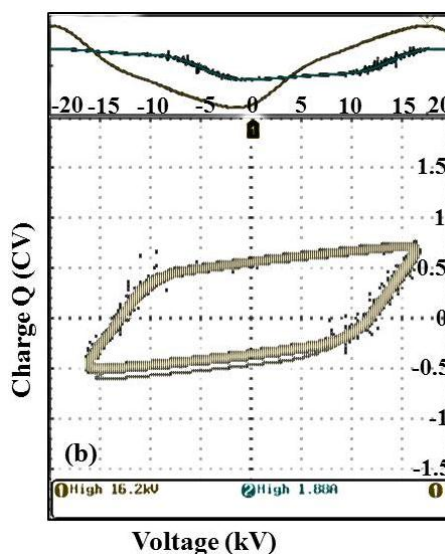


**Figure 1.3** The schematic representation of voltage vs. charge Lissajous figure, representing the power consumption during plasma discharge.

### 1.3 DBD Plasmas for nanomaterial synthesis

Nanostructured materials exhibit peculiar behaviors due to quantum effects (size) and interfacial phenomena. A solid object is called a nanostructured material when at least one of its dimensions lies within the range of nanometer to tens of nanometer. Particularly, one dimensional (1D) nanostructures (such as wires, belts, rods and tubes whose lateral dimensions fall anywhere in the range of 1-100 nm) are preferred in technologically valuable applications on account of the performance improvements resulting from their morphological effects. To accomplish 1D structure in wet chemical synthesis, care must be taken to optimize the process parameters such as precursor concentration, type and concentration of surfactant, pH and temperature. Plasma-mediated gas phase routes such as metal-organic chemical vapor deposition (MOCVD), microwave plasma synthesis [31,32] and sputtering techniques usually give high

aspect ratio 1D materials. Vapor deposition techniques are performed in high vacuum environments for which the installation cost and the energy requirements are very high. A review article by Ostrikov et al. [33] reports the plasma-based nanoscale materials synthesis achieved in vacuum environments with other fundamental considerations including classification and terminology. Thermal plasma is conventionally used through combustion-assisted plasma spraying but high operation cost related to cooling system and low energy efficiency hampers their use. In order to mitigate the above problems, atmospheric pressure non-equilibrium plasma [34,35] has been investigated as an alternative approach and interesting results have been achieved in synthesizing and functionalizing specific nanomaterials [36]. Recently, Mariotti et al. [29,37,38] have given a short review about the recent findings in the micro-plasma mediated NMs synthesis and they have also acknowledged the potential of other atmospheric plasma techniques such as dielectric barrier discharge (DBD). A quick review of the literature revealed that the DBD plasmas have mainly been used for gas purification, surface functionalization and synthesis of carbon-based nanomaterials [39-44]. In such DBD processes, there is no mandatory requirement for applying any external heating system and the whole reaction is carried out under non-thermal condition. Sometimes, a small increase of temperature caused by collisions of plasma constituents can be an advantage for reactions. The DBD plasma technique is a novel way of achieving 1D materials in which interactions between plasma constituents and precursor molecules serve as a key role. Due to easy handling and simplicity in design, there are many possibilities for the preparation of NMs, especially rod-shaped ones, by using the DBD plasma. Achievement of rod type NMs are fulfilled by the assistance of electric forces which require no capping agents, stabilizers and surfactants. The DBD plasma technique gains momentum nowadays for NMs synthesis [45], and it is imperative to note that information on the synthesis

of metal or metal oxide using the DBD plasma is scarce in the literature. With this background information, attempts have been made to prepare metal oxide nanomaterials such as RuO<sub>2</sub> and CuO using DBD plasma. The prepared NMs were used for specific applications stated below with an extensive literature survey. The NMs were also synthesized by conventional wet chemical techniques in order to demonstrate the uniqueness of plasma-mediated method.

## **1.4 Shape dependent performance of RuO<sub>2</sub> and CuO NMs in catalysis and biology**

### *1.4.1 Photocatalytic activity*

Semiconducting materials such as TiO<sub>2</sub> and ZnO exhibit the optical band gap for solar absorption of > 3 eV and thus they respond mainly in the UV region (except in some cases where they need to be functionalized with dyes for visible region response), which ultimately hampers their use as a visible light photocatalytic material. In order to use the visible region of the solar spectrum effectively (which occupies > 50% of the radiation), materials should be active in the said region with sufficiently lesser band gap. Nanomaterials such as RuO<sub>2</sub> and transition metal ions such as Cu<sup>2+</sup> and Fe<sup>3+</sup> have been reported to alter the band gap energy of the photo catalysts [46]. The RuO<sub>2</sub> NMs possess the band gap of about 2.2-2.7 eV and its compounds (especially with TiO<sub>2</sub>) have previously used for the photocatalytic oxidation of water in the presence of visible light [47], degradation of azo dyes under UV irradiation [48] etc. It was showed that the photocatalysis by organometallic ruthenium complexes is due to its favorable redox potentials, metal-to-ligand charge transfer etc [49]. But investigation on the possibility to use RuO<sub>2</sub> NMs as a visible light photo catalyst was not performed earlier. Thus, visible light photocatalytic performances of the spherical and one dimensional RuO<sub>2</sub> nanomaterials were carried out in this

research. At the same time, photocatalytic activity of CuO is basically UV responsive and numerous research was carried out earlier [50,51] and thus not reported here.

#### 1.4.2 CO oxidation catalysis using $RuO_x/\gamma-Al_2O_3$ and $CuO/\gamma-Al_2O_3$



Noble metal catalysts such as Pt and Pd exhibit good CO oxidation activity but concerns over cost and abundance have compelled researchers develop metal oxides as a viable alternative [52-55]. The catalytic activity of candidate metal oxide systems is heavily dependent on oxidation state and for example in the Ru-O system, when  $RuO_2$  catalyst is used under a high partial pressure of  $O_2$ , it exhibits a superior CO oxidation performance than Ru metal catalysts [10,56]. As stated earlier, CuO catalysts are viable alternative for preparing low cost industrial catalysts in abundance. Moreover, the performance of such catalysts can improve greatly when they are well stabilized or uniformly dispersed on the surface of the suitable support such as  $\gamma-Al_2O_3$  [57].



Dispersion is a critical step furthering an effective reaction between the reactants [58]. Conventional methods of catalyst dispersion on support materials by wet impregnation often yield aggregated structures [59]. Using DBD plasma to prepare  $RuO_x/\gamma-Al_2O_3$  or  $CuO/\gamma-Al_2O_3$  is also cumbersome because of the non-uniformity of the catalyst dispersion and plasma exposure only to upper surface of the catalyst. In this case, polymer molecules can be used in wet chemical nanomaterial synthesis as a stabilizer, surfactant or growth-directing agent [60,61] in which they control the particle aggregation, pore characteristics and in the catalysis context, stability and poisoning resistance of the support [62] relatively easier. Polyethylene glycol (PEG) is one of the most widely-used polymers in the design of heterogeneous catalysts [63] and can increase the interaction between the catalyst and the support. Polymer additives need to be

chosen carefully so as not to hinder the catalytic process and need to be removed by heat treatment prior to the experiment. PEG is an attractive choice as an additive since its oxidation products contain no nitrogen, sulfur or phosphorous thus precluding catalyst poisoning during heat treatment [64]. There are several reports describing the use of polymer stabilizers for the preparation of the catalysts [65-67] but there are few detailed studies on the surfactant-induced morphological changes and subsequent correlations with activity are available. Further understanding of such relationships provides a useful means to improve catalyst performance. In this study, the shape dependent CO oxidation performance of  $\text{RuO}_x/\gamma\text{-Al}_2\text{O}_3$  and  $\text{CuO}/\gamma\text{-Al}_2\text{O}_3$  catalysts were studied. Detailed physical and chemical characterizations of the materials have allowed us to begin to understand the connectivity between catalyst design and activity.

#### *1.4.3 Antibacterial activity of $\text{RuO}_2$ and $\text{CuO}$ NMs*

It is a well-known fact that microbial contamination of air, water, and soil due to different types of microorganism creates problems in living conditions and also it is a serious issue in health care. Apart from the major applications of  $\text{RuO}_2$  in energy and catalysis, investigation in the fields of biology, environmental conservation and health is very limited. Recently numerous studies indicate that nanoparticles have strong antibacterial activity against plant and animal pathogens. For example, metallic silver nanoparticles are known to inactivate microbes by interacting with their enzymes and restrain cell proliferation [68]. Recently many metal oxide NMs such as  $\text{Ag}_2\text{O}$ ,  $\text{ZnO}$ ,  $\text{Fe}_2\text{O}_3$ ,  $\text{TiO}_2$ ,  $\text{SnO}_2$ ,  $\text{CeO}_2$  and polymer membrane composites [69-74] were shown to exhibit good antibacterial activities. In addition to the type of materials, morphology also can induce additional effects on the microorganism. For example, size and shape dependent anti-bacterial activities are reported for single-walled carbon nanotubes [75] and silver [76]. Although great many studies on the antibacterial effect of numerous metal and

metal oxide nanoparticles are available, investigations using RuO<sub>2</sub> nanomaterials are very less in this field. Existing literatures have mainly focused on the activity of ruthenium complexes [77,78]. At the same time, recent reports on uptake and effect of nanoparticles with aquatic organisms such as fish species suggest its limited bioavailability [79,80]. Based on the above backgrounds, our curiosity to investigate the usage of RuO<sub>2</sub> nanomaterials for biological applications called for this research. When considering copper oxide for this application, the United States environmental protection agency (U.S EPA) has already approved only copper and its alloys as a solid surface material to continuously kill 99.9% bacteria within two hours on touch surfaces. When copper compounds used for cleaning of water, copper ions release from copper surface and hit the protein or fatty acid of the cell membrane, create holes (oxidative damage) through which the cell loses essential nutrients required for its survival [81,82]. Coating of CuO on the support membrane material is a good technique to kill microorganism and decontaminate polluted water by increasing the specific surface area and mesoporous property [83]. The main contribution of CuO over other metal oxide NMs is the cost benefit, which is cheaper than silver and exhibits relatively stable physical and chemical properties. It can easily mix with polymers and can be prepared with various surface morphologies and surface area [84].

In recent times, much attention is given to the synthesis of structure-specific (both size and shape) NMs since the material's effective performance largely depends on this factor [85-87]. For example, uptake and distribution of NMs by a biological system largely depend on the size, while preferential interaction with specific target molecules is mainly determined by the shape. Surface functionalization, surface area and morphology play important roles to inhibit the bacterial growth. The quantity of metal ion release, reactive oxygen species generation and interaction between microorganism and the NMs are mainly decided by the above factors [88-

91]. It must be noted in the literature that investigation on the shape-dependent behavior using CuO NMs is very less but can be found for Cu<sub>2</sub>O NMs [92,93]. Studies suggests that CuO NMs are superior to Cu<sub>2</sub>O based on the minimum bactericidal concentration (MBC) values. The main advantage of CuO over Cu<sub>2</sub>O is the stability. The CuO is stable at room temperature (Cu ion is in the +2 valance state) whereas Cu<sub>2</sub>O (+1 valance state) is stable above 1020°C only. Second, CuO primarily exhibit monoclinic crystal structure but Cu<sub>2</sub>O is cubic. This parameter is also important since the adsorption and desorption of bacteria greatly depend on the microstructure.

### **1.5 Focus of current research**

This research is focused on two themes such as preparation of structure specific nanomaterials and its application in catalysis and biology. The DBD plasma and wet chemical routes were used for the synthesis of RuO<sub>2</sub> and CuO NMs. The effects of plasma gas composition and growth substrates on the morphology of the NMs, plausible mechanisms elucidating the morphological differences, challenges in the plasma synthesis, and the physicochemical aspects of the prepared NMs are dealt with this section. On considering the application part, photocatalysis, CO oxidation catalysis and antibacterial activities with an emphasis on nanomaterial shapes are studied extensively.

## References

- [1] B. Zhang, C. Zhang, H. He, Y. Yu, L. Wang, J. Zhang, Electrochemical Synthesis of Catalytically Active Ru/RuO<sub>2</sub> Core–Shell Nanoparticles without Stabilizer, *Chem. Mater.* 22 (2010) 4056-4061.
- [2] D. Music, F.H.U. Basse, R. Habdorf, J.M. Schneider, Synthesis and thermoelectric properties of RuO<sub>2</sub> nanorods, *J. App. Phys.* 108 (2010) 013707-013711.
- [3] C.L. Cheng, Y.F. Chen, R.S. Chen, Y.S. Huang, Raman scattering and field-emission properties of RuO<sub>2</sub> nanorods 2005 *Appl. Phys. Lett.* 86 (2005) 103104-103107.
- [4] B-Z. Zhan, M.A. White, T-K. Sham, J.A. Pincock, R.J. Doucet, K.V.R. Rao, K.N. Robertson, T.S. Cameron, Zeolite-Confined Nano-RuO<sub>2</sub>: A Green, Selective, and Efficient Catalyst for Aerobic Alcohol Oxidation, *J. Am. Chem. Soc.* 125 (2003) 2195-2199.
- [5] W. Sugimoto, H. Iwata, Y. Yasunaga, Y. Murakami, Y. Takasu, Preparation of Ruthenic Acid Nanosheets and Utilization of Its Interlayer Surface for Electrochemical Energy Storage, *Angew. Chem. Int. Ed.* 42 (2003) 4092-4096.
- [6] Y. Zhang, C. Wang, N. Wan, Z. Mao, Deposited RuO<sub>2</sub>–IrO<sub>2</sub>/Pt electrocatalyst for the regenerative fuel cell, *Int. J. Hydrogen Energy* 32 (2007) 400-404.
- [7] S. Park, M. Kim, D.H. Koo, S. Chang, Use of Ruthenium/Alumina as a Convenient Catalyst for Copper-Free Sonogashira Coupling Reactions, *Adv. Syn. Catal.* 346 (2004) 1638-1640.
- [8] P.K. Dutta, A.S. Vaidyalingam, Zeolite-supported ruthenium oxide catalysts for photochemical reduction of water to hydrogen, *Microporous Mesoporous Mater.* 62 (2003) 107-120.

- [9] K. Li, X.F. Wang, H.C. Zeng, Kinetics of N<sub>2</sub>O Decomposition on a RuO<sub>2</sub>/Al<sub>2</sub>O<sub>3</sub> Catalyst, Chem. Engg. Res. Design 75 (1997) 807-812.
- [10] E.J. Gracia-Suarez, M. Tristany, A.B. Gracia, V. Colliere, K. Philippot, Carbon-supported Ru and Pd nanoparticles: Efficient and recyclable catalysts for the aerobic oxidation of benzyl alcohol in water, Microporous Mesoporous Mater. 153 (2012) 155-162.
- [11] L. Zang, H. Kisch, Room Temperature Oxidation of Carbon Monoxide Catalyzed by Hydrous Ruthenium Dioxide, Angew. Chem. Int. Ed. 39 (2000) 3921-3922.
- [12] D.W. Goodman, C.H.F. Peden, CO oxidation on ruthenium: The nature of the active catalytic surface, Surf. Sci. 601(2007) L124-L126.
- [13] H. Maeno, H. Matsumoto, US Patent 6429167 B1 (2002), to Idemitsu Kosan Company Limited.
- [14] Q. Zhang, K. Zhang, D. Xu, G. Yang, H. Huang, F. Nie, C. Liu, S. Yang, CuO nanostructures: Synthesis, characterization, growth mechanisms, fundamental properties, and applications, Prog. Mater. Sci. 60 (2014)208-337.
- [15] G. Avgouropoulos, J. Papavasiliou, T. Tabakova, V. Idakiev, T. Loannides, A comparative study of ceria-supported gold and copper oxide catalysts for preferential CO oxidation reaction, Chem. Eng. J. 124 (2006) 41-45.
- [16] R. Sankar, P. Manikandan, V. Malarvizhi, T. Fathima, K.S. Shivashangari, V. Ravikumar, Green synthesis of colloidal copper oxide nanoparticles using Carica papaya and its application in photocatalytic dye degradation, Spectrochimica Acta A 121 (2014) 746-750.

- [17] M. Yang, J. He, X. Hu, C. Yan, Z. Cheng, Y. Zhao, G. Zuo, Copper oxide nanoparticle sensors for hydrogen cyanide detection: Unprecedented selectivity and sensitivity, *Sensors Actuators B* 155 (2011) 692-698.
- [18] A. Sacuto, Y. Gallais, M. Cazayous, S. Blanc, M-A. Measson, J. Wen, Z. Xu, G. Gu, D. Colson, Electronic Raman scattering in copper oxide superconductors: Understanding the phase diagram, *C.R. Physique* 12 (2011) 480-501.
- [19] M. Umadevi, A.J. Christy, Synthesis, characterization and photocatalytic activity of CuO nanoflowers, *Spectrochimica Acta Part A*. 109 (2013) 133-137.
- [20] T. Oku, R. Motoyoshi, K. Fujimoto, T. Akiyama, B. Jeyadevan, J. Cuya, Structures and photovoltaic properties of copper oxides/fullerene solar cells, *J. Phys. Chem. Solids* 72 (2011) 1206-1211.
- [21] M.S. Hassan, T. Amna, O-B. Yang, M.H. El-Newehy, S.S. Al-Deyab, M-S. Khil, Smart copper oxide nanocrystals: Synthesis, characterization, electrochemical and potent antibacterial activity, *Colloids Surf. B* 97 (2012) 201-206.
- [22] T. Pandiyarajan, R. Udayabhaskar, S. Vignesh, R.A. James, B. Karthikeyan, Synthesis and concentration dependent antibacterial activities of CuO nanoflakes, *Mater. Sci. Engg. C* 33 (2013) 2020-2024.
- [23] I.M. El-Nahhal, S.M. Zourab, F.S. Kodeh, M. Selmane, I. Genois, F. Babonneau, Nanostructured copper oxide-cotton fibers: synthesis, characterization, and applications, *Inter. Nano Lett.* 2(2012)14-18.
- [24] M. Ahamed, H.A. Alhadlaq, M.A.M. Khan, P. Karuppiyah, N.A. Al-Dhabi, Synthesis, Characterization, and antimicrobial activity of copper oxide nanoparticles, *J. Nanomaterials* 2014 (2014) 1-4.

- [25] Y. Wang, F. Yang, H-X. Zhang, X-Y. Zi, X-H. Pan, F. Chen, W-D. Luo, J-X. Li, H-Y. Zhu, Y-P. Hu, Cuprous oxide nanoparticles inhibit the growth and metastasis of melanoma by targeting mitochondria, *Cell death disease* 4 (2013) r783.
- [26] A. Goswami, P.K. Raul, M.K. Purkait, Arsenic adsorption using copper (II) oxide nanoparticles, *Chem. Eng. Res. Design* 90 (2012) 1387-1396 .
- [27] T. Watanabe, M. Tanaka, Thermal plasma processing for functional nanoparticle synthesis, 16th ASEAN Regional Symposium on Chemical Engineering (2009) 47-50.
- [28] D. Mariotti, R.M. Sankaran, Microplasmas for nanomaterials synthesis, *J. Phys. D: Appl. Phys.* 43 (2010) 323001
- [29] P. Kong, A.Kawczak, Plasma synthesis of nanoparticles for nanocomposite energy applications, 8th World congress nanocomposites (2008).
- [30] U. Kogelschatz, B. Eliasson, W. Egli, Dielectric –Barrier Discharges. Principle and Applications, *J. Phys. IV France* 7 (1997) C4-47
- [31] M. Vennekamp et al, Formation of SiC nanoparticles in an atmospheric microwave plasma, *Beilstein J. Nanotech.* 2 (2011) 665-673.
- [32] K. Nadeem, H. Krenn, T. Traussnig, R. Wurschum, D.V. Szabo, I.L. Papst, Spin-glass freezing of maghemite nanoparticles prepared by microwave plasma synthesis, *J. App. Phys.* 111 (2012) 113911-113916.
- [33] K. Ostrikov, A.B. Murphy, Plasma-aided nanofabrication: where is the cutting edge?, *J. Phys. D:Appl. Phys.* 40 (2007) 2223
- [34] A. Chirokov, Gutsol, A. Fridman , Atmospheric pressure plasma of dielectric barrier discharges, *Pure Appl. Chem.* 77 (2005) 487-495.

- [35] F. Massines, C. Sarra-Bournet, F. Fanelli, N. Naude, N. Gherardi, Atmospheric Pressure Low Temperature Direct Plasma Technology: Status and Challenges for Thin Film Deposition, *Plasma process. Polym.* 9 (2012) 1041-1073.
- [36] T. Nozaki, K. Okazaki, Materials processing at atmospheric pressure: Nonequilibrium effects on nanotechnology and mega-industries, *Pure Appl.Chem.* 78 (2006) 1157-1172.
- [37] D. Mariotti, R.M. Sankaran, Perspectives on atmospheric-pressure plasmas for nanofabrication, *J. Phys. D:Appl. Phys.* 44 (2011) 174023-174030.
- [38] D. Mariotti, Nonequilibrium and effect of gas mixtures in an atmospheric microplasma, *App. Phys. Lett.* 92 (2008) 151505-151507.
- [39] Y.S. Mok, J.O. Jo, J.C. Whitehead, Degradation of an azo dye Orange II using a gas phase dielectric barrier discharge reactor submerged in water *Chem. Eng. J.* 142 (2008) 56-64.
- [40] Y.S. Mok, H.C. Kang, H.J. Lee, D.J. Koh, D.N. Shin, Effect of Nonthermal Plasma on the Methanation of Carbon Monoxide over Nickel Catalyst. *Plasma Chem. Plasma Proc.* 30 (2010) 437-447.
- [41] T. Nozaki, K. Okazaki., Carbon Nanotube Synthesis in Atmospheric Pressure Glow Discharge: A Review. *Plasma Process. Polym.* 5 (2008) 300-321.
- [42] Q. Zhou, Z. Zhao, Y. Chen, H. Hua, J. Qiu, Low temperature plasma-mediated synthesis of graphene nanosheets for supercapacitor electrodes. *J. Mat. Chem.* 22 (2012) 6061-6066.
- [43] W. Xu, X. Wang, Q. Zhou, B. Meng, J. Zhao, J. Qiu, Y. Gogotsi, Low-temperature plasma-assisted preparation of graphene supported palladium nanoparticles with high hydrodesulfurization activity. *J. Mater. Chem.* 22 (2012) 14363-14368.

- [44] P. Bruggeman, C. Leys, Non-thermal plasmas in and in contact with liquids, J. Phys. D:Appl. Phys.42 (2009) 053001.
- [45] Q.D. Sun, B.Yu, C.J. Liu, Characterization of ZnO Nanotube Fabricated by the Plasma Decomposition of Zn(OH)<sub>2</sub> Via Dielectric Barrier Discharge Plasma Chem. Plasma Proc. 32 201-209 (2012).
- [46] J. Zhao, C. Chen, W. Ma, Photocatalytic degradation of organic pollutants under visible light irradiation, Topics catal. 35 (2005) 269-278.
- [47] T. Ohno, F. Tanigawa, K. Fujihara, S. Izumi, M. Matsumura, Photocatalytic oxidation of water by visible light using ruthenium-doped titanium dioxide powder, J. Photochem. Photobiol. A 127 (1999) 107-110 .
- [48] A.O. Ibahadon, G.M. Greenway, Y. Yue, Photocatalytic activity of surface modified TiO<sub>2</sub>/RuO<sub>2</sub>/SiO<sub>2</sub> nanoparticles for azo-dye degradation, Catalysis Commn. 9 (2008) 153-157.
- [49] K. Zeitler, Photoredox catalysis with visible light, Angew. Chem. Int. Ed. 48 (2009) 2-7.
- [50] M. Umadevi, A.J. Christy, Synthesis, Characterization and photocatalytic activity of CuO nanoflower, Spectrochim. Acta. A 109 (2013) 133-137.
- [51] R. Sankar, P. Manikandan, V. Malarvizhi, T. Fathima, K.S. Shivashangari, V. Ravikumar, Green synthesis of colloidal copper oxide nanoparticles using *Carica papaya* and its application in photocatalytic dye degradation, Spectrochim. Acta. A 121 (2014) 746-750.
- [52] Y. Perez, M.L. Ruiz-Gonzalez, J.M. Gonzalez-Calbet, P. Concepcion, M. Boronat, A. Corma, Shape-dependent catalytic activity of palladium nanoparticles embedded in SiO<sub>2</sub> and TiO<sub>2</sub>, Catal. Today 180 (2012) 59-67.

- [53] Y. Martynova, B. Yang, X. Yu, J.A. Boscoboinik, S. Shaikhutdinov, H-J. Freund, Catal. Lett. Low Temperature CO Oxidation on Ruthenium Oxide Thin Films at Near-Atmospheric Pressures, 142 (2012) 657-663.
- [54] Sk. Mahammadunnisa, P.M.K. Reddy, N. Lingaiah, Ch. Subrahmanyam, Catal. Sci. Tech. NiO/Ce<sub>1-x</sub>Ni<sub>x</sub>O<sub>2-δ</sub> as an alternative to noble metal catalysts for CO oxidation 3 (2013) 730-736.
- [55] R. Wang, J. Wang, L. Liu, H. Dai, Shape-regulation: An effective way to control CO oxidation activity over noble metal catalysts, Catal. Today 201 (2013) 68-78.
- [56] Z-P. Liu, P. Hu, Mechanism for the high reactivity of CO oxidation on a ruthenium-oxide, The J. Chem. Phys. 114 (2001) 5956-5957.
- [57] M-C. Rosu, R-C. Suciu, S-V. Dreve, T-D. Silipas, I. Bratu, E. Indrea, The influence of PEG/PPG and of the annealing temperature on TiO<sub>2</sub>-based layers properties, Rev. Roum. Chim. 57 (2012) 15-21.
- [58] J.H. Sinfelt, Structure of metal catalysts, Rev. Modern Phys. 51(1979) 569-589.
- [59] I.E. Achouri, N. Abatzoglou, C.Fauteux-Lefebvre, N. Braidy, Diesel steam reforming: Comparison of two nickel aluminate catalysts prepared by wet-impregnation and co-precipitation, Catal. Today 207 (2013) 13-20.
- [60] B.A. Rozenberg, R. Tenne, Polymer-assisted fabrication of nanoparticles and nanocomposites, Prog. Polym. Sci. 33 (2008) 40-112.
- [61] H. Zhang, J. Feng, J. Wang, M. Zhang, Preparation of ZnO nanorods through wet chemical method, Mat. Lett. 61 (2007) 5202-5205.
- [62] M. Lijima, H. Kamiya, KONA Powder Particle J. 27 (2009) 119-129.

- [63] A. Ananth, Y.S. Mok, Preparation of ZnO nanorods through wet chemical method, Chem. Eng. J. 239 (2014) 290-298.
- [64] S. Han, C. Kim, D. Kwon, Thermal/oxidative degradation and stabilization of polyethylene glycol, Polymer 38 (1997) 317-323.
- [65] C. Kim, H. Lee, Shape effect of Pt nanocrystals on electrocatalytic hydrogenation, Catal. Commn. 11 (2009) 7-10.
- [66] H. Einaga, M. Harada, Photochemical Preparation of Poly(*N*-vinyl-2-pyrrolidone)-Stabilized Platinum Colloids and Their Deposition on Titanium Dioxide, Langmuir 21 (2005) 2578-2584 .
- [67] Y-S. Jung, W-L. Yoon, Y-W. Rhee, Y-S. Seo, Photochemical Preparation of Poly(*N*-vinyl-2-pyrrolidone)-Stabilized Platinum Colloids and Their Deposition on Titanium Dioxide, Int. J. Hydrogen Energy 37 (2012) 9340-9350.
- [68] K.H. Hong, Preparation and properties of electrospun poly(vinyl alcohol)/silver fiber web as wound dressings, Polym. Eng. Sci. 47 (2007) 43-49.
- [69] A. Azam, A.S. Ahmed, M.S. Khan, S.S. Habib, A. Memic, Antimicrobial activity of metal oxide nanoparticles against Gram-positive and Gram-negative bacteria: a comparative study, Int. J. Nanomed. 7 (2012) 6003-6009.
- [70] S.M. Dizaj, F.Lotfipour, M. Barzegar-Jalali, M.H. Zarrintan, K. Adibkia, Antimicrobial Activity of the Metals and Metal Oxides Nanoparticles, Mater. Sci. Eng. C 44 (2014) 278-284.
- [71] Y. Chen, Y. Zhang, J. Liu, H. Zhang, K. Wang, Preparation and antibacterial property of polyethersulfone ultrafiltration hybrid membrane containing halloysite nanotubes loaded with copper ions. Chem. Eng. J. 210 (2012) 298-308.

- [72] H. Yu, Y. Zhang, J. Zhang, H. Zhang, J. Liu, Preparation and antibacterial property of SiO<sub>2</sub>-Ag/PES hybrid ultrafiltration membranes. *Desalination Water Treatment* 51 (2013) 3584-3590.
- [73] Y. Chen, Y. Zhang, H. Zhang, J. Liu, C. Song, Biofouling control of halloysite nanotubes-decorated polyethersulfone ultrafiltration membrane modified with chitosan-silver nanoparticles. *Chem. Eng. J.* 228 (2013) 12-20.
- [74] J. Zhang, Y. Zhang, Y. Chen, L. Du, B. Zhang, H. Zhang, J. Liu, K. Wang, Preparation and Characterization of Novel Polyethersulfone Hybrid Ultrafiltration Membranes Bending with Modified Halloysite Nanotubes Loaded with Silver Nanoparticles. *Ind. Eng. Chem. Res.* 51 (2012) 3081-3090.
- [75] C. Yang, J. Mamouni, Y. Tang, L. Yang, Antimicrobial Activity of Single-Walled Carbon Nanotubes: Length Effect, *Langmuir* 26 (2010) 16013–16019.
- [76] S. Pal, Y.K. Tak, J.M. Song, Antibacterial Activity of Silver Nanoparticles Depend on the Shape of the Nanoparticle? A Study of the Gram-Negative Bacterium *Escherichia coli*, *App. Enviro. Microbiol.* 73 (2007) 1712-1720.
- [77] A. Bolhuis, L. Hand, J.E. Marshall, A.D. Richards, A. Rodger, J.A. Wright, Antimicrobial activity of ruthenium-based intercalators, *Euro. J. Pharma. Sci.* 42 (2011) 313-317.
- [78] T.D. Thangadurai, S. Jeong, S. Yun, S. Kim, C. Kim, Y.I. Lee, Antibacterial and luminescent properties of new donor–acceptor ruthenium triphenylphosphine–bipyridinium complexes, *Microchem. J.* 95 (2010) 235-239.

- [79] R. D. Handy, T. B. Henry, T. M. Scown, B. D. Johnston, C. R. Tyler, Manufactured nanoparticles: their uptake and effects on fish—a mechanistic analysis, *Ecotoxicology* 17(2008) 396–409.
- [80] T. M. Scown, R. M. Goodhead, B. D. Johnston, J. Moger, M. Baalousha, J. R. Lead, R. Aerle, T. Iguchi, C.R. Tyler, Assessment of cultured fish hepatocytes for studying cellular uptake and (eco)toxicity of nanoparticles, *Environ. Chem.* 7 (2010) 36–49.
- [81] A.K. Chatterjee, R. Chakraborty, T. Basu, Mechanism of antibacterial activity of copper nanoparticles, *Nanotechnology* 25 (2014) 135101-135112.
- [82] M.J. Hajipour, K.M. Fromm, A.A. Ashkarran, D. J. Aberasturi, I.R. Larramendi, T. Rojo, V. Serpooshann, W.J. Parak, M. Mahmoudi, Antibacterial properties of nanoparticles, *Trends. Biotechnol.* 30 (2012) 499-511.
- [83] Z. Liu, H. Bai, D.D. Sun, Hierarchical CuO/ZnO Membranes for Environmental Applications under the Irradiation of Visible Light, *Int. J. Photoenergy* 2012 (2012) 1-11.
- [84] G. Ren, D.Hu, E.W.C. Cheng, M.A. Vargas-Reus, P. Reip, R.P. Allaker, Characterisation of copper oxide nanoparticles for antimicrobial applications, *Int. J. Antimicrobial agents* 33 (2009) 587-590.
- [85] G. Guisbiers, S. Mejia-Rosales, F.L. Deepak, Nanomaterial properties: Size and Shape dependencies, *J. Nanomaterials*, 2012 (2012) <http://dx.doi.org/10.1155/2012/180976>.
- [86] A. Ananth, Y.S. Mok, Synthesis of RuO<sub>2</sub> nanomaterials under dielectric barrier discharge plasma at atmospheric pressure - Influence of substrates on the morphology and application, *Chem. Eng. J.* 239 (2014) 290–298.

- [87] A. Ananth, S. Dharaneedharan, M. S. Gandhi, M-S. Heo, Y. S. Mok, Novel RuO<sub>2</sub> nanosheets – Facile synthesis, characterization and application, Chem. Eng. J. 223 (2013) 729–736.
- [88] Y.H. Leung et al. Antibacterial activity of ZnO nanoparticles with a modified surface under ambient illumination, Nanotechnology 23 (2012) 475703-475714.
- [89] K. Zawadzka, K. Kadziola, A. Felczak, N. Wronska, I. Piwonski, A. Kisielewska, K. Lisowska, Surface area or diameter – which factor really determines the antibacterial activity of silver nanoparticles grown on TiO<sub>2</sub> coatings?, New J. Chem. 38 (2014) 3275-3281.
- [90] B. Vatsha, P. Tetyana, P.M. Shumbula, J.C. Ngila, L.M. Sikhwivhilu, R.M. Moutloali, Effects of precipitation temperature on nanoparticle surface area and antibacterial behavior of Mg(OH)<sub>2</sub> and MgO nanoparticles, J. Biomater. Nanobiotechnol. 4 (2013) 365-373.
- [91] S. Pal, Y.K. Tak, J.M. Song, Does the Antibacterial Activity of Silver Nanoparticles Depend on the Shape of the Nanoparticle? A Study of the Gram-Negative Bacterium Escherichia coli, Appl. Environ. Microb. 73 (2007) 1712-1720.
- [92] Y-J. Lee, S. Kim, S-H. Park, H. Park, Y-D. Huh, Morphology-dependent antibacterial activities of Cu<sub>2</sub>O, Mater. Lett. 65 (2011) 818-820.
- [93] H. Pang, F. Gao, Q. Liu, Morphology effect on antibacterial activity of cuprous oxide, Chem. Commun. (2009) 1076–1078.

## CHAPTER II

### EXPERIMENTAL METHODS

#### 2.1 Introduction

This chapter discusses the detail information about the experimental setup and methods used for the preparation of RuO<sub>2</sub> and CuO NMs using DBD plasma and wet chemical synthesis. Also experimental details related to photocatalysis, anti-bacterial properties, preparation of RuO<sub>x</sub>/γ-Al<sub>2</sub>O<sub>3</sub> and CuO/γ-Al<sub>2</sub>O<sub>3</sub> catalysts used for CO oxidation are given.

#### 2.2 Materials used

RuCl<sub>3</sub>.xH<sub>2</sub>O (MW. 207.43 g mol<sup>-1</sup>), polyethylene glycol (average MW. 20000) and Tetraethyl orthosilicate (TEOS, MW. 208.33 g mol<sup>-1</sup>) were purchased from Sigma-Aldrich. Copper (II) nitrate trihydrate (Cu(NO<sub>3</sub>)<sub>2</sub>.3H<sub>2</sub>O, MW. 241.6 g mol<sup>-1</sup>), ethyl alcohol and sodium hydroxide (NaOH) were purchased from Daejung chemical and metal Co. Ltd., Korea. The CuCl<sub>2</sub> (Hayashi Pure Chemical) and NH<sub>3</sub> (Junsei Chemical Co.) were also used. All chemicals are of analytical grade and used without further preparation.

#### 2.3 DBD plasma reactor setup

The preparation of RuO<sub>2</sub> and CuO NMs was carried out in a self-designed planar type DBD plasma reactor whose schematic diagram is presented in figure 2.1. Two stainless steel sheets (15 cm long and 4 cm wide) were acted as high voltage and ground electrodes. Two 1.5-mm-thick glass plates serving as a dielectric barrier were inserted between the electrodes. The distance between the upper and lower electrodes was fixed at 15 mm. The whole DBD reactor was enclosed in an acrylic chamber equipped with a gas inlet and outlet. Alternating current (AC) high voltage of about 16

to 20 kV at a frequency of 400 Hz was applied across the electrodes. The actual discharge power dissipated in the plasma reactor was calculated from the area of the so-called Lissajous curve (also known as charge-voltage plot) generated in a digital oscilloscope (*Tektronix MSO/DPO3000*). The feed gas to the DBD plasma reactor consisted of Ar and H<sub>2</sub> (or O<sub>2</sub>). Mass flow controllers (Atovac AFC 500) were used to adjust the flow rates of Ar, O<sub>2</sub> and H<sub>2</sub>.

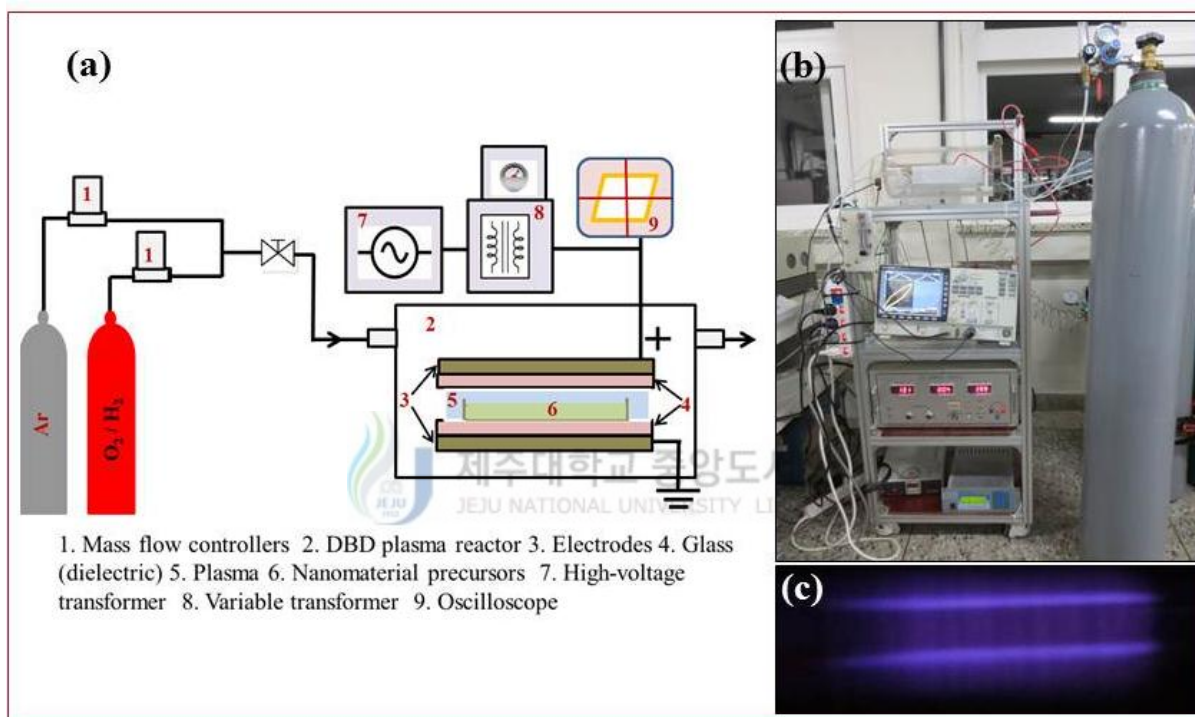


**Figure 2.1.** Schematic (a) and the laboratory setup (b) of the DBD plasma reactor used for NMs synthesis. (c) shows the photograph of the generated plasma.

## 2.4 Synthesis of RuO<sub>2</sub> nanomaterials under DBD plasma

Table 2 in the chapter III summarizes the feed gas composition and the concentrations of the precursors used. About 2 ml of RuCl<sub>3</sub>.xH<sub>2</sub>O and NaOH each were mixed in a small petri-dish (or on a glass plate) and kept inside the DBD plasma reactor. Two experimental parameters such as the NaOH concentration and the feed gas composition were chosen to control the growth and

agglomeration process. As an indication of the variation in the plasma density, the area of the Lissajous curve corresponding to the actual discharge power gradually increased from 2 to 32 W as time went by. At the end of 3-h plasma reaction, ruthenium hydroxide was formed as a black precipitate. The precipitate was washed repeatedly with deionized water in order to remove the un-reacted chemicals and byproducts. The powder was dried in a furnace at 350°C for 24 h and the final product was taken for further characterizations.

## **2.5 Plasma Synthesis of RuO<sub>2</sub> using different substrates**

So as to examine the substrate effect on the morphological structure of RuO<sub>2</sub> NMs, four different substrate materials such as copper (Cu), silicon (Si), glass (GL), and polyethylene terephthalate (PET) were used. The substrates were 5 cm long and 4 cm wide, respectively. (Table 5 in section III summarizes the sample names (based on the substrates used) and the flow rates maintained to grow NMs). About 500 μL of RuCl<sub>3</sub>.xH<sub>2</sub>O (0.1 M) and NaOH (1.0 M) each were mixed, stirred for 2 min and then it was spread on the substrate. The substrate was kept on the bottom electrode of the DBD plasma reactor. Gas purging with corresponding gases was done for 15 min and the samples were exposed to plasma. The input power was controlled at 38.20 W for all samples. It should be noted that the input power also includes the power consumed in the area not occupied by the nanomaterial precursor, i.e. actual power consumption for nanomaterial generation is much less than the aforementioned value. The area occupied by the nanoparticle precursor is about 1/5<sup>th</sup> of the whole electrode area. Two experimental parameters such as the composition of feed gas and the type of substrate were chosen to analyze the growth process. Black precipitate of Ru (OH)<sub>3</sub> was collected at the end of 3 h reaction, which was washed repeatedly with deionized water. Drying and heat treatment was performed at

350°C for 24 h by keeping the solid powder in a furnace, which eventually produced crystalline RuO<sub>2</sub> and they were used for photocatalysis experiments.

## **2.6 Synthesis of RuO<sub>2</sub> by conventional synthesis**

Two methods were carried out for preparing spherical and sheet-like RuO<sub>2</sub> nanomaterials. For spherical types (will be hereafter referred to as SP NPs), 0.1 M RuCl<sub>3</sub>.xH<sub>2</sub>O dissolved in 20 mL de-ionized water was taken in a two neck flat bottom flask stirred with magnetic stirrer and 20 mL of NaOH (1M) was added drop wise in a course of 3 h. For achieving sheet structures (will be hereafter referred to as SH NPs), about 0.4 g PEG (dissolved in 20 mL H<sub>2</sub>O) was added extra with the same concentrations of the reactants used in the first experiment [i.e. 0.1 M RuCl<sub>3</sub>.xH<sub>2</sub>O + 1 M NaOH + 0.4 g PEG]. The temperature of the solution was maintained at 75°C for the entire reaction. At the end of the reaction, black precipitate was formed. After discarding the supernatant, the precipitate was washed many times with deionized water. The solid precipitate was heat treated in a furnace up to 350°C for 24 h and the final product was taken for further characterization and anti-bacterial tests.

## **2.7 Shape dependent Photocatalytic activity of RuO<sub>2</sub>**

The photocatalytic activity of the spherical and one dimensional RuO<sub>2</sub> NMs was assessed by their degradation capability of methylene blue (MB) solution in the presence of a visible light. A compact fluorescent lamp (CFL, model: ES 220/N EX-L, Orex Co. Ltd, Korea) operating at 220V, 20 W and 60 Hz was used for this experiment. The light emission of the lamp was measured by using Maya 2000 PRO optical emission spectrometer. Exactly 4.5 mg of MB was dissolved in 1 L H<sub>2</sub>O and then RuO<sub>2</sub> NMs were added separately with 20 ml of the prepared solution. Known quantity of spherical and sheet shaped RuO<sub>2</sub> NMs was taken for experiments and named as SP 2.5 (2.5 mg spherical type), SP 5.0 (5 mg spherical type), SH 2.5 (2.5 mg sheet

type) and SH 5.0 (5 mg sheet type), respectively. The sample solution was kept in an open glass reactor, exposed to CFL lamp and simultaneously agitated by using a magnetic stirrer. A UV-visible absorbance spectrometer (model: HP 8453) was used to monitor the intensity of the dye solution at different time interval in order to monitor the degradation process.

## 2.8 Shape dependent antibacterial activity of RuO<sub>2</sub> nanomaterials

The bacterial species such as *S. iniae*, *S. parauberis*, *E. tarda* and *V. anguillarum* were maintained in Brain Heart Infusion (BHI) agar at 37 °C. The bacterial suspensions were prepared by taking a single colony from the stock bacterial culture with a loop and inoculating with 20 mL of sterile nutrient broth in a 100 mL Erlenmeyer flask. The flask was then incubated in a shaking incubator at 37 °C at 110 rpm for 24 ± 2 hours. After incubation, 0.4 mL of the overnight inoculum was transferred to a 100 mL Erlenmeyer flask containing 20 mL nutrient broth and incubated in a shaking incubator for 3 hours at 37 °C with 120 rpm. The RuO<sub>2</sub> nanomaterials (SP NPs and SH NPs) were diluted from two to four times with 100 μL of BHI broth and inoculated with each pathogenic bacteria at an approximate concentration between 10<sup>5</sup> to 10<sup>6</sup> colony-forming units (CFU)/mL. The bacterial concentration from 0 to 24 h was estimated by measuring the optical density of the culture at 660 nm using UV-visible spectrophotometer (Libra S22, Biochrom). Positive control with all the reaction components except nanomaterials, standard control containing all components with silver nanoparticles (10 mg/mL, instead of RuO<sub>2</sub> nanomaterials) and a negative control (without nanomaterials and bacterial cells) were also performed in triplicate and the mean ± standard error (SE) was taken.

### 2.8.1 Thiobarbituric acid reactive species (TBARS) assay

Free radicals generated in the cultures were estimated with TBARS assay kit (CellBiolabs, USA). Briefly, an aliquot of 1 mL of nanomaterials containing culture was collected to which 200  $\mu$ L of 10% SDS was added and swirled vigorously. About 2 mL of freshly prepared thiobarbituric acid (TBA) was added to the above mixture and incubated at 95  $^{\circ}$ C for 60 min. It was then cool down to room temperature and centrifuged at 3500 rpm for 15 min. The supernatant was collected and optical density was measured at 532 nm to estimate the formation of TBARS, a malondialdehyde (MDA) equivalent. All analyses were carried out in triplicate.

## 2.9. Shape dependent CO oxidation using $\text{RuO}_x/\gamma\text{-Al}_2\text{O}_3$

### 2.9.1. Syntheses of catalysts

1 wt.%  $\text{RuO}_x$  supported on mesoporous  $\gamma\text{-Al}_2\text{O}_3$  (referred hereafter as RAWOS) was prepared using the following homogeneous precipitation procedure (for calculations, refer appendix 4.2). Firstly, a known quantity of  $\text{RuCl}_3 \cdot x\text{H}_2\text{O}$  (0.155 g) and TEOS (0.25 wt.%, also containing ethanol and water) solution were prepared and mixed (previously it has been suggested that the *in situ* formation of a minor amount of  $\text{SiO}_2$  could improve the hardening of the oxidation catalyst without affecting its performance [1]). The solution was reacted with 25 mL, 1M  $\text{NH}_3$  solution (acting as a precipitating agent) at 75 $^{\circ}$ C. After 2 h, the required amount of  $\text{Al}_2\text{O}_3$  powder (9.9 g irreducible support) was added and the mixture was stirred for further 1 h. Following the reaction, the product was washed repeatedly with deionized water in order to remove the by-product and then heat-treated at 115  $^{\circ}$ C. The resulting powder was pressed into a pellet (approximately 8 Ton weight for 1 cm diameter) and calcined at 650  $^{\circ}$ C for 24 h. In order to investigate the role of stabilizer/surfactant, a separate sample (hereafter referred to as RAWOS)

was prepared as above with the addition of a synthesis step in which, PEG (0.5 g) was prior to the addition of the NH<sub>3</sub> solution. It is to be understood that the calcination step convert amorphous Ru (OH)<sub>3</sub> into RuO<sub>x</sub> and to remove PEG completely. Unmodified γ-Al<sub>2</sub>O<sub>3</sub> was also prepared as a reference sample (hereafter referred to as ALVIR). Following calcination, the pellets were crushed and sieved to obtain 2-3 mm size granules.

### 2.9.2 Experimental part

Exactly 10 g of catalyst prepared as above was loaded in a tubular reactor (1.5 cm diameter) and then fixed inside a furnace equipped with a temperature controller (Fig. 2.2). The volume of the catalyst inside the reactor was 11.48 cm<sup>3</sup>. The gas flow rate of CO was fixed at 2 cm<sup>3</sup>min<sup>-1</sup> (based on room temperature and at 1 atm) corresponding to 2000 ppm (the value of the space velocity is 5226 h<sup>-1</sup>). The oxygen concentration was varied from 0.5 to 2.5 vol.% and supplied to the reactor with N<sub>2</sub> carrier gas (total flow is 1 L min<sup>-1</sup>). All experiments were performed under isothermal conditions (the feed gases were introduced immediately after the required temperature was attained). The difference between the temperature measured at the catalyst using a thermocouple and recorded by the temperature controller was negligible. The concentration of CO at the outlet was measured by using the FTIR spectrometer after 1 h of the reaction. The percentage of conversion was calculated by using the following formula:

$$\text{CO conversion (\%)} = [1 - (\text{CO}_{\text{outlet}}/\text{CO}_{\text{inlet}})] \times 100 \quad \text{----- (2)}$$

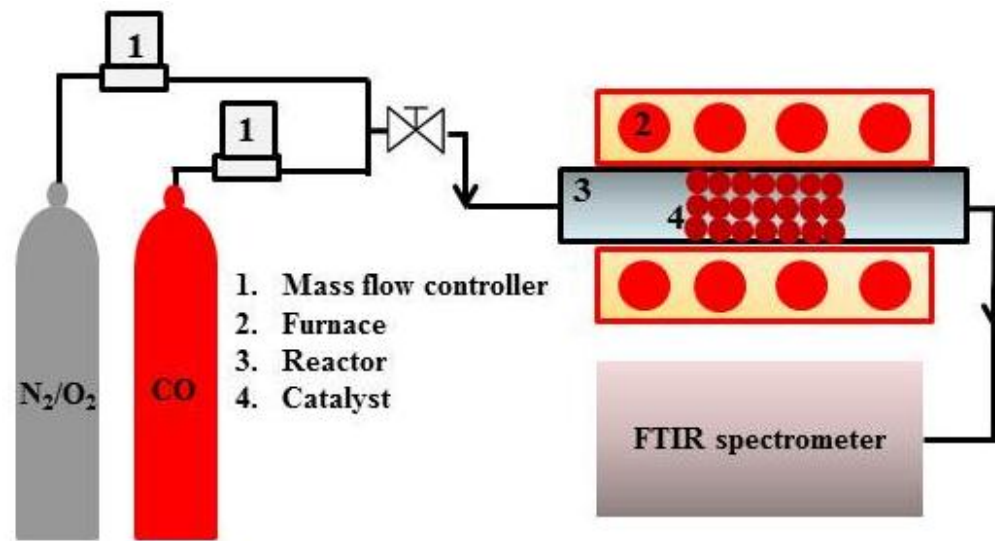


Fig. 2.2 The experimental setup used for CO oxidation.

## 2.10 Plasma Synthesis of CuO

The  $\text{CuCl}_2$  and  $\text{NH}_3$  were used as received. About 0.1 M of the above precursors was separately prepared and 500  $\mu\text{L}$  each was kept on a glass plate or in a petri dish. Then, 500  $\mu\text{L}$   $\text{NH}_3\text{OH}$  (1 M) precipitating agent was added, stirred using a glass rod and kept in between electrodes of the DBD reactor (Fig. 1.1). Then, Ar plasma was generated and the nanomaterial solution was exposed to the plasma for 3 hours. At the end of the plasma reaction, the product was collected, washed and annealed at 200°C.

## 2.11 Synthesis of CuO by conventional methods

Exactly 0.01M  $\text{Cu}(\text{NO}_3)_2 \cdot 3\text{H}_2\text{O}$ , 0.1M NaOH and 0.0002M PEG solutions were prepared separately in a 100 mL deionized water and agitated with a magnetic stirrer. The  $\text{Cu}(\text{NO}_3)_2 \cdot 3\text{H}_2\text{O}$  and PEG were mixed together and the temperature of the solution was maintained at 75°C. Then NaOH solution was added drop-wise by using a burette and observed the change in the color of the solution from light blue to black and the reaction was continued for another 3 h (will be referred hereafter as CuO 75). Second set of experiment was conducted with

all the precursors stated above but the temperature was kept at 100°C (will be referred hereafter as CuO 100) by using water condenser set up. Final set of experiment was performed with the same precursors in a hydrothermal reactor for 36 h and the furnace temperature was fixed at 150 °C (will be referred hereafter as HYD 150). At the end of the reaction, the precipitate was washed repeatedly with de-ionized water, dried and heat treated at 200 °C. All experiments were performed many times with different process parameters and the optimized variables (to obtain CuO with different surface morphology) are reported above. (It is to be understood that PEG is basically used for the stabilization of nanoparticles and it is eco-friendly [2] as well. The molecular weight (MW) of PEG has a strong influence on the viscosity of the solution. Increasing the MW would increase the viscosity and vice versa. It is reported in the literature that PEG with high MW (> 6000) decrease the dispersion of the metal salt. This is because high MW PEG behaves like a linear hydroxyl polymer, which is very hydrophilic in nature. It restricts the migration of the metal ions and thus reduces the size of the nanoparticles eventually [3]. In addition, size can also be controlled by using the same MW PEG with different concentration [4]. Crystallinity of the final product will not be affected much when using different MW PEG [5]. When considering the above points, it was planned to fix the size as minimum as possible by choosing the PEG 20000 and concentrated much on other experimental parameters to achieve different shapes).

### 2.11.1 Antibacterial activity of CuO nanomaterials

Antibacterial activity of the synthesized CuO NMs of different shapes were determined using a human Gram negative pathogenic bacteria, *Escherichia coli* and three major fish pathogens namely two Gram positive bacteria - *Streptococcus iniae*, *Streptococcus parauberis* and one Gram negative bacteria - *Vibrio anguillarum* following disc diffusion method. Bacteria were

cultured in Brain Heart Infusion (BHI) broth at 37 °C on a shaking incubator (at 190 rpm). A lawn of bacterial culture was prepared by spreading 100 µL culture broth ( $10^7$  CFU/mL) of each test organism on solid BHI agar plates. The CuO NMs (CuO 75, CuO 100 and HYD 150) were diluted to a stock concentration of 10 mg/mL of BHI broth and 10 µL of it was impregnated into the disk (diameter of 8 mm). Then the discs were allowed to dry for 15 min aseptically. The prepared CuO NMs impregnated discs were placed on each bacterial spread BHI agar plates and initially incubated for 15 min at 4 °C (to allow diffusion) and later on at 37 °C for 24 h. Positive test results were scored when a zone of inhibition was observed after the incubation period. Silver NMs was used as positive nanomaterial control (+NMC). The assay was performed in triplicates and the mean  $\pm$  standard error (SE) was calculated.

The minimum inhibitory concentration (MIC) was determined based on a broth micro-dilution method as described elsewhere [6]. Briefly, bacteria were cultured overnight at 37 °C in BHI broth and adjusted to a final density of  $10^7$  CFU/mL by 0.5 McFarland standards. Then, in a 96-well plate, 90 µL of BHI broth was added and 10 µL of CuO NMs (10 mg/mL) was diluted eight fold serially. To that 10 µL of bacterial culture was inoculated and then the 96-well plate was incubated at 37 °C for 12 h in shaking incubator rotating at 150 rpm. The lowest concentration at which no or least observable bacterial growth (as noted by the absence of visible bacterial growth) was taken as the MIC value of CuO NMs. Positive bacterial control (+BaC) with all the reaction components except nanomaterials, positive nanomaterial control (+NMC) containing all components with serially diluted silver nanomaterials (10 mg/mL, instead of CuO NMs), negative bacterial control (-BaC, containing CuO NMs without bacterial cells) and a negative control (without nanomaterials and bacterial cells, containing only BHI medium) were also performed simultaneously in triplicate and the mean  $\pm$  standard error (SE) was taken.

### 2.11.2. Metal ion release analysis

In order to estimate the release of copper ions, the CuO NMs treated bacterial cultures were centrifuged using 96-well plate centrifuge (PlateFuge™, Alkali Scientific Inc.). The obtained supernatant (contains dissolved Cu<sup>2+</sup>) and the pellet (contains bacterial culture, Cu<sup>2+</sup> and CuO NMs) were dissolved well in 2 vol.% nitric acid separately, kept overnight and subjected to elemental analysis using inductively coupled plasma-optical emission spectroscopy (ICP-OES 700 series, Agilent Technologies). Before that, standard ICP ionic solution with different concentrations (from 0.1 to 100 ppm) was prepared and the calibration curve was plotted.

### 2.12 Shape dependent CO oxidation performance using CuO / $\gamma$ -Al<sub>2</sub>O<sub>3</sub>

1 wt.% CuO (CuO 75 and CuO 100) supported on mesoporous  $\gamma$ -Al<sub>2</sub>O<sub>3</sub> was prepared by directly mixing the above powders. The resulting powder was pressed into a pellet (approximately 8 Ton weight for 1 cm diameter) and calcined at 650 °C for 24 h. Unmodified  $\gamma$ -Al<sub>2</sub>O<sub>3</sub> was also prepared as a reference sample. Following calcination, each of the pellets were crushed and sieved to obtain 2-3 mm size granules. The pellets were loaded inside a quartz tube and performed for CO oxidation experiments similar to the procedures carried out for RuO<sub>2</sub>.

## References

- [1] R.W. Baldwin, Upton, Mass., Preparation of catalyst pellets having sustained hardness and attrition resistance, US Patent 3146210 (1964), to OxyCatalyst. Inc.
- [2]. Y. Hatakeyama, T. Morita, S. Takahashi, K. Onishi, K. Nishikawa, Synthesis of Gold Nanoparticles in Liquid Polyethylene Glycol by Sputter Deposition and Temperature Effects on their Size and Shape, *J. Phys. Chem. C* 115 (2011) 3279-3285.
- [3] M. Sun, A. Zhu, Q. Zhang, Q. Liu, A facile strategy to synthesize mono disperse super paramagnetic OA-modified Fe<sub>3</sub>O<sub>4</sub> nanoparticles with PEG assistant, *J. Magn. Mater.* 369 (2014) 49-54.
- [4] S.A. Jayanthi, D.Sukanya, A.J.A. Pragasam, P.Sagayaraj, The influence of PEG 20,000 concentration on the size control and magnetic properties of functionalized bio-compatible magnetic nanoparticles, *Der Pharma Chemica* 5 (2013) 90-102.
- [5] N. Nabiyouni, A. Barati, M. Saadat, Surface Adsorption of Polyethylene Glycol and Polyvinyl Alcohol with Variable Molecular Weights on Zinc Oxide Nanoparticles, *Iranian J. Chem. Eng.* 8 (2011) 20-30.
- [6] F.A. Al-Bayati, Synergistic antibacterial activity between *Thymus vulgaris* and *Pimpinella anisum* essential oils and methanol extracts, *J. Ethnopharmacology* 116 (2008) 403-406.

## CHAPTER III

### RESULTS AND DISCUSSIONS

This chapter provides detailed information about the physico-chemical characterization, growth mechanisms of RuO<sub>2</sub> and CuO nanomaterials. Also, obtained results when the nanomaterials were utilized for the application such as photocatalysis, antibacterial activity and CO oxidation are dealt with in detail.

#### 3.1 Influence of plasma on the morphology of RuO<sub>2</sub>

##### 3.1.1 Absorbance measurement by UV-visible spectrometer

The mixture of RuCl<sub>3</sub>.xH<sub>2</sub>O and NaOH were exposed to plasma for 3 h (see Table 2). Generally the process of nanoparticle formation occurs in four stages such as precursor formation, nucleation, growth and ageing. Mixing of the reactants led to the formation of zero charge precursor molecules of hydrated hydroxide [1], i.e., insoluble Ru(OH)<sub>3</sub>. Such attainment of zero-charge molecules is necessary for further nucleation, which can be monitored by measuring the absorbance values. Figure 3.1 represents the UV-visible absorption spectra of the precursors recorded at different times when Ar plasma-assisted synthesis was performed (RO NR1). The RuCl<sub>3</sub> solution exhibited a broad absorbance peak at 407 cm<sup>-1</sup> due to the metal-ligand charge transfer. On mixing NaOH with RuCl<sub>3</sub>, the intensity of the peak started disappearing and at the end of 3-h plasma exposure, it completely vanished and might have shifted to higher energies. The analysis of the UV absorption spectra confirmed the complete chemical conversion of the precursor molecules into metal hydroxides [2]. Further, for the growth of metal oxide particles, olation and oxolation reactions occur, which means that hydrated hydroxides take part in condensation reactions. Theoretically, the super-saturation condition

resulting from increasing the precursor concentration leads to nucleation. The growth continues until the solution concentration falls to the saturation. Since the initial nucleation and growth of metal oxides might result in spherical shapes (due to the lowest possible surface energies) [3], a typical Mie scattering profile of exponential decay was observed, which is in agreement with the previous results [4]. The growth and the ageing process are determining factors for the final morphology of the RuO<sub>2</sub> NMs, which also depend on the experimental conditions.

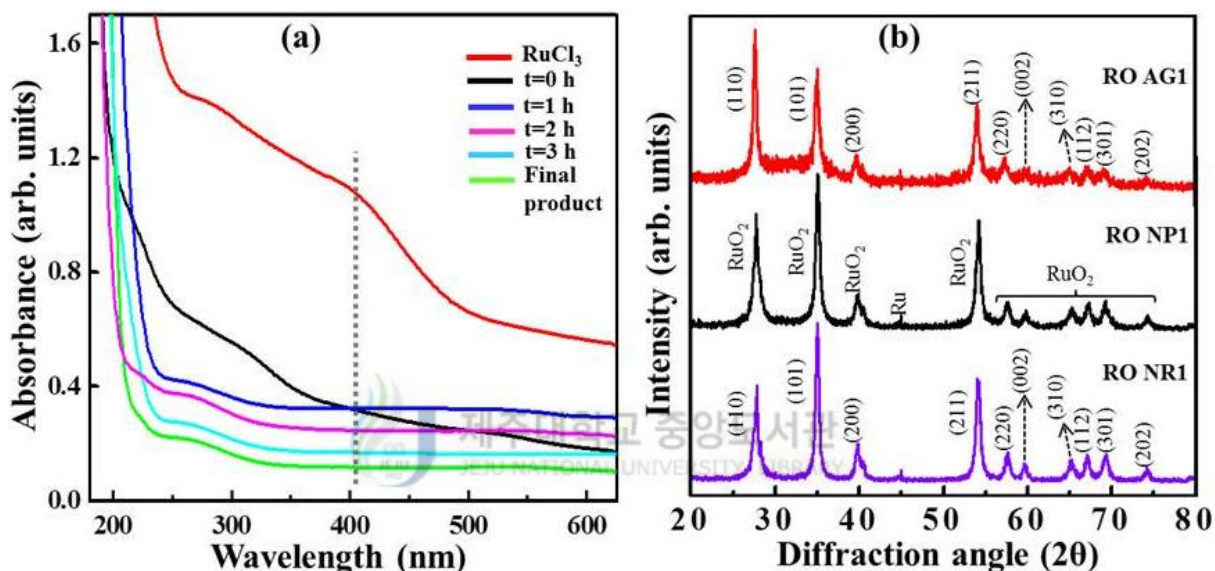


**Figure 3.1** (a) UV-visible absorbance spectra recorded during and after synthesis of RuO<sub>2</sub> NMs. (b) XRD spectra of RuO<sub>2</sub> NMs: (a) RO AG1 (Ar + H<sub>2</sub>), (b) RO NP1 (Ar + O<sub>2</sub>) and (c) RO NR1 (Ar).

### 3.1.2 X-ray Diffraction study for structural analysis

Ruthenium hydroxides obtained from plasma exposure were amorphous in nature, and thus the powders were heat-treated in a furnace to obtain crystallinity by removing water molecules [5]. Figure 3.1 (b) displays the XRD patterns of RuO<sub>2</sub> NMs heat-treated at 350°C corresponding to RO AG1, RO NP1 and RO NR1, respectively. Regardless of the feed gas compositions, RuO<sub>2</sub> NMs yielded a good crystallinity with prominent diffraction peaks. Due to

thermal decomposition of RuO<sub>2</sub> in the furnace, a small amount of metallic Ru was observed [6]. In fig. 3.1 (b), major Bragg reflections at 2θ values around 28.00°, 34.93°, 39.64° and 54.00° represent (110), (101), (200) and (211) set of lattice planes of rutile RuO<sub>2</sub> (JCPDS card no.88-0322).

**Table 2.** Composition of the feed gas and the concentrations of precursors

Sample name	Feed gas flow rate (cm <sup>3</sup> min <sup>-1</sup> )	Conc. of RuCl <sub>3</sub> .xH <sub>2</sub> O (M)	Conc. of NaOH (M)
RO AG1	Ar (60)+H <sub>2</sub> (15)	0.1	1
RO AG2		0.1	2
RO NP1	Ar (60)+O <sub>2</sub> (15)	0.1	1
RO NP2		0.1	2
RO NR1	Ar (75)	0.1	1
RO NR2		0.1	2

RO→ ruthenium oxide; AG→ aggregated; NP→ nano pillar; NR→ nano rod; gas flow rates are mentioned in the parentheses.

### 3.1.3 XPS- surface chemical analysis

The chemical nature of the surface of RuO<sub>2</sub> NMs prepared by using Ar + H<sub>2</sub>, Ar + O<sub>2</sub> or Ar feed gas was studied with the help of XPS. The high resolution core level spectra for Ru 3d (3d<sub>5/2</sub> and 3d<sub>3/2</sub>) and O 1s were taken in the range between 278-292 and 527-535 eV, respectively, for samples RO AG1, RO NP1 and RO NR1(Fig. 3.2). The spectra were de-convoluted using a peak fit program (Gauss-Lorentzian) by fixing the full width at half maximum (FWHM) values at 1.4 and 1.8 for Ru 3d and O 1s spectra, respectively. The positions corresponding to the binding energies of the species and their assignments are listed in table 3. One can note from

table 3 that the chemical state of Ru prepared using Ar plasma (RO NR1) showed a major portion containing RuO<sub>2</sub> (Fig. 3.2 (c)). The Ar + H<sub>2</sub> (RO AG1) and Ar + O<sub>2</sub> (RO NP1) plasma-synthesized samples exhibited a considerable portion of RuO<sub>3</sub> in addition to RuO<sub>2</sub> [Fig. 3.2 (a) and (b)]. It represents the presence of non-stoichiometric oxygen on the surface of Ru. The respective O 1s spectra [Fig. 3.2 (d)-(f)] for RO AG1, RO NP1 and RO NR1 showed main peaks at 531.7 eV along with lower binding energy lattice oxygen around 529.3 eV, which indicated the enhancement in the interaction between Ru and O species forming RuO<sub>2</sub> [7].

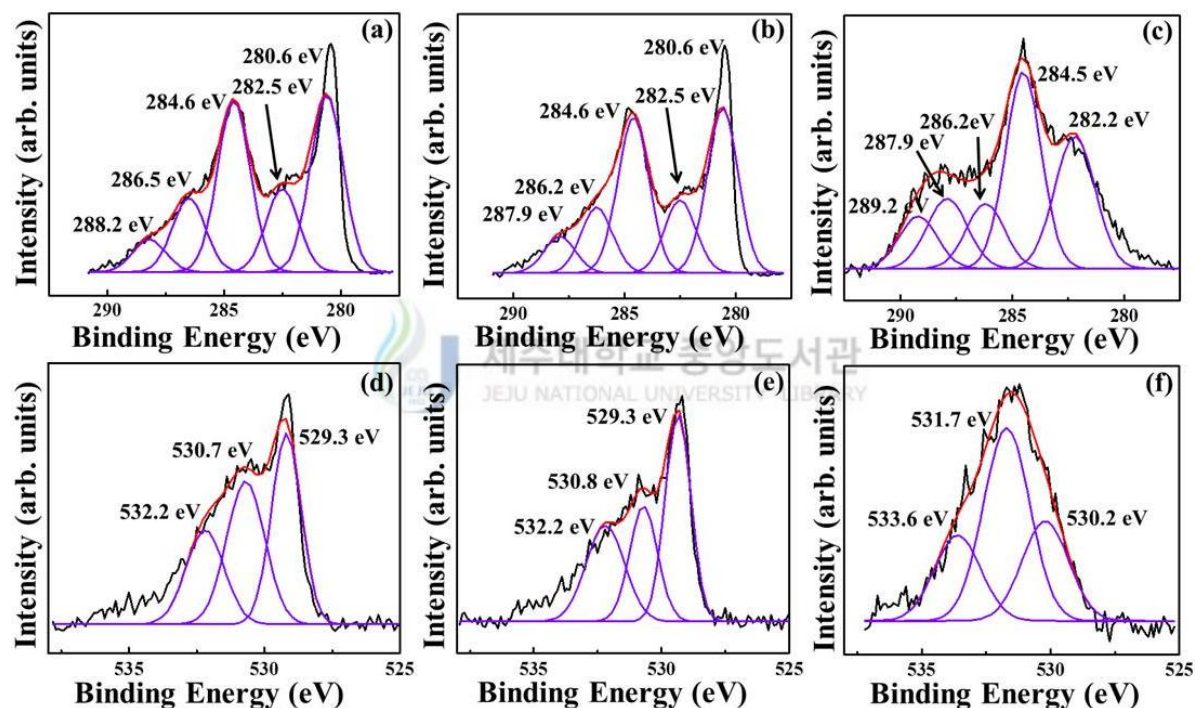


**Figure 3.2** High resolution core level XPS spectra of Ru 3d and O 1s species for RO AG1 [(a) and (d)], RO NP1 [(b) and (e)] and RO NR1 [(c) and (f)], respectively.

**Table 3.** XPS binding energies of identified species found with Ru.

Sample name	Species	Peak position (eV)	Assignment	Refs.
RO AG1 and RO NP1	Ru 3d	280.6	RuO <sub>2</sub>	[8]
		282.5	RuO <sub>3</sub>	[9]
		284.6	C 1s	
		286.2	CO	[10]
		286.5	CO <sub>2</sub>	[11]
		287.9	CO	[12]
		O 1s	529.3	RuO <sub>2</sub>
	530.7		RuO <sub>3</sub>	[9]
	530.8		Non stoichiometric O <sub>2</sub>	[14]
	RO NR1	Ru 3d	532.2	Molecular O <sub>2</sub>
282.2			RuO <sub>2</sub>	[16]
284.5			C 1s	
286.2			CO	[10]
O 1s		287.9	CO	[12]
		530.2	Atomic Oxygen	[17]
		531.7	RuO <sub>x</sub> /Ru	[18]
		533.6	Chemisorbed O <sub>2</sub>	[14]

### 3.1.4 Surface morphological analysis

Figure 3.3 shows the FESEM images of the RuO<sub>2</sub> NMs prepared using three different combinations of plasma gases (see Table 2). Figures 3.3 (a) and (b) show the surface morphological images when using Ar + H<sub>2</sub>. As can be seen from these figures, RuO<sub>2</sub> NMs prepared using this method were completely aggregated in nature and displayed a non-specific structure (RO AG1). In addition, increasing the concentration of NaOH twice (RO AG2) did not help attain a particular morphology. Figures 3.3 (c) and (d) show the structures of RuO<sub>2</sub>

resulting from Ar + O<sub>2</sub> plasma exposure. When 1 M NaOH was used, a ‘pillar-like’ morphology (RO NP1) with ‘channel-like’ cut portions was observed [figure 3.3 (c)].

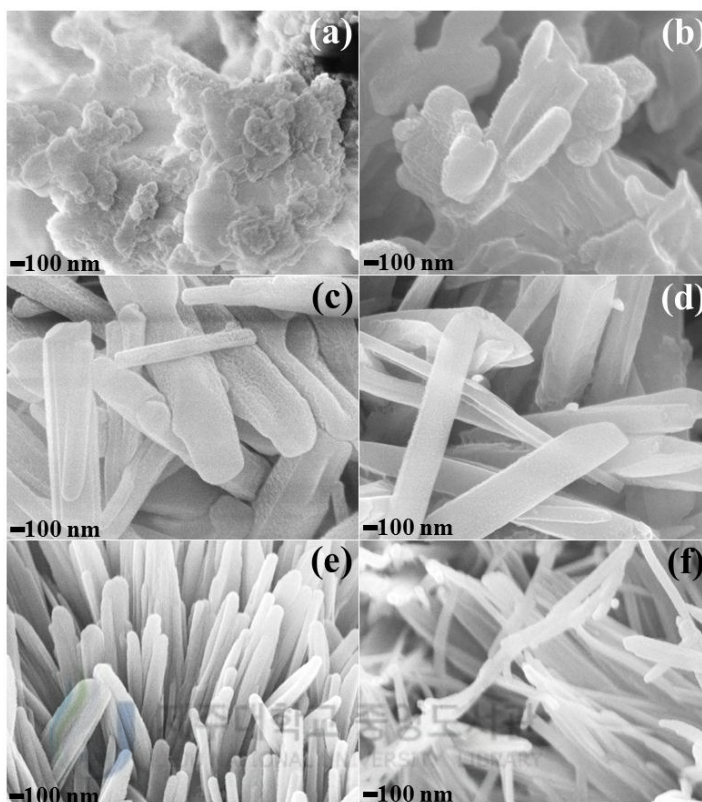


**Figure 3.3.** Effects of gas composition and concentration of NaOH on the surface morphology of RuO<sub>2</sub> NMs. FESEM images obtained when (a) Ar + H<sub>2</sub> gas mixture and 1 M NaOH [RO AG1]; (b) Ar + H<sub>2</sub> gas mixture and 2 M NaOH [RO AG2]; (c) Ar + O<sub>2</sub> gas mixture and 1 M NaOH [RO NP1]; (d) Ar + O<sub>2</sub> gas mixture and 2 M NaOH [RO NP2]; (e) Ar gas and 1 M NaOH [RO NR1]; (f) Ar gas and 2 M NaOH [RO NR2] were used.

When the concentration of NaOH was increased to 2 M, they exhibited a perfect ‘nanopillar’ morphology (RO NP2) showing widths and lengths in the range of 200 nm and >1.5 μm, respectively [figure 3.3 (d)]. On the other hand, when Ar only was used as the feed gas, regular and uniformly-oriented RuO<sub>2</sub> ‘nanorods’ were obtained. When 1 M NaOH was used, the nanorods prepared were approximately 100 nm width [figure 3.3 (e)]. Increasing the NaOH

concentration resulted in further changes in the width and the length to less than 100 nm and to greater than 2.5  $\mu\text{m}$ , respectively [figure 3.3 (f)]. The FESEM results demonstrated that the growth and the morphology of  $\text{RuO}_2$  were mainly controlled by the gas composition, while the concentration of  $\text{NaOH}$  played an auxiliary role.

### 3.1.5 Morphological confirmation studies

#### 3.1.5.1 Morphologies obtained in the absence of plasma

In order to confirm whether the morphology of  $\text{RuO}_2$  NMs results from plasma effects, additional reference experiments were performed using the respective gas compositions. For these experiments, instead of applying high voltage, the precursor solution was heated according to the recorded temperature curves in section 3.6. Figures 3.4 (a)-(c) show the FESEM surface morphologies of the  $\text{RuO}_2$  NMs prepared in the presence of  $\text{Ar} + \text{H}_2$ ,  $\text{Ar} + \text{O}_2$  and  $\text{Ar}$  gas atmosphere, respectively. The NMs prepared in the presence of mixed gases exhibited random aggregation with no specific morphology, as compared to less aggregated spherical particles observed in the  $\text{Ar}$ -only case. Since all the above cases did not result in any specific morphologies it can be concluded that the nanopillar and nanorod structures observed in section 3.1.4 are entirely attributed to plasma mediation.

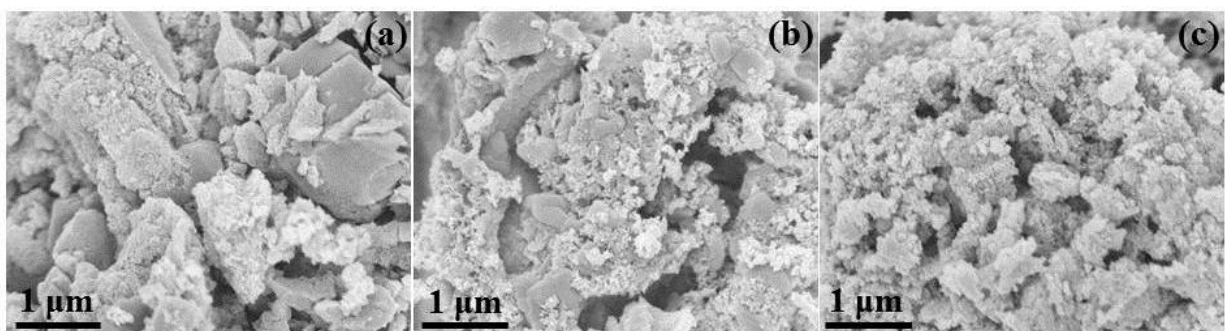


**Figure 3.4.** FESEM surface morphologies of the  $\text{RuO}_2$  NMs prepared under non-plasma condition in the presence of  $\text{Ar} + \text{H}_2$  (a),  $\text{Ar} + \text{O}_2$  (b) and  $\text{Ar}$  (c) feed gas.

### 3.1.5.2 Investigations on the effects of plasma treatments

We also investigated whether the morphology could be altered by exposing RuO<sub>2</sub> powders obtained from the wet chemical method to plasma. One set of experiment includes the preparation of RuO<sub>2</sub> nanoparticles by the wet chemical method, followed by exposing the dry powder to Ar + H<sub>2</sub>, Ar + O<sub>2</sub> and Ar plasma for 3 h. The FESEM surface morphologies are given in figures 3.5 (a)-(c), respectively. The spherical morphology obtained from the chemical method was not affected much by the plasma exposure but their aggregation behaviors slightly differed from each other, depending on the gas composition. Ar + H<sub>2</sub> and Ar + O<sub>2</sub> plasma resulted in an agglomeration of the RuO<sub>2</sub> nanoparticles with varying degrees whereas Ar plasma did not encourage the above behavior [Fig. 3.5 (c)]. Another set of experiment includes exposing the wet chemically prepared RuO<sub>2</sub> in its precipitate state containing some water to Ar + H<sub>2</sub>, Ar + O<sub>2</sub> and Ar plasma. The FESEM morphological images are given in Figs. 3.5 (d)-(f), respectively. According to the gas composition, changes in the aggregation behaviors were also noticed here. When Ar + H<sub>2</sub> was used, the RuO<sub>2</sub> particles were conglomerated [Fig. 3.5 (d)]. Similar trend was noticed for Ar + O<sub>2</sub> with a minor distinction [figure 3.5 (e)]. When Ar plasma was used, the nucleated RuO<sub>2</sub> particles tried to align themselves in a perfect straight line (arrow marked) and eventually rendered a self-assembled bundles [figure 3.5 (f)]. An important point to be noted is that the transformation from spherical to rod structure was not achieved in all these cases. The above experiments gave an important confirmation that the morphology of RuO<sub>2</sub> powders prepared using wet chemical routes could not be altered by the post plasma treatments, irrespective of whether they are in dry or wet states. Conversely speaking, the whole reaction should be carried out in the presence of Ar plasma for attaining uniform 1D surface architecture.

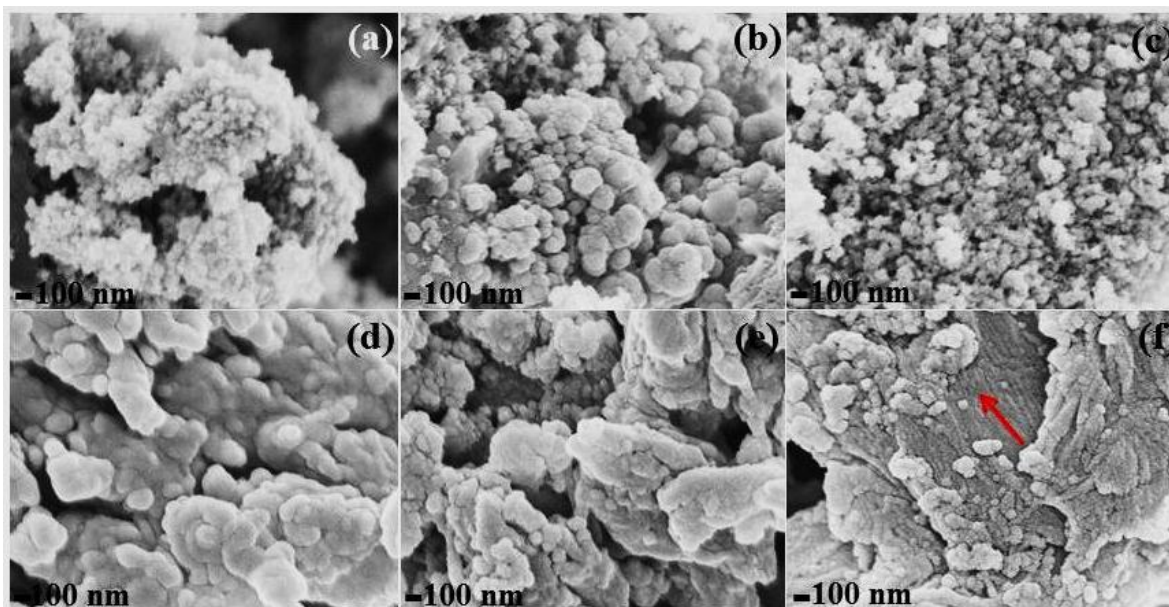


**Figure 3.5.** FESEM surface morphological images of wet chemically prepared  $\text{RuO}_2$  powders after (a)  $\text{Ar} + \text{H}_2$ , (b)  $\text{Ar} + \text{O}_2$  and (c)  $\text{Ar}$  plasma exposure. The surface morphological images of the  $\text{RuO}_2$  NMs after exposed to (d)  $\text{Ar} + \text{H}_2$ , (e)  $\text{Ar} + \text{O}_2$  and (f)  $\text{Ar}$  plasma when the reactions were started in its wet precipitation state.

### 3.1.6 Evolution of temperature during plasma reaction and its influence on the morphology

It was inferred from the literature that temperature plays an important role in rendering specific morphology in NMs. We investigated the effect of the feed gas composition on the morphology of  $\text{RuO}_2$  by monitoring the variations in the temperature versus time inside the plasma reactor. Totally two alcohol thermometers one of which was fixed at the center of the reactor ( $T_1$ ) and the other one was placed on the top of the nanomaterial precursors ( $T_2$ ) in order to probe the changes in the solution and the surrounding temperature during the synthesis. Figures 3.6 (a)-(c) show the temperature-time plot (heating curves) when  $\text{Ar} + \text{H}_2$ ,  $\text{Ar} + \text{O}_2$  and  $\text{Ar}$  were used, respectively. It was observed that the attainment of thermal equilibrium depended on the composition of the gas mixture and time. The initial values of  $T_1$  and  $T_2$  were 30 and 28°C, respectively. From the beginning to the end, gradual increases in  $T_1$  and  $T_2$  were observed

for all the cases. The increase in the temperature increases the vapor pressure of the solution, leading to the evaporation of water molecules. In addition, the energy imparted from the plasma constituents to the solution was utilized for interfacial electrochemical reactions [19]. The observed difference ( $\Delta T$ ) between  $T_1$  and  $T_2$  was approximately between 2 and 8°C from start-up until about 120 min of the process. After that, both  $T_1$  and  $T_2$  reached almost the same temperature beyond 150 min for mixed gases (Ar + H<sub>2</sub> and Ar + O<sub>2</sub>) and 130 min for Ar, respectively. It means that the entire chemical reactions were carried out in a gradually varying thermodynamic condition.

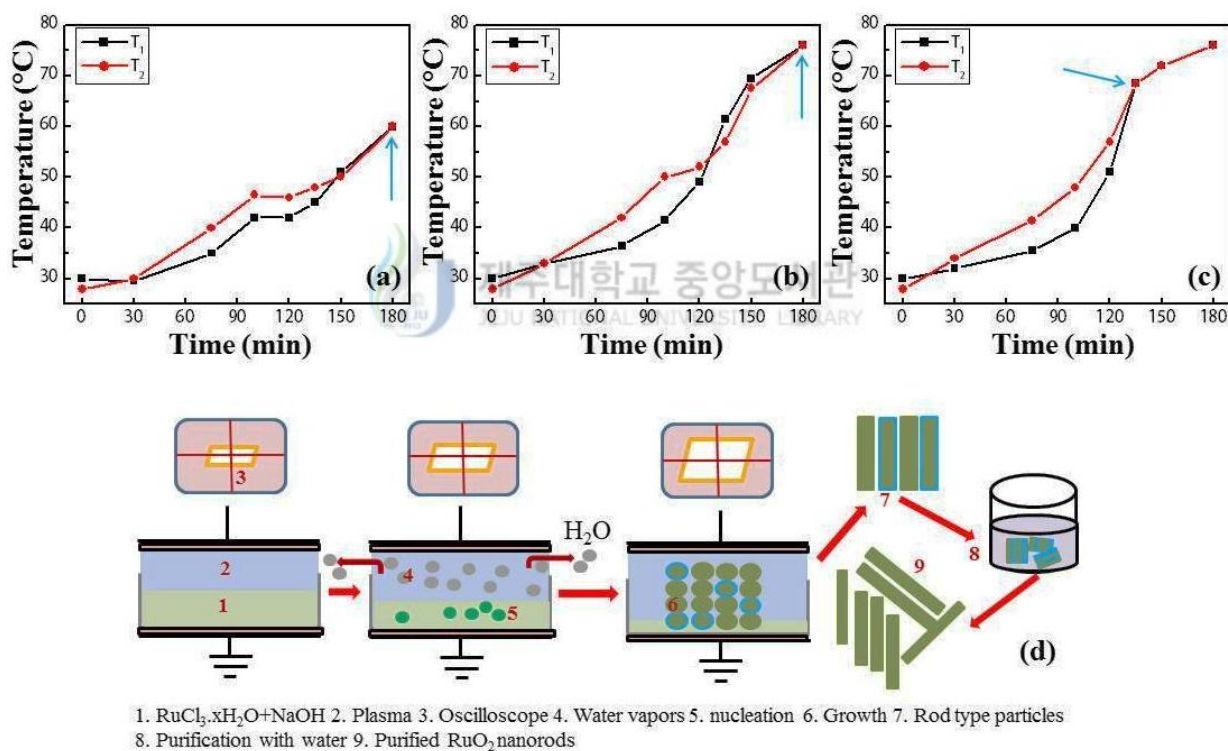


**Figure 3.6.** Temperature-time plots during RuO<sub>2</sub> synthesis in the presence of Ar + H<sub>2</sub> (a), Ar + O<sub>2</sub> (b) and Ar (c). [ $T_1$  and  $T_2$  are the temperatures at the center of the reactor and near the solution, respectively]. The process and the mechanisms of nucleation and growth in Ar plasma (d).

It is to be noted that such fluctuations could be an important parameters to affect the growth of nanoparticles. When Ar + H<sub>2</sub> was used as the feed gas [Fig. 3.6 (a)], maximum temperature inside the plasma reactor was around 60°C whereas for Ar + O<sub>2</sub> and Ar, it was 76°C [Figs. 3.6 (b) and (c)], respectively. For Ar + H<sub>2</sub>, complete water evaporation was achieved at the end of 3 h, whereas for the other cases, it took 2 h. On comparing the generation of temperature according to the gas composition, it is understood that the aggregated RuO<sub>2</sub> NMs obtained with Ar + H<sub>2</sub> may be attributed to the temperature inadequacy. But in the other cases, the maximum temperature of about 76°C was reached, which may be an optimum value required for attaining efficient nucleation and thus specific morphology. It seems that reaction is shifting from physical to chemical to thermal in time.

### 3.1.7 Possible chemical reaction mechanism mediated by plasma species

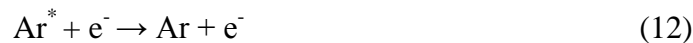
Other than temperature effects, possible plasma reactions in determining the morphology of RuO<sub>2</sub> NMs were analyzed from the literature. Reactive species such as energetic electrons, ions and radicals are generated in the plasma due to collisional ionization and dissociation. The density and the composition of the species mainly depend on the applied electric power and the feed gas composition. The growth kinetics of the NMs is controlled by transport coefficients of the plasma species. When Ar and H<sub>2</sub> are used as the feed gas constituents, the following gas-phase reactions [20] may occur:





The electron-impact ionization, dissociative electron-impact excitation and charge-transfer reactions produce H-ionic species such as  $\text{H}_2^+$ ,  $\text{H}_3^+$  and  $\text{H}^\bullet$ . Further,  $\text{ArH}^+$  ions also create H-atom by reacting with electrons. The above formed H-ionic species and H radicals may also increase the production of condensed HCl along with NaCl, which might have an influence on the morphological control. The addition of  $\text{H}_2$  to Ar leads to changes in the plasma discharge such as shift in the electron energy distribution function (EEDF) and decreases in the densities of metastable Ar,  $\text{Ar}^+$  and  $\text{e}^-$ . It causes asymmetric charge transfer and ion flux which in turn decrease or hinder the progress in the electrical current and thus resultant temperature [30]. In addition,  $\text{H}_2$  reduction leads to the formation of  $\text{H}_2\text{O}$  molecules at the interfaces of Ru clusters which may reduce the temperature and increase the aggregation of the particles.

For Ar +  $\text{O}_2$  mixture,  $\text{Ar}^*$  dissociate  $\text{O}_2$  molecule at a high rate, and thus a substantial decrease in the  $\text{Ar}^*$  density was reported [22] as follows:



The enhanced O species may further form non-stoichiometric oxides on the surface of Ru as observed in the XPS spectra. In addition, the electron impact excitation of O atoms produces O (3s), O (5s) and O (5p) with photon emissions at 130, 136 and 777 nm, respectively, during their relaxation processes. Such UV and VUV fluxes are basically used for breaking the bond in

the Ru precursors exothermically. The crater-like structure in the RO NP samples may be ascribed to the ‘spouting out’ of water vapors during heat treatment [23].

In the Ar-only case, major energy loss mechanisms are electron collision and wall quenching. Internal energy minimization or the dissipation of electron energy is mainly utilized for the evaporation of the solvent. Uniform growth is controlled by the accumulation of the negative charges on the surface of the Ru hydroxide nuclei which effectively prevent further aggregation during the ageing process. Since Ru hydroxide is capable of accumulating more charges when it is used in the aqueous condition, agglomeration is strongly prevented and a defined morphology is attained in the presence of plasma. The creation of a positive potential in the plasma region (during the half cycle of AC voltage) and the net negative charge on the nucleated Ru particles effectively form a potential gradient which drives the growth towards 1D rod like morphology. This is schematically represented in figure 8 (d). Since Ar is an inert gas, it is expected that no noteworthy surface chemical modifications occurred on the NMs except for the morphological control.

*In summary, an investigation of the possibility to use the DBD plasma reactor to synthesize RuO<sub>2</sub> NMs with different morphologies was carried out. It was observed that feed gases (such as Ar + H<sub>2</sub>, Ar + O<sub>2</sub> and Ar) used for plasma generation control the final morphology. Experiments conducted in the absence of plasma showed only aggregated structures which indicated that plasma reactions are essential to achieve various morphological features. Post plasma treatments of RuO<sub>2</sub> NMs prepared by wet chemical method did not show any morphological changes except the degree of aggregation. It is concluded that Ar plasma was effective for obtaining uniform 1D RuO<sub>2</sub> nanostructured materials. Eventually, apart from the environmental applications, the potential of the DBD plasma for the synthesis of one dimensional nanostructured materials looks significant.*

## 3.2 Effect of substrates on the plasma synthesis of RuO<sub>2</sub>

### 3.2.1. Structure and composition analysis

Figure 3.7 (a) represents the XRD spectra of the RuO<sub>2</sub> NMs prepared when Ar + O<sub>2</sub> plasma was used. The prominent diffraction peaks at the diffraction angles (2θ) of about 28.0°, 34.9°, 39.6° and 54.0° correspond to (110), (101), (200) and (211) set of lattice planes, respectively, which represent the rutile type RuO<sub>2</sub> (JCPDS card no.88-0322). Depending on the substrates and the inlet gas used, structural changes were noted especially for one dimensional nanostructures in which (101) plane intensity was higher than (110) plane [19]. Usually for spherical and mixed morphologies (will be discussed in section 3.2.2), predominant diffraction peak at 28° referring to (110) plane is always higher than any other peaks [24]. Similar trend was noted for RuO<sub>2</sub> NMs prepared under Ar plasma. The atomic percentage of Ru and O were calculated to be 30.07 and 69.93, respectively by EDX analysis (Fig. 3.7 (b)). Figure 3.7 (c) displays the XPS survey spectra of the Cu AO sample (table 5), in which the characteristic peaks belonging to Ru 3d, Ru 3p and O 1s indicated the formation of RuO<sub>2</sub>. In order to identify the nature of oxides on the surface, high resolution core level Ru 3p<sub>3/2</sub> spectra were taken and deconvoluted using Gauss-Laurentian peak fitting program (Fig. 3.7 (d)). Two peaks at the binding energy values of about 462.8 and 465.0 eV correspond to ruthenium dioxide and higher oxides of ruthenium. The atomic percentages of RuO<sub>2</sub> and RuO<sub>x</sub> calculated from the areas of the peaks were found to be 66.6 and 33.4, respectively [25,26]. It is thought from our earlier studies that chemical composition will not change to a greater extent (except for a slight variation from RuO<sub>2</sub> to the formation of minor amount of RuO<sub>3</sub>) when different substrates were used since the post synthesis processes such as cleaning and heat treatment were same for all samples.

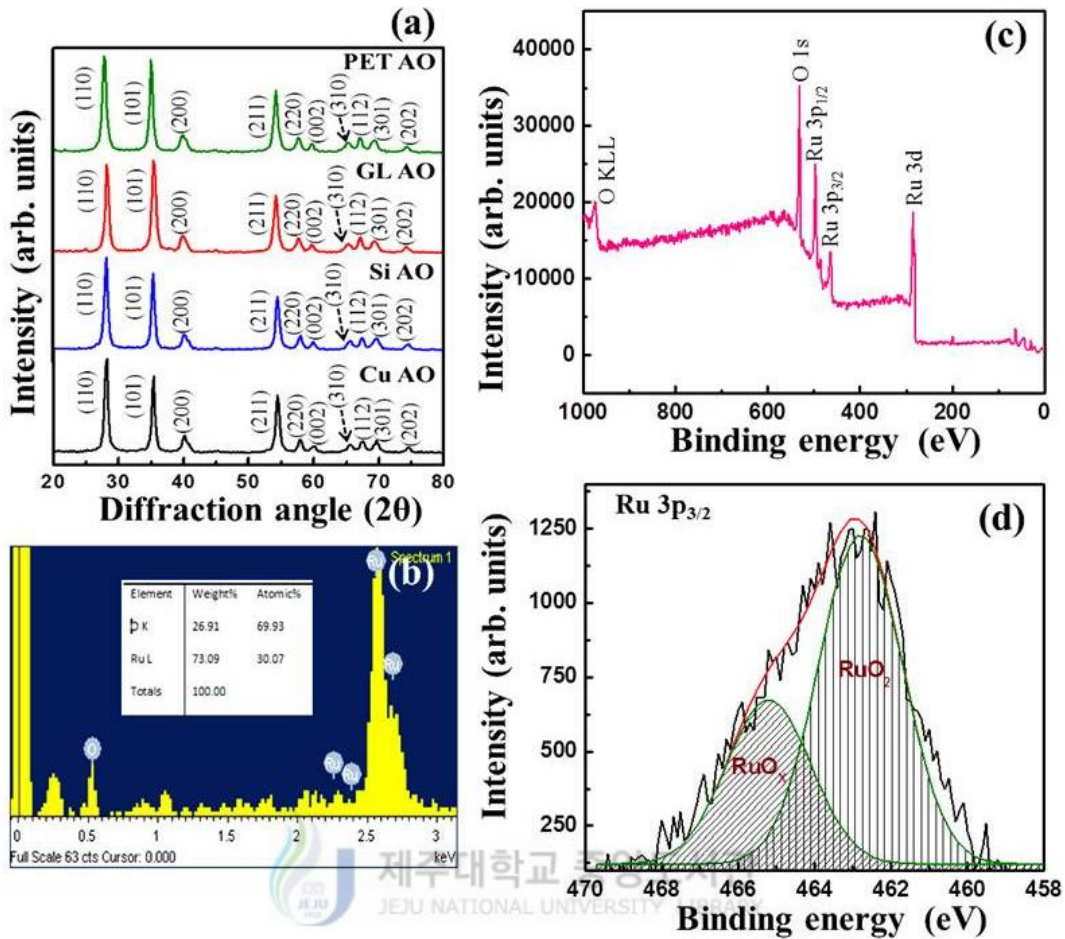


**Figure 3.7.** Characterization results of RuO<sub>2</sub> NMs prepared in the presence of Ar + O<sub>2</sub> plasma. (a) XRD spectra (Cu, Si, GL and PET refers to copper, silicon, glass and polyethylene terephthalate substrates), (b) EDX data, (c) XPS survey spectrum, and (d) high resolution core level spectrum for Ru 3p<sub>3/2</sub> taken for Cu AO sample.

### 3.2.2 Morphological studies

#### 3.2.2.1. Preparation of RuO<sub>2</sub> NMs using different substrates under Ar plasma

Figures 3.8 (a)-(d) show the observed morphology of the RuO<sub>2</sub> NMs corresponding to the samples Cu A, Si A, GL A and PET A, respectively prepared under Ar plasma. The RuO<sub>2</sub> NMs grown on the copper substrate exhibited self-assembled non-uniform spherical structure. On the other hand, the NMs grown on the silicon, glass and PET substrates exhibited various one-

dimensional (1D) morphologies such as tip-broken dense nanostructures, flower-shaped uniform nanosheets and nanonetworks, respectively. The length and the width of nanosheets and networks were observed to be  $>1 \mu\text{m}$  and  $<100 \text{ nm}$ , respectively. From the figures, it is obvious that morphology of NMs can be altered by varying the substrate material. Since the reaction time and condition for all the substrates were maintained identical, the changes in the morphology must have resulted from the substrate materials. In other words, the nature of the substrate is one of the key parameters to determine the morphological structure. The substrates explored in this work can be classified into conductor, semiconductor and insulator. The substrates grouped into insulator resulted in 1D morphology, probably due to the so-called electrostatic trapping phenomenon [27] that is usually observed in vacuum deposition processes. In such processes, insulating materials serve as a nucleation site for the formation of rod-shaped 1D NMs. As presented in Table 4, the thermal and electrical conductivities of the substrates differ from one another, which gave important information on the heat and electrical conduction of the substrate materials under the plasma discharge condition. Apart from the chemical and electrical interactions [28], the energy gained from the plasma constituents is dissipated as heat, which increase the solution temperature, i.e., the vapor pressure of water, eventually leading to the evaporation of water. Subsequently, the nucleation of the particles and further growth take place, based on the heat surrounding of the medium established by the thermal conductivity of the substrate. When using Ar for the creation of plasma, two dominant processes such as electron collision and wall quenching give rise to the accumulation of negative charges on the surface of the ruthenium particles, which can effectively hinder the aggregation during ageing. Such charge accumulation usually results in the 1D morphology at  $76^\circ\text{C}$  reactor temperature.

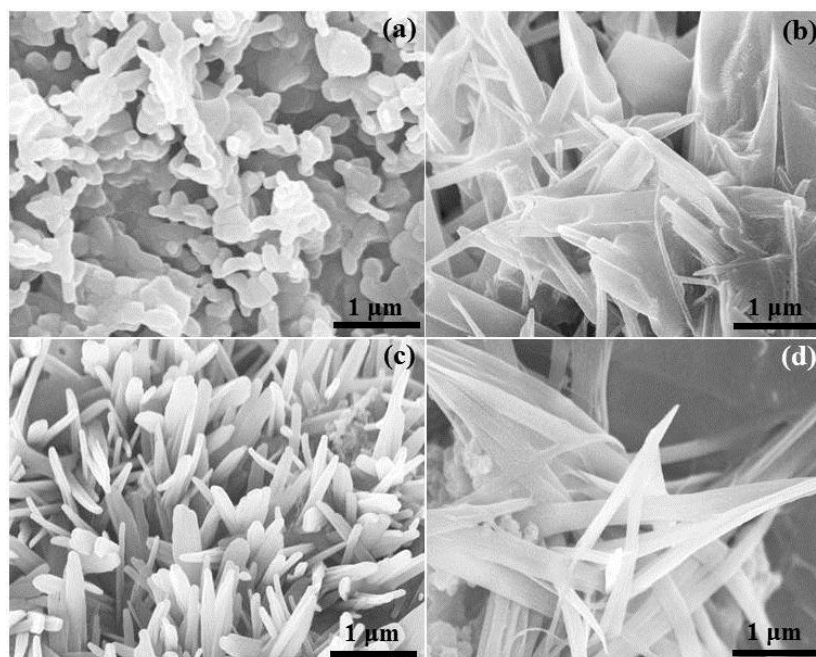


**Figure 3.8.** Effect of substrate materials such as (a) copper, (b) silicon, (c) glass and (d) PET on the morphology of RuO<sub>2</sub> NMs in the presence of Ar plasma.

**Table 4** Conductivity values of the substrates explored at room temperature.

Material	Thermal (W.m <sup>-1</sup> .K <sup>-1</sup> )	Electrical (Ohm <sup>-1</sup> .m <sup>-1</sup> )
Copper	385-401	5.9×10 <sup>7</sup>
Silicon	149	4.3×10 <sup>-4</sup>
Glass	0.82-0.93	10 <sup>-14</sup> -10 <sup>-12</sup>
PET	0.15-0.24	8.6×10 <sup>-17</sup>

### 3.2.2.2. Preparation of RuO<sub>2</sub> NMs using different substrates under Ar + O<sub>2</sub> plasma

Besides the substrate-induced morphological changes of RuO<sub>2</sub> NMs, effect of gas composition was also studied by introducing oxygen along with Ar. Net temperature of around 76°C was also reached with this gas composition. Figures 3.9 (a)-(d) show the observed morphologies of the RuO<sub>2</sub> NMs corresponding to the samples Cu AO, Si AO, GL AO and PET

AO, respectively. When comparing with the Ar-alone case (Fig. 3.8), it can be noticed that the gas composition also plays an important role in determining the morphology. The RuO<sub>2</sub> NMs grown on copper and silicon substrates exhibited aggregated nanostructures with varying degrees, while those grown on glass and PET substrates displayed nanopillar and non-uniform nanorod structures. When the mixture of Ar and O<sub>2</sub> was used, excited Ar molecules dissociate O<sub>2</sub> molecules with a high rate constant [29]. This results in the increase of the highly reactive atomic O species which might form further non-stoichiometric oxides on the surfaces of Ru.

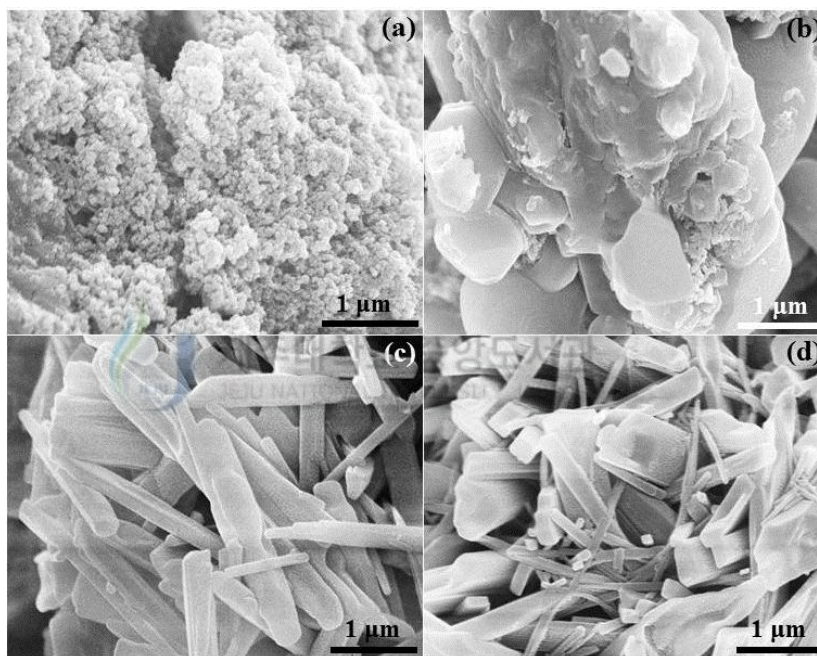


**Figure 3.9.** Effect of substrate materials such as (a) copper, (b) silicon, (c) glass and (d) PET on the morphology of RuO<sub>2</sub> NMs in the presence of Ar + O<sub>2</sub> plasma.

It appears that the DBD plasma reactor is suitable for obtaining spherical/aggregated and rod-type NMs, just like in vacuum deposition processes. In fact, the nucleation and growth mechanisms are similar to each other in many aspects, but it seems the ways they attain the states are quite different. In sputtering processes, applied power, temperature, gas composition (also, pressure) and substrate are the crucial factors to determine the coating characteristics. For

instance, it was reported that RuO<sub>2</sub> nanorods with a length of about 1.4 μm can be obtained by regulating the substrate temperature with higher plasma density and lower oxygen mole fraction [30]. In such vacuum processes, nanorods are formed at high temperatures (400-600°C) which essentially required for the adatom diffusion. Likewise, all the above variables can also affect the DBD process. According to our previous observations, starting the synthesis with less input power caused the whole process to end very slowly, whereas applying too high power could break the dielectric layer. More importantly, starting the synthesis with too high power did not produce any specific morphology because the solvent evaporated much earlier. As mentioned above, the effective reactor temperature is around 76°C, which can be used as an internal temperature parameter. Under this temperature condition, the electrical force between the electrodes drives the nucleated species to align in the axial direction. From the above results, it is thought that input power, temperature, gas composition and substrate type can all have impact on the material's morphology in the DBD plasma reactor.

### **3.2.3. Particle size analysis and zeta potential analysis**

Particle size analysis was performed mainly for the 1D particles of our interest. The average hydrodynamic diameter for each sample is given in Table 5, and the particle size distribution is also shown in Fig. 3.10 in which the diameter of the NMs versus light scattering distribution (%) along with cumulative percentage distribution is represented. Overview of the graphs show the average particle size varies between 231.4 and 353.1 nm for the samples (for spherical types it was about 38.6 nm). The particles with larger size may reflect their length. Further, particles might have hydrated in water, which can explain their presence at higher size range. The average size of the spherical and sheet structures obtained from the particle size analysis once again confirmed the morphological features obtained by FESEM.

**Table 5** Observed morphologies of the RuO<sub>2</sub> NMs obtained by changing the gas composition and the substrate.

Sample name	Feed gas and flow rate (cm <sup>3</sup> min <sup>-1</sup> )	Morphology	Average size (nm)	Zeta potential values (mV)
Cu A	Ar (75)	Aligned spherical	353.1	28.7
Si A	Ar (75)	Broken tip	243.1	26.5
GL A	Ar (75)	Nanosheets	259.3	29.5
PET A	Ar (75)	Networks	338.0	28.1
Cu AO	Ar (60) and O <sub>2</sub> (15)	Spherical	38.6	25.8
Si AO	Ar (60) and O <sub>2</sub> (15)	Stacked bundles	-	-
GL AO	Ar (60) and O <sub>2</sub> (15)	Nanopillar	231.4	27.2
PET AO	Ar (60) and O <sub>2</sub> (15)	Non-uniform rod	320.1	23.3

A: Ar; AO: Ar and O<sub>2</sub>.



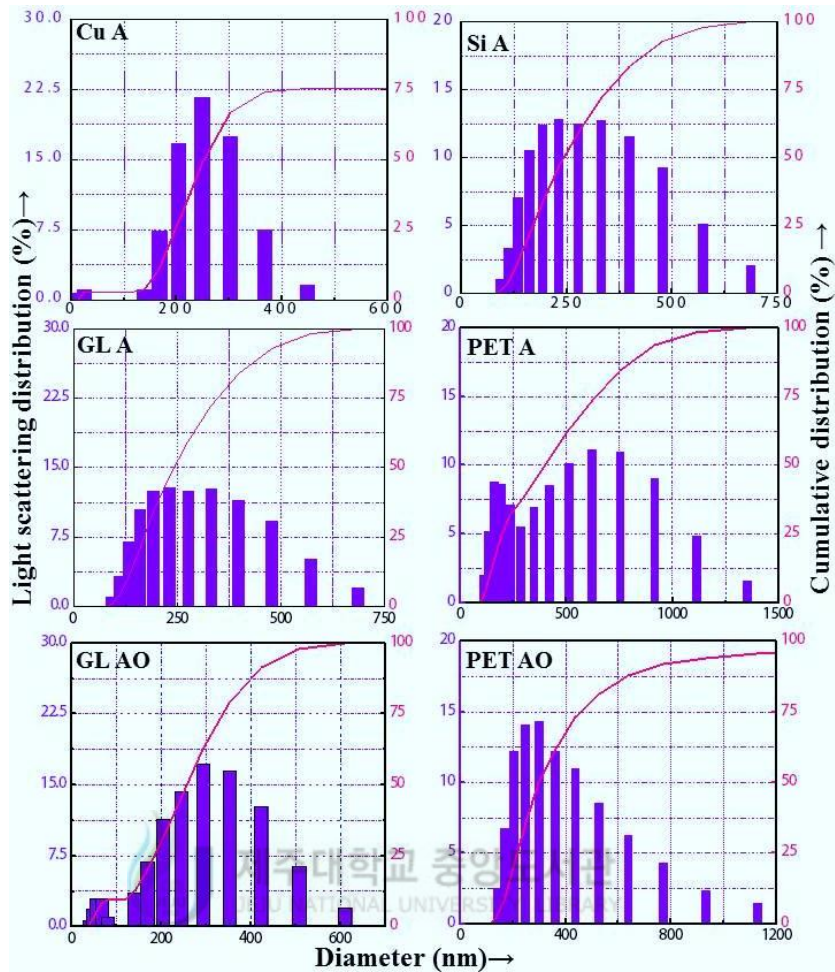


**Figure 3.10.** Particle size analysis histogram of RuO<sub>2</sub> NMs grown on various substrates in the absence and in the presence of oxygen.

The stability of the RuO<sub>2</sub> NMs was analyzed using the surface charge measurements (zeta potential). The experiments were carried out for investigating the aggregation behavior of the particles in potential applications. In suspension state, the electrostatic repulsion between the adjacent charged particles can be identified from the zeta potential. The surface charge values of the Cu A and PET AO samples were found to be about 28.7 and 23.3 mV, respectively. The zeta potential values exhibited by the above samples are very close to the prescribed value of 30 mV for good stability [31]. The zeta potential value of the other specified 1D particles were also given in Table 5.

### 3.2.4. Photocatalytic properties

In order to investigate the property differences arising from the morphological effects, methylene blue dye degradation experiments were carried out by using spherical type (Cu AO) and sheet shaped (GL A) NMs obtained from the plasma reaction. Firstly, the optical band gap of the chosen spherical and sheet-like RuO<sub>2</sub> samples were calculated from their absorption spectrum in the visible region by taking 1.25 mM sample. The absorption coefficient ( $\alpha$ ) was calculated by noting the absorbance value of the samples at 407 nm. The band gap energy was calculated by extrapolating the linear portion of the plot drawn between  $(\alpha h\nu)^2$  and  $h\nu$ . From the plot, the optical band gap for the spherical and sheet-like RuO<sub>2</sub> nanomaterials was found to be 2.69 and 2.62 eV (Fig. 3.11 (a)-(b)). From the literature, optical band gap corresponding to RuO<sub>2</sub> varies between 2.2 and 2.7 eV depending upon the synthesis procedure [32]. The optical emission spectrum of the CFL used for the experiment is given in Fig. 3.12 which showed the wavelength mostly lying in the visible region.

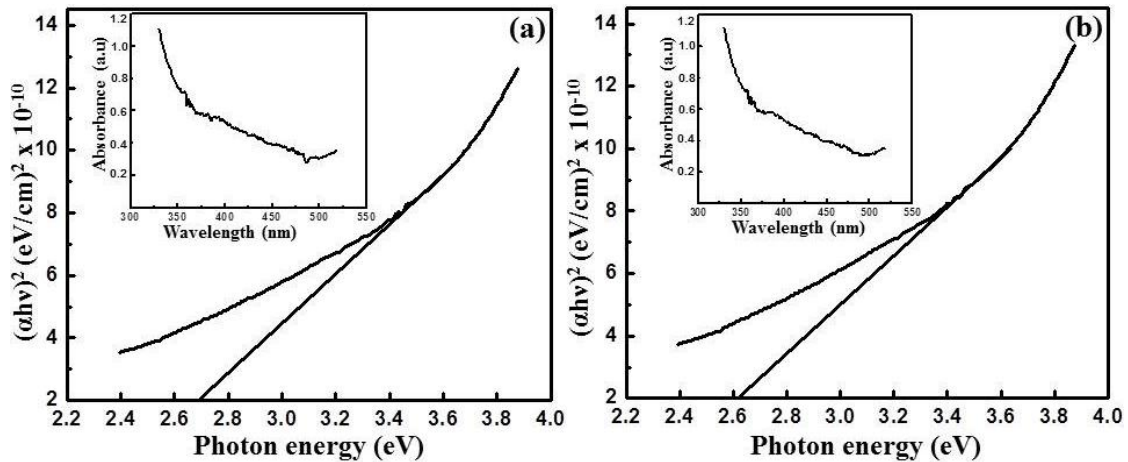


**Figure 3.11.** Band gap calculation by plotting  $(\alpha h\nu)^2$  vs.  $h\nu$  corresponding to spherical (a) and sheet-like (b) RuO<sub>2</sub> nanomaterials. The inset figures show the variation in the absorbance vs. wavelength for the nanomaterials as measured by using UV-visible spectrometer.

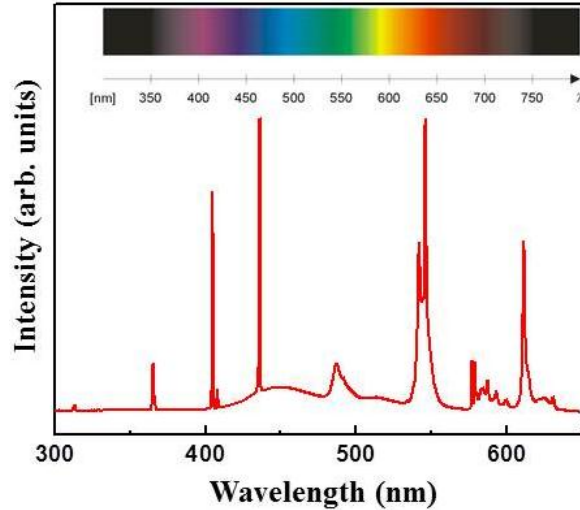


**Figure. 3.12** The optical emission spectrum of the CFL used for the experiment

The UV-visible absorbance spectra of the virgin dye (photolysis) and photocatalyzed MB solution taken at different time of exposure is given in the supporting information (Fig. 3.13). In order to determine the percentage of photodegradation of MB, the following formula was used and plotted in Fig. 3.14.

$$\% \text{ Degradation} = [1 - (C_t / C_0)] \times 100 \quad \text{-----} \quad (15)$$

Where  $C_0$  is the initial concentration of the dye and  $C_t$  is the concentration after degradation. It can be seen from the figure that virgin MB underwent its natural photo degradation of about 16% after 15 h CFL exposure. The percentage of  $\text{RuO}_2$  NMs catalyzed photo degradation was improved much, which was dependent on the amount of NMs loading and shape. It was about 78.26 and 85.51 % degradation was observed for the samples SP 5.0 and SH 5.0, respectively. The difference of about 7.25% is ascribed due to the shape effect which indicates that sheet shaped  $\text{RuO}_2$  NMs were superior as compared with spherical shaped NMs.

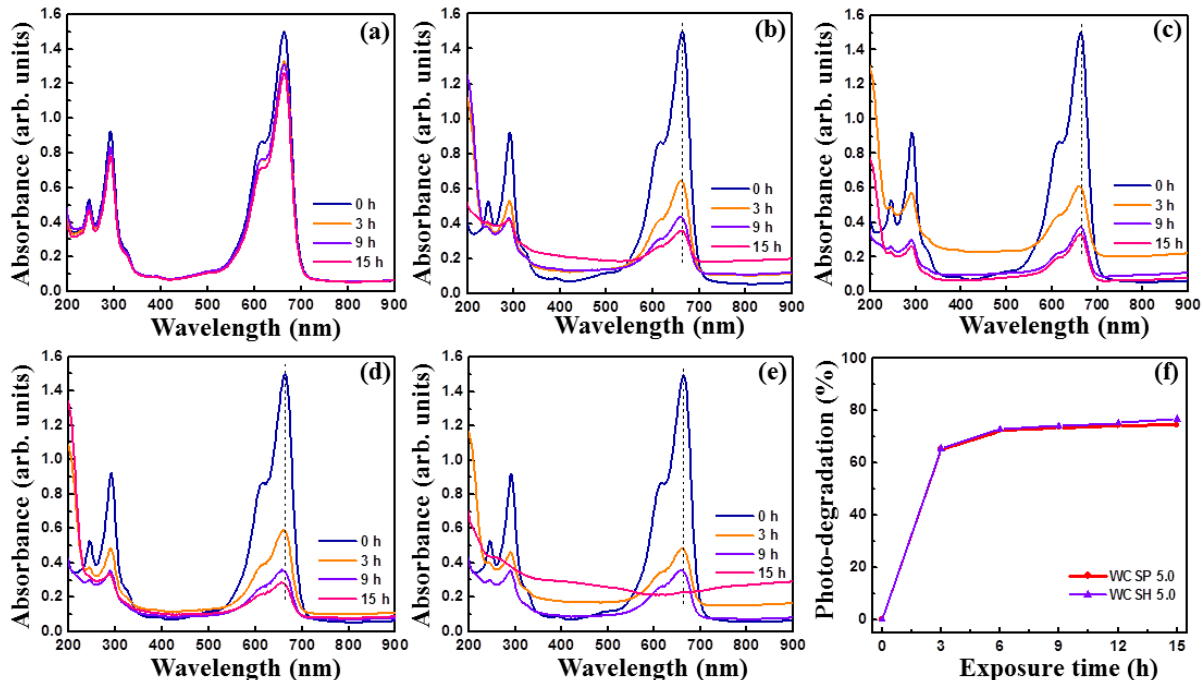


**Figure 3.13** The UV-visible absorbance spectra corresponding to photolysis of virgin dye (a) and photocatalyzed MB solution taken at different time of exposure is given for SP 2.5, SP 5.0, SH 2.5 and SH 5.0 in (b)–(e), respectively. Figure (f) shows the degradation of methylene blue using wet chemically synthesized spherical (WCSP 5.0) and sheet-like (WCSH 5.0) RuO<sub>2</sub> NMs.

The adsorption capacity of the dye molecules on the NMs surface is a critical step in photo-catalysis which is determined from the surface area of the RuO<sub>2</sub> NMs. Figure 3.15 shows the adsorption-desorption isotherm [(a) and (c)] and the multipoint BET plots [(b) and (d)] for SP 5.0 and SH 5.0, respectively as measured by using Quantachrome Instruments (version 2.11). The shape indicates that it belongs to type V isotherm, where the adsorbate-adsorbent interaction potential is small. The pore volume and pore radius of the spherical and sheet-like NMs during adsorption and desorption process are mentioned in Table 6, which confirmed the standard values (1.5-100 nm). The linearity of the data over the relative pressure ( $P/P_0$ ) range 0.1-0.3 assures the suitability of the BET model to determine the surface area of the RuO<sub>2</sub> NMs. The

spherical and sheet shaped nanomaterials exhibit the surface area of about 25.39 and 37.48 m<sup>2</sup>/g, respectively. Even though the difference is very small, enhancement in the activity might be due to the surface structure and electronic properties (band gap) of the NMs [33].

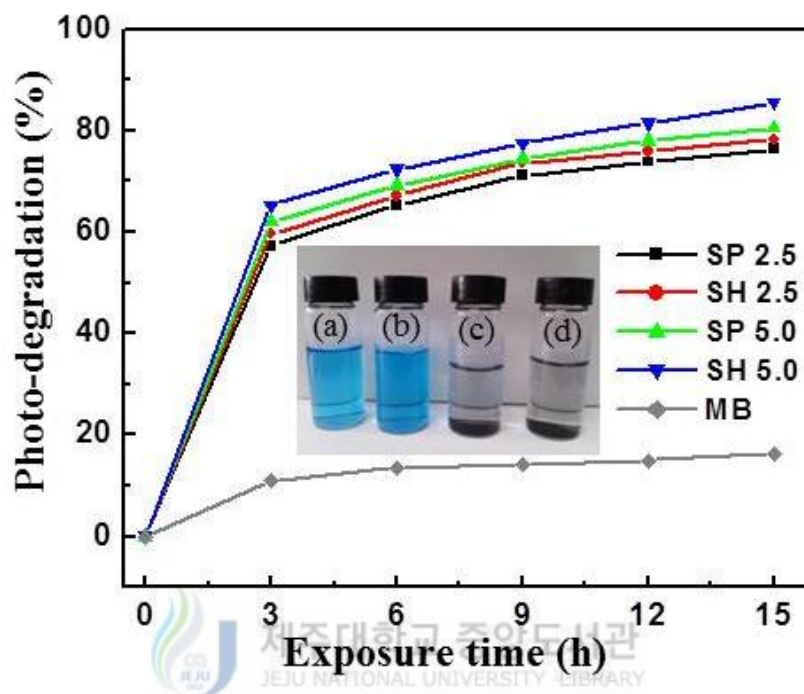


**Figure 3.14.** The comparison of the % degradation of methylene blue versus exposure time using spherical (SP 2.5 and SP 5.0) and sheet-like (SH 2.5 and SH 5.0) RuO<sub>2</sub> NMs. Inset figure shows the virgin methylene blue solution at 0 h (a) and 15 h (b) of CFL exposure (photolysis) whereas (c) and (d) shows the SP 5.0 and SH 5.0 samples after 15 h of exposure, respectively.

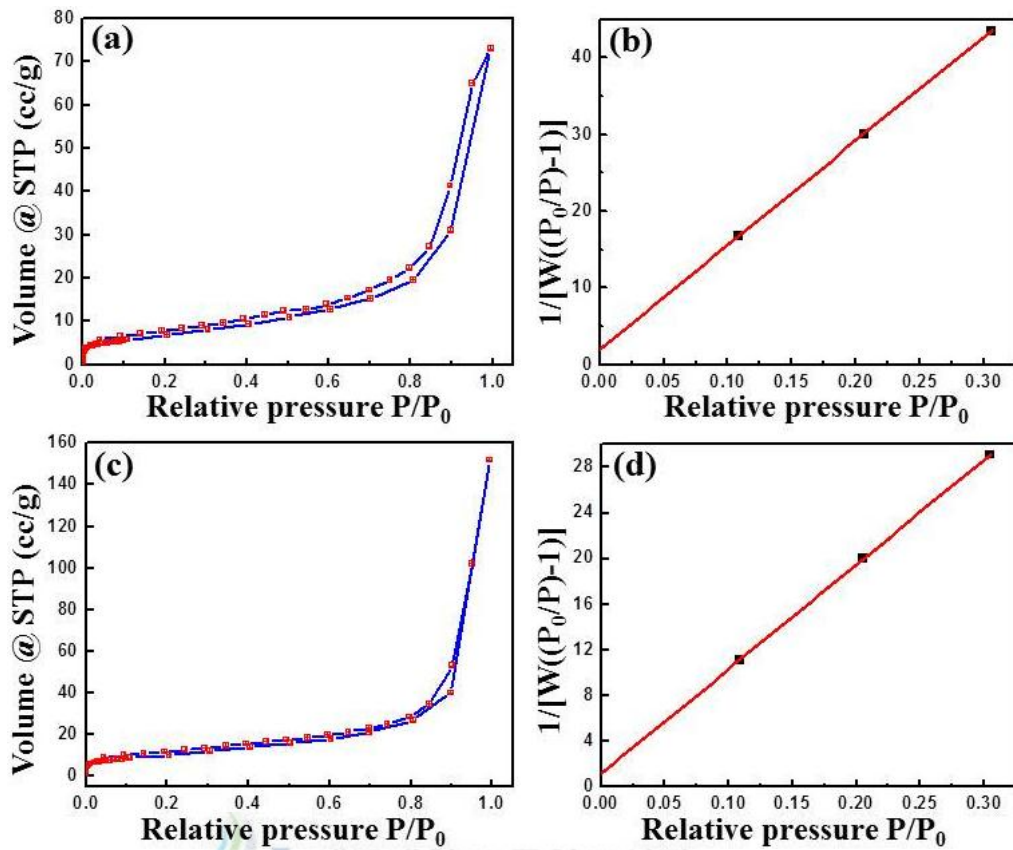
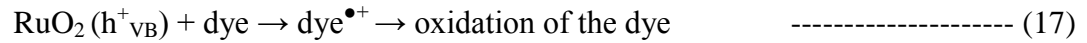
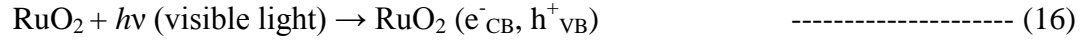


**Figure 3.15.** The adsorption-desorption isotherm (a) and (c) and the multipoint BET plot (b) and (d) observed for spherical (SP 5.0) and sheet-like (SH 5.0) RuO<sub>2</sub> nanomaterials.

**Table 6** Properties of the nanomaterials measured using Barrett-Joyner-Halenda (BJH) method.

Nanomaterials	Process	Surface area (m <sup>2</sup> /g)	Pore volume (cc/g)	Pore radius Dv(r) Å
Spherical type	Adsorption	19.601	0.109	18.392
	Desorption	27.293	0.111	84.188
Sheet-like	Adsorption	25.657	0.227	18.344
	Desorption	33.990	0.229	87.081

After adsorption of the dye molecules, the mechanism of dye degradation under visible light can be explained similar to the UV mediated excitation of the catalyst material as given below [34,35].



Formation of the oxide species such as super oxide ( $\text{O}_2^{\bullet-}/\text{OOH}^\bullet$ ),  $\text{H}_2\text{O}_2$  and  $\text{OH}^\bullet$  radicals originated due to the ejected electrons of the conduction band and valence band holes of the NMs are assumed to be responsible for the degradation of dye .

*The above study investigated the application of DBD plasma for the syntheses of  $\text{RuO}_2$  NMs with different shapes, focusing on the roles of plasma gas composition and substrate material to achieve structure-specific  $\text{RuO}_2$  NMs. The heat conduction and charging mechanism in and out of the substrate might be the reason for the changes in the morphology. The particle size analysis and surface charge measurements confirmed the stability of the prepared particles. The spherical and sheet shaped  $\text{RuO}_2$  nanomaterials exhibited the optical band gap values of about 2.69 and 2.62 eV and tested for methylene blue photo-catalytic performance under visible light exposure. The results showed that sheet shaped nanomaterials exhibited higher activity as compared to spherical types.*

### 3.3 Alternative way of tailoring the morphology of RuO<sub>2</sub>

#### 3.3.1. X-Ray diffraction study for structural analysis

The XRD patterns of SP NPs heat treated from 100 to 350°C are shown in Fig. 3.16. From the spectra, it is possible to elucidate the formation mechanism of RuO<sub>2</sub>. Addition of NaOH with RuCl<sub>3</sub>.xH<sub>2</sub>O forms the precipitate of Ru(OH)<sub>3</sub> at the end of the reaction. Ruthenium (III) hydroxide is unstable and oxidizes in the presence of air during initial heat treatment (100°C drying process) which form RuO<sub>2</sub>. nH<sub>2</sub>O. At this stage the product exhibits amorphous nature with no prominent peaks. Further heat treating the samples up to 350°C causes the complete removal of water molecules and produce crystalline RuO<sub>2</sub> with small presence metallic Ru due to thermal decomposition [36]. The major Bragg reflections at 2θ values around 28.00°, 34.96°, 39.65° and 54.00° correspond to (110), (101), (200) and (211) set of lattice planes of rutile RuO<sub>2</sub>. XRD spectra of SH NPs also displayed the same diffraction pattern (not given here), which may result from the presence of mixed morphology.

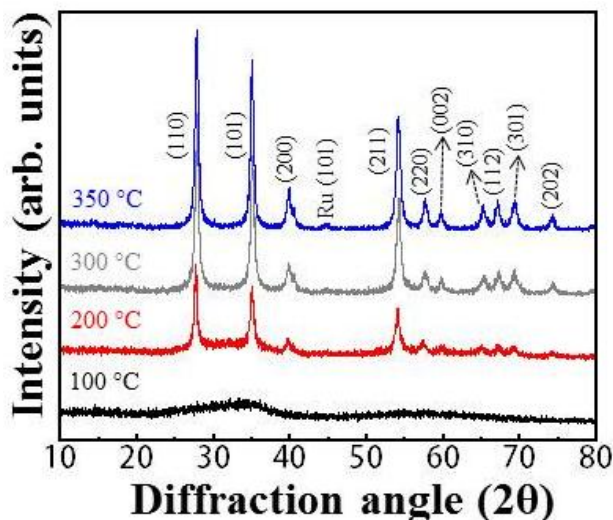


**Figure 3.16** X-ray diffraction patterns of SP NPs after heat treatment at different temperatures.

### 3.3.2. Surface morphological analysis.

Figures 3.17 (a) and (b) represent FESEM images and Figs. 3.17 (c) and (d) correspond to TEM images of SP NPs and SH NPs, respectively. The SP NPs mainly exhibited RuO<sub>2</sub> particle blocks of spherical morphology and the same was observed in TEM (< 50 nm size). On the other hand, SH NPs displayed a ‘sheet like’ structure due to PEG addition which might controlled the growth process. It can be seen from Fig. 3.17 (b), the total length and width of the RuO<sub>2</sub> nanosheets are > 1 μm and 250 nm, respectively. The corresponding TEM image in Fig. 3.17 (d) also showed the nanosheet structures containing sharp tips.

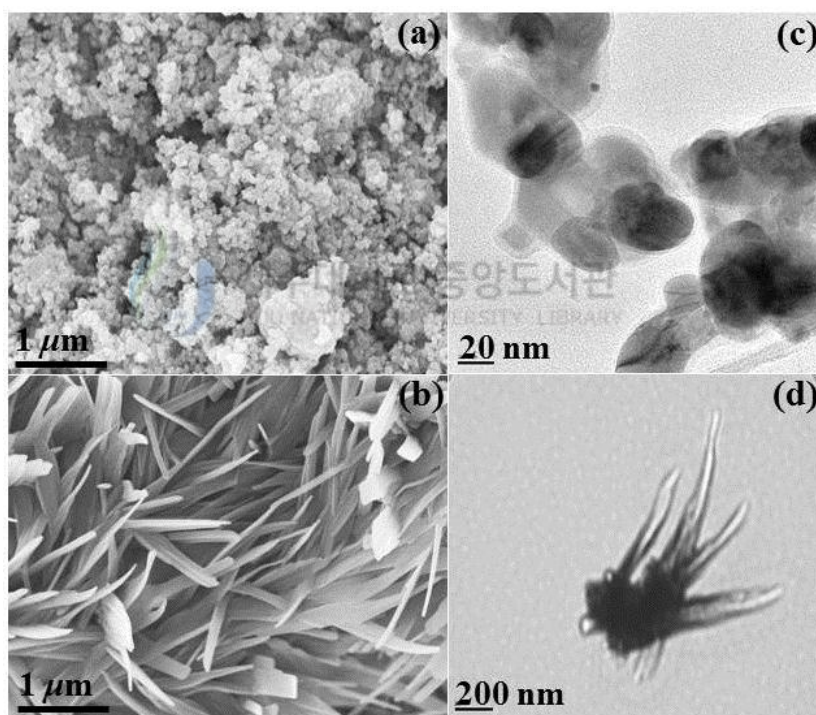


**Figure 3.17** FESEM and TEM surface morphology of RuO<sub>2</sub>: SP NPs [(a) and (c)] and SH NPs [(b) and (d)], respectively.

### 3.3.2.1 Effect of varying concentration of NaOH and PEG on the morphological structure of RuO<sub>2</sub> nanomaterials

It would be more appropriate discussing the morphologies observed during the optimization process. The solution temperature, concentration of NaOH and PEG were noted as important factors affecting the final morphology of RuO<sub>2</sub> nanomaterials. For all experiments, Ru precursor concentration was fixed at 0.1 M. Experiments conducted at room temperature and below 75°C yielded only aggregates of RuO<sub>2</sub> powders with no specific morphology.

Effect of NaOH on the spherical morphology of RuO<sub>2</sub> was studied by varying the concentration such as 0.5, 1.0, 1.5 and 2.0 M. The FESEM images of the observed structures are given in Fig. 3.18 (a)-(d) showing the spherical particles with varying degrees of aggregation. For example, it is obvious to see highly aggregated (Fig. 3.18 (a)) and less aggregated spherical particles (Figs. 3.18 (b)-(d)). From the above observations, reaction between 1 M NaOH and 0.1 M RuCl<sub>3</sub>.xH<sub>2</sub>O was taken as an optimized parameter for obtaining RuO<sub>2</sub> with spherical morphology.

The effect of PEG on the sheet like morphology was studied by varying the amount of PEG such as 0.2, 0.4, 0.6 and 0.8 g (each dissolved in 20mL H<sub>2</sub>O), keeping 1 M NaOH constantly in order to find out the surfactant induced changes. Addition of PEG did not affect the pH (~10) value. When 0.4 g of PEG was used, most of the RuO<sub>2</sub> (around 65%) nanomaterials exhibited sheet like morphology (Fig. 3.18 (f)) but other compositions yielded low or dense sheet-like structures (Fig. 3.18 (e), (g)-(h)). It was inferred from the above optimization process that addition of 0.4 g PEG (with 1 M NaOH and 0.1 M RuCl<sub>3</sub>. xH<sub>2</sub>O) at 75°C could yield maximum sheet like structures in RuO<sub>2</sub>.

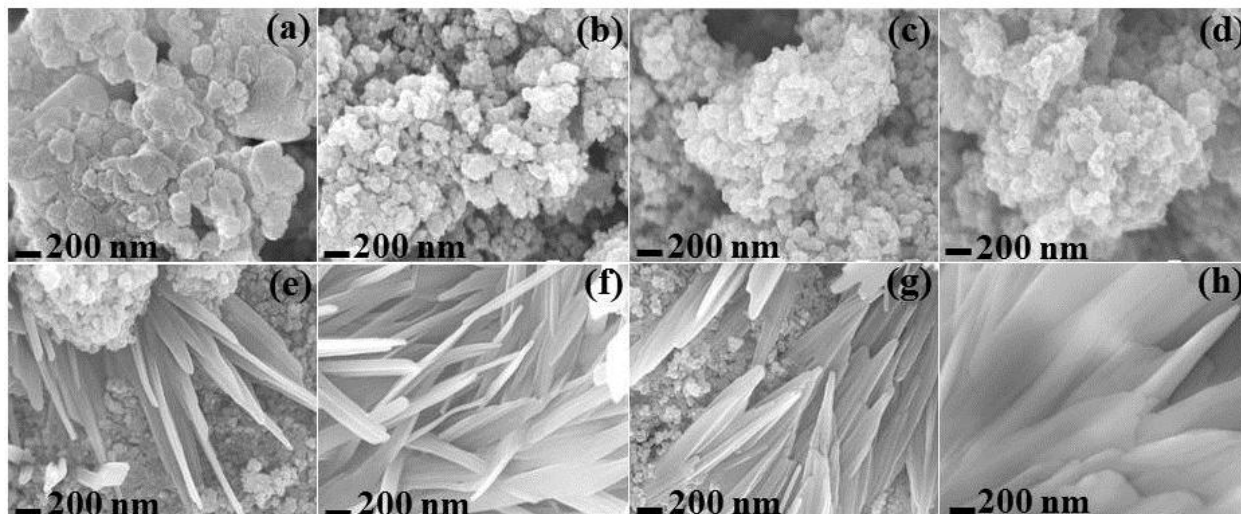


**Figure 3.18** Observed FESEM morphologies of RuO<sub>2</sub> at different experimental conditions.

RuCl<sub>3</sub>.xH<sub>2</sub>O was fixed at 0.1 M for all experiments. Effects noticed when increasing the concentration of NaOH such as (a) 0.5 M, (b) 1.0 M, (c) 1.5 M and (d) 2 M. Effect of surfactant induced growth by varying the concentration of PEG such as (e) 0.2 g, (f) 0.4 g, (g) 0.6 g and (h) 0.8 g (at 1 M NaOH fixed concentration). All solutions were prepared separately in 20 mL H<sub>2</sub>O.

### 3.3.3. Analysis of functional groups using FT-IR spectroscopy

The FTIR spectra of SP NPs and SH NPs are given in Figs. 3.19 (a) and (b). On observation, it brought out the spectral regions correspond to oxide and water molecules. The lattice and the surface vibration between Ru metal and the oxygen atom can be traced in the region defined by their fundamental frequency. The metal-oxygen (M-O) vibration or the perturbation region was observed around 650-800 cm<sup>-1</sup> in which the lattice vibration expressed the oxygen content in the form of oxides. The vibrational frequency of Ru-O bond depends on the co-ordination number of Ru metal atom. Characteristic bands over 3200 cm<sup>-1</sup> resulted from the surface hydroxyl groups and uncompensated water vapor bands [37]. Peaks at 1068 and 1300-1400 cm<sup>-1</sup>

attributed to the vibration of C-OH stretching mode and C-O-H in-plane deformation [38]. The reduction in the intensity of OH and the absence of C-OH bands are clearly visible in SP NPs in which no PEG was added.

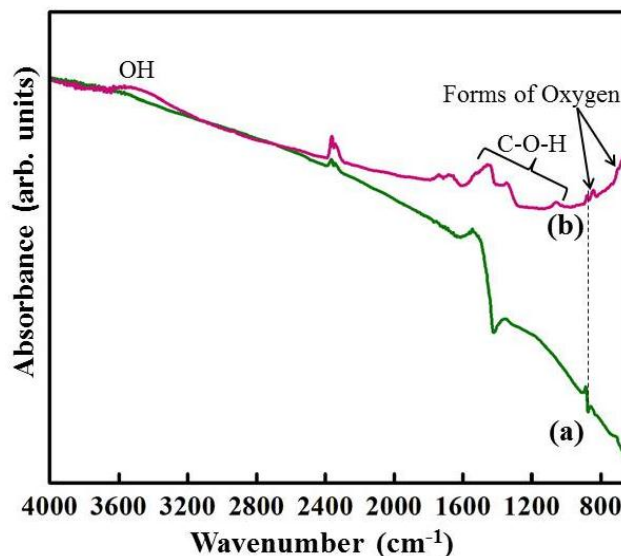


Figure 3.19 The FTIR spectra of SP NPs and SH NPs.

### 3.3.4. XPS surface chemical analysis

Typical XPS survey spectrum for SH NPs is given in Fig. 3.20. The characteristic peaks correspond to Ru 3d, Ru 3p and O 1s regions were detected. Figures 3.21 (a) and (b) refers to the high resolution core level Ru 3d spectra of SP NPs and SH NPs, respectively. Both spectra exhibited three regions at the binding energy values of 286.0, 284.2 and 284.6 eV corresponding to ruthenium oxides, small amount of metallic Ru and carbon [39,40], respectively. Since the binding energy of carbon also falls closely with Ru 3d, Ru 3p peaks were fitted for obtaining accurate results which are given in Fig. 3.21 (c) and (d). As can be seen from the spectra, the prepared nanomaterial consisted mainly of ruthenium dioxide (463.2 eV) and ruthenium oxides (RuO<sub>3</sub> at 465.0 eV). Corresponding O 1s spectra for SP NPs and SH NPs are also shown in Figs. 3.21 (e) and (f), respectively. The oxygen spectra showed the presence of ruthenium oxides at

529.3 and 530.7 eV [41,42] and the presence of less intense water molecules which might have resulted by water adsorption from the atmosphere prior to XPS measurement [43].

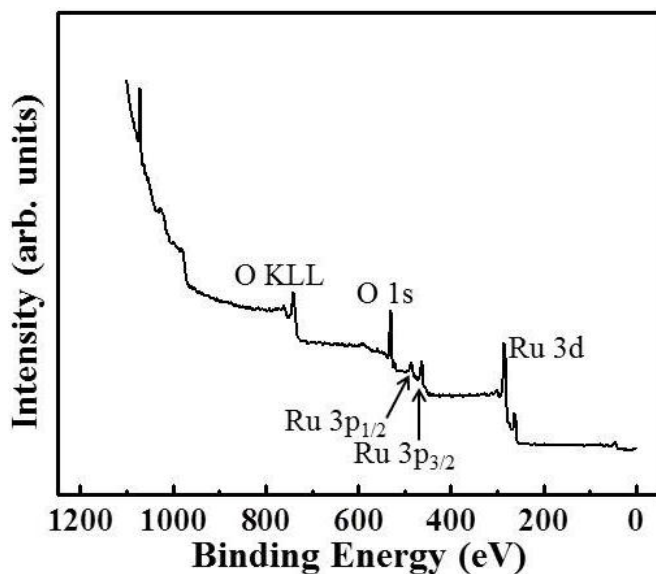


Figure 3.20 XPS survey spectrum for RuO<sub>2</sub> (SH NPs).

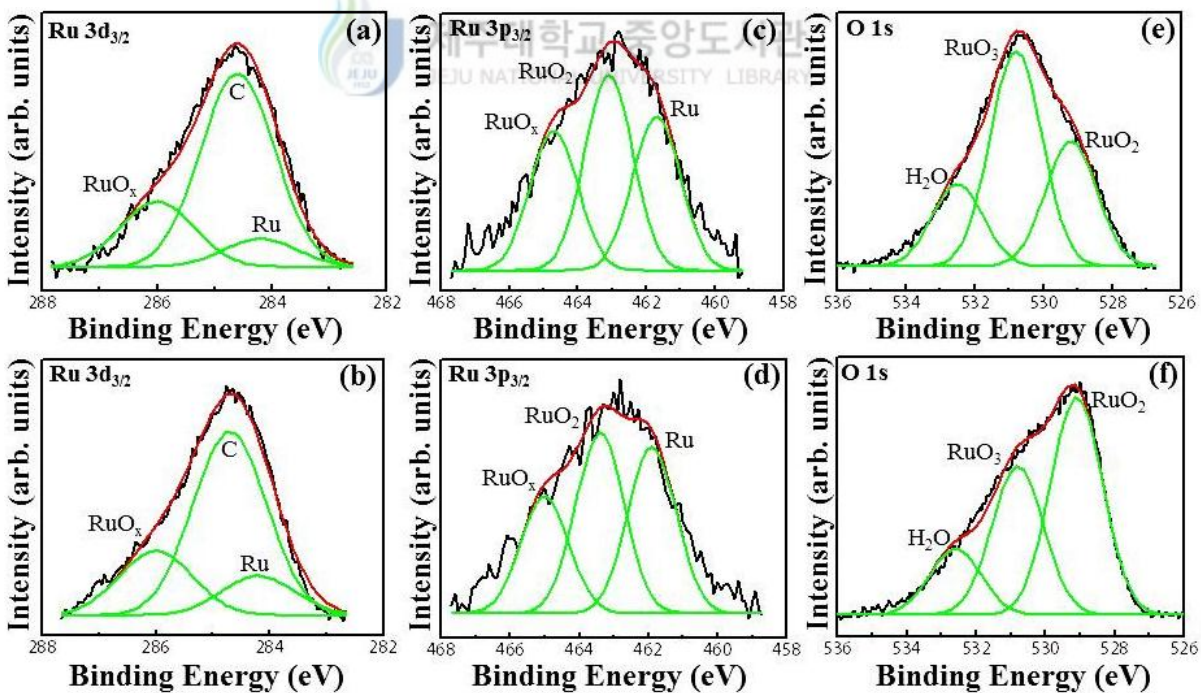


Figure 3.21 XPS high resolution core level spectra of SP NPs and SH NPs: Ru 3d<sub>3/2</sub> [(a) and (b)], Ru 3p<sub>3/2</sub> [(c) and (d)] and O 1s [(e) and (f)].

### 3.3.5. Stability of RuO<sub>2</sub> nanomaterials

The stability of SP NPs and SH NPs were analyzed by measuring its surface charges (zeta potential) after dispersion in pure water at 25°C. In a suspension state, repulsion between the adjacent particles by charging can be identified from the zeta potential. As can be seen from Figs. 3.22 (a) and (b), the prepared SP NPs and SH NPs exhibited the surface charge values of about 25.36 and 23.35 mV, respectively. The zeta potential values exhibited by the particles are close to the prescribed value shown in the literature [44]. The particle size analysis showed the hydrodynamic diameter of SP NPs was well below 150 nm (Fig. 3.22 (c)). Small fraction of the particles might have hydrated easily in water and could be the reason for their presence at higher size range [45] as compared to the sizes observed in microscopic techniques. But the SH NPs spanned a wider range (greater than 65% of the particles lies above 600 nm) which may due to sheet shapes (Fig. 3.22 (d)). The above studies provided the information related to RuO<sub>2</sub> nanomaterials' stability and agglomeration phenomena in aqueous solution which is essential for attachment of nanomaterials with bacterial surfaces.

### 3.3.6. Shape dependent anti-microbial effects of RuO<sub>2</sub> nanomaterials

Inhibitory effect of the RuO<sub>2</sub> nanomaterials [SP NPs and SH NPs] against four pathogenic bacterial species is shown in Fig. 3.23. The positive control curve for all pathogens showed a sigmoidal growth pattern with logarithmic phase between 0 and 24 h and the negative control did not show any growth. Among the four bacterial species *V. anguillarum* and *E. tarda* (Gram-negative) evidenced a significant growth inhibition ( $P < 0.05$ ) at all the three concentration as compared to other two Gram-positive pathogens (*S. iniae* and *S. parauberis*), which recorded the growth inhibition only at higher concentration (75 µg/mL).

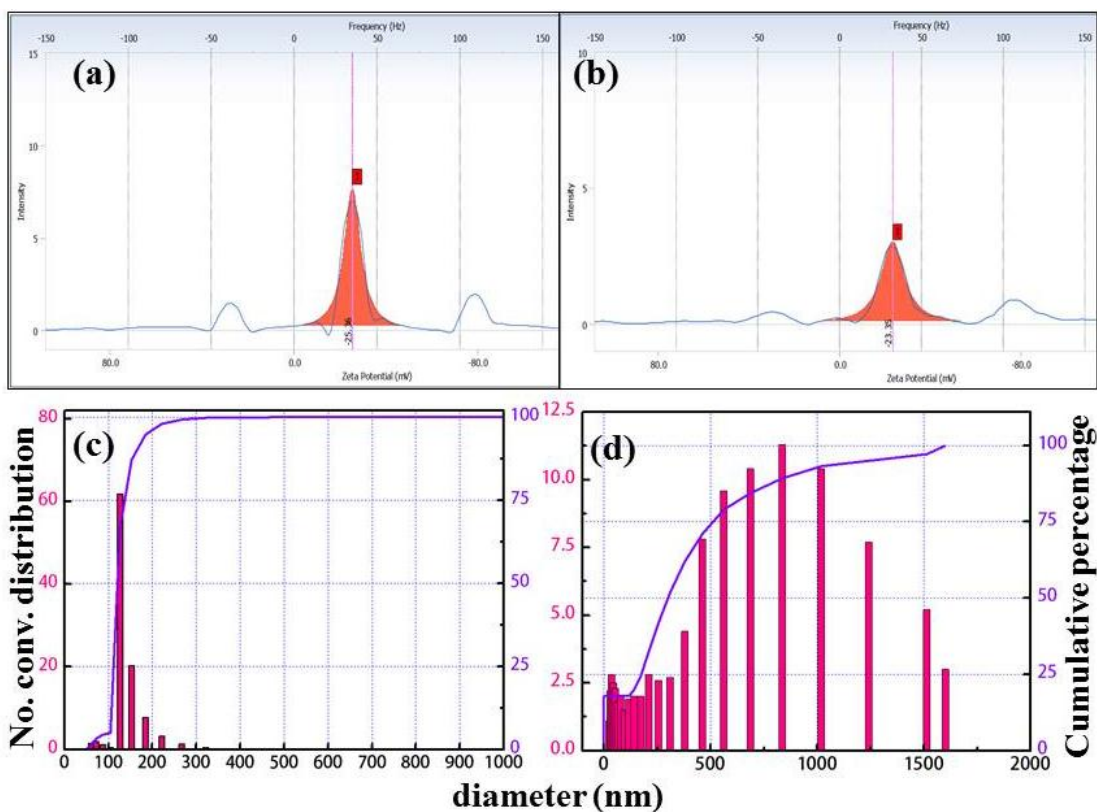


**Figure 3.22** Zeta potential studies for SP NPs (a) and SH NPs (b). Particle size analysis performed to SP NPs (c) and SH NPs (d).

The reason could be due to the differences in their structure of the cell walls. The Gram-negative bacteria have lipopolysaccharide (LPS) layer at the exterior, followed underneath by a thin peptidoglycan layer of thickness about 7-8 nm [46]. Even though LPS layer composed of covalently linked lipids and polysaccharides, they lack rigidity and strength. The negative charges on the LPS are attracted towards weak positive charges (as measured in zeta potential) possess by nanomaterials [47]. On the other hand, the cell wall of Gram-positive bacteria is principally composed of peptidoglycan layer (linear polysaccharide chains cross-linked by short peptides which form a three dimensional rigid structure) of thickness around 20-80 nm [48]. The rigidity and extended cross-linking not only supports the cell walls but also making difficult to the nanomaterials for penetration and damage. The extent of inhibition of bacterial growth

reported in this study with RuO<sub>2</sub> nanomaterials was dependent on the concentration and their physical structure. In comparison with the spherical shaped RuO<sub>2</sub> nanomaterials, the SH NPs is highly sensitive towards all the tested bacteria which may be due to the penetration capability of the hierarchical structures. However, the inhibitory effect of standard Ag nanoparticles (10 μg/mL) was significantly higher (P<0.001) when compared with RuO<sub>2</sub> nanomaterials.

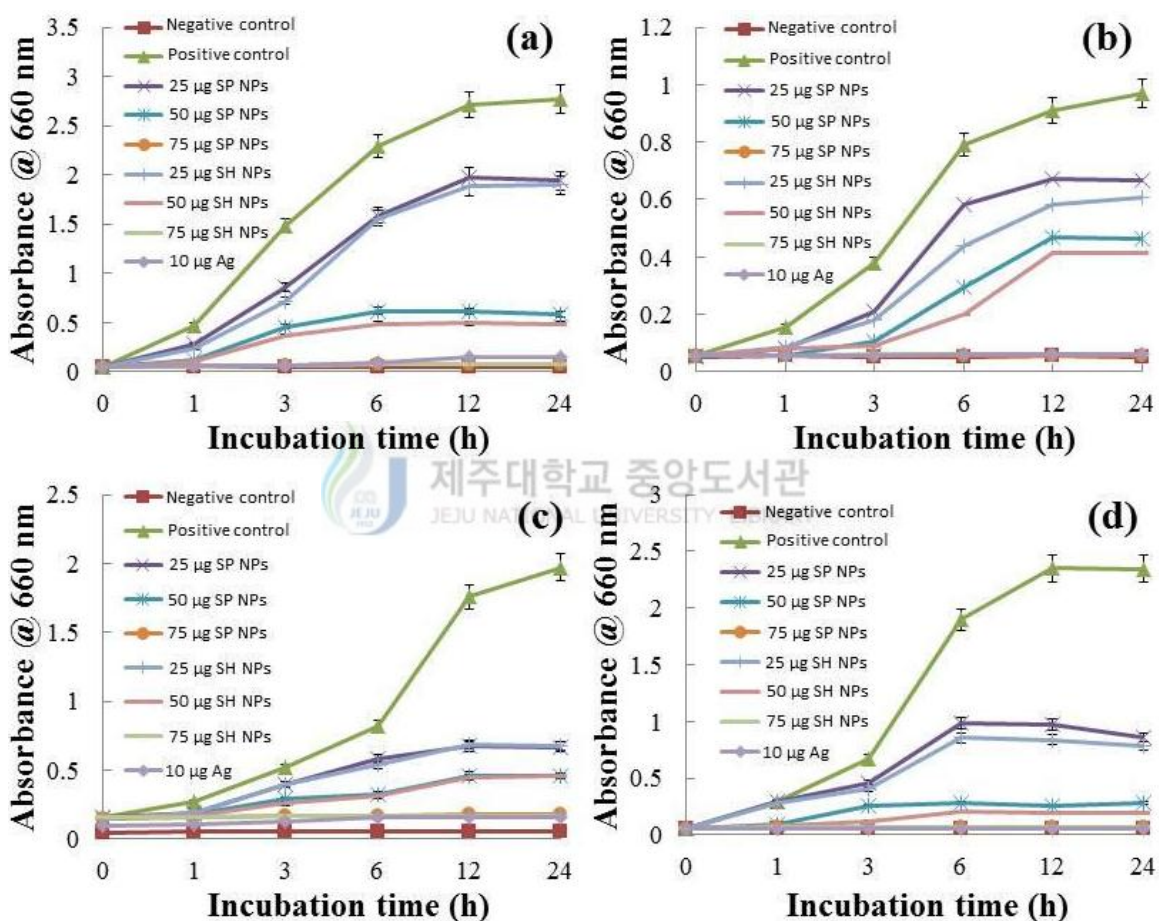


**Figure 3.23** The O.D. values measured using UV spectrophotometer representing the bacterial growth curves for (a) *S. parauberis*, (b) *S. iniae*, (c) *E. tarda* and (d) *V. anguillarum* when interacting with SP NPs and SH NPs at different concentrations. Positive control refers to bacteria in nutrient broth; Negative control refers to nutrient broth; Standard control refers to 10 μg Ag (silver) nanoparticles in nutrient broth.

In order to probe the effect of RuO<sub>2</sub> nanomaterials, FESEM images were taken to analyze the damages occurred to the bacterial surface. Figure 3.24 shows the surface morphological images of *E. tarda* and *S. iniae* taken before [(a) and (b)] and after [(c) and (d)] interaction with SH NPs. The images clearly revealed the damages caused to the cell membrane along with adsorbed RuO<sub>2</sub> nanomaterials on the entire surface. It is obvious to see the catastrophic damage occurred to *E. tarda* as well as surface pits on *S. iniae*. Similar damage in the cell membrane of Gram-negative bacteria by silver nanoparticles has been reported previously [49]. The EDS mapping was carried out to confirm the adsorbed materials on the bacterial surface. Figures 3.24 (e) and (f) represent the EDS elemental mapping of SH NPs adsorbed on *E. tarda* and *S. iniae* which showed the presence of RuO<sub>2</sub> with its composition at the inset table.

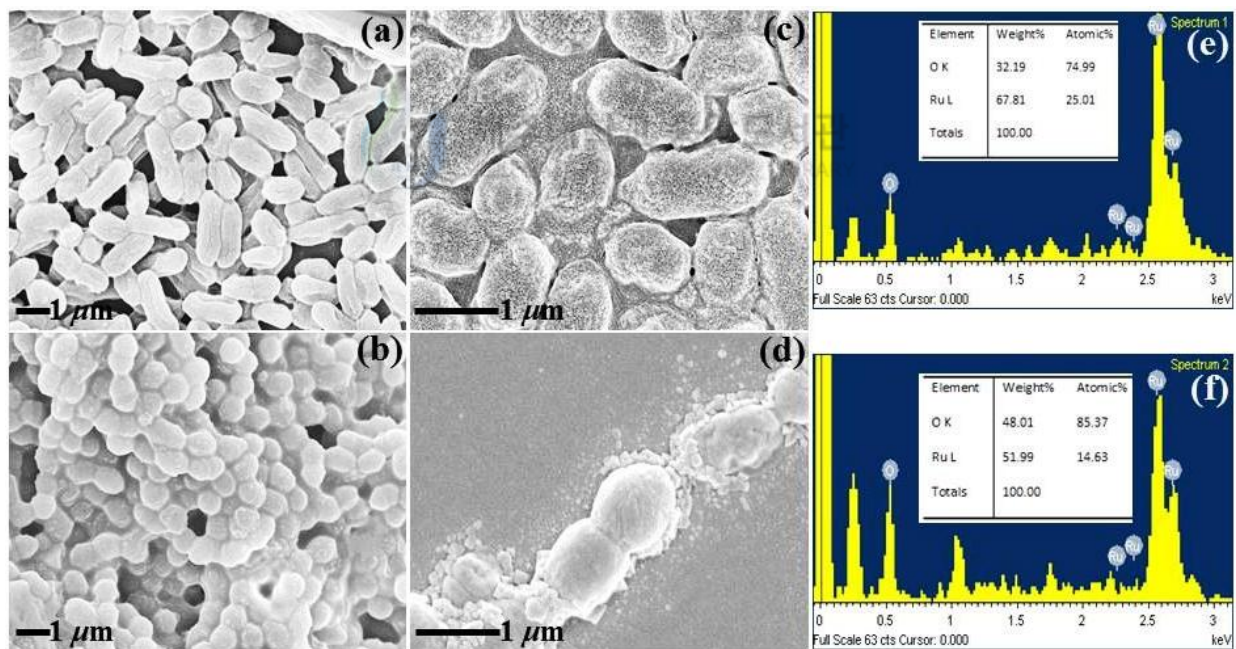


**Figure 3.24** The FESEM surface morphological images of *E. tarda* [(a) and (c)] and *S. iniae* [(b) and (d)] taken before and after interaction with SH NPs, respectively. The ruptured cell walls and the damaged body of the cells can be seen. EDS mapping performed on *E. tarda* (e) and *S. iniae* (f) confirmed the adherence of SH NPs on the surface of the cells.

The mechanism for the antibacterial activity of RuO<sub>2</sub> nanomaterials may be either due to direct contact mechanism or oxidative stress. The former is due to the direct contact occurs between the metal oxide surface and the bacterial cell walls which eventually lead to the disruption of bacterial organelles [50]. The latter may due to the elevated reactive oxygen species levels (ROS) by the exposed nanomaterials. This was confirmed from our studies that TBARS assays showed an increase in the ROS production for *E. tarda* (Fig. 3.25 (a)) as compared to *S. iniae* (Fig. 3.25 (b)). However, the ROS production for both types of RuO<sub>2</sub> containing bacterial cultures was found significantly lower than Ag nanoparticles. Previous studies on ZnO, TiO<sub>2</sub> and MgO nanomaterials showed the cellular toxicity owing to oxidative stress [51]. Several studies claimed that the direct contact itself is sufficient for bacterial cell death which is based on the surface charge of the nanoparticles. Both mechanisms are inter-related [52] and the exact mechanism of the toxicity of the RuO<sub>2</sub> nanoparticles need further investigations.



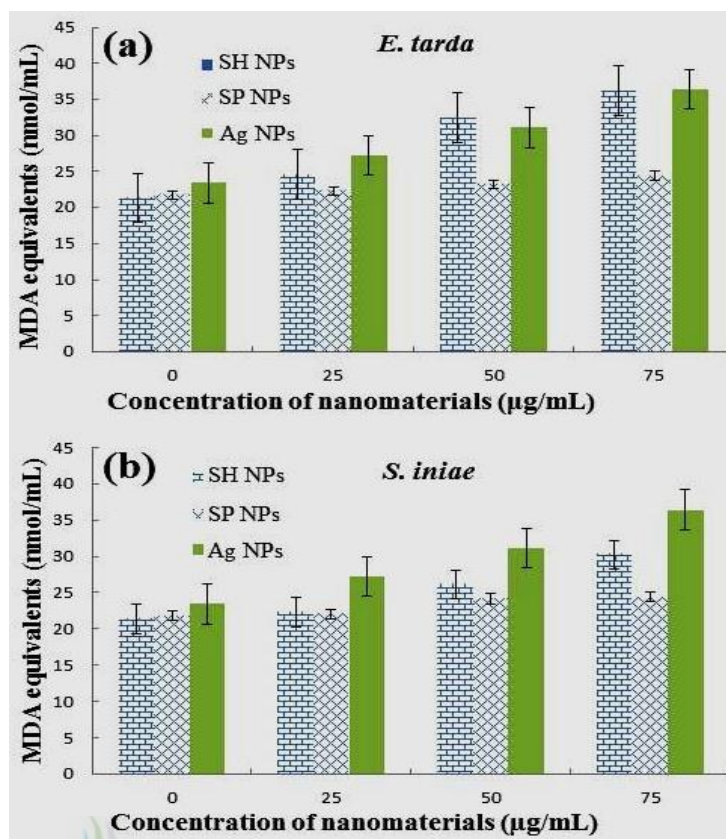


**Figure 3.25** Bar charts show the trends of MDA equivalents with increasing concentration of SP NPs, SH NPs and Silver nanoparticles.

To summarize, a systematic study on the wet chemical synthesis, characterization and shape dependent anti-bacterial studies of  $RuO_2$  nanomaterials were carried out. The concentration of the precursors, PEG surfactant and the reaction temperature played a major role in controlling the morphology. The surface chemistry of the materials was identified with FTIR and XPS which revealed the presence of majority of ruthenium oxides without much variation in its oxidation state as compared to samples prepared by plasma techniques. The prepared nanomaterials showed an excellent stability in water and tend to adsorb easily on bacterial surfaces due to its surface charge. Investigations of the antibacterial property on fish pathogenic bacteria showed that sheet-like  $RuO_2$  nanomaterials render strong inhibition as compared to spherical type nanostructured materials.

### 3.4 Shape dependent CO oxidation performance of RuO<sub>x</sub>/γ-Al<sub>2</sub>O<sub>3</sub>

#### 3.4.1 Characterization of the catalyst

Figure 3.26 (a-b) shows the FESEM micrographs of the RAWOS and RAWS catalysts, respectively. The RAWOS samples showed the presence of aggregated structures of RuO<sub>x</sub> nanomaterials inside and on the surface of the γ-Al<sub>2</sub>O<sub>3</sub> support. By contrast, the PEG-stabilized RAWS sample exhibited a finger-like protrusion of RuO<sub>x</sub> on the surface of the γ-Al<sub>2</sub>O<sub>3</sub>.

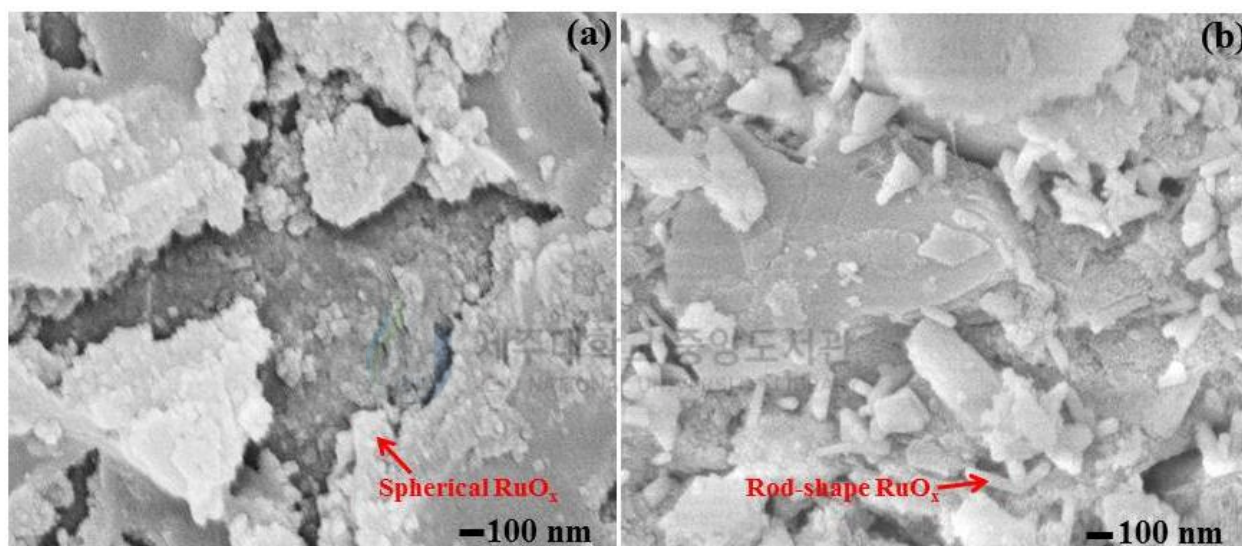


**Figure 3.26** The FESEM surface morphological images of RAWOS (a) and RAWS (b) catalysts.

(Abbreviations: RAWOS: RuO<sub>x</sub>/γ-Al<sub>2</sub>O<sub>3</sub> without polymer stabilizer; RAWS: polymer stabilized RuO<sub>x</sub>/γ-Al<sub>2</sub>O<sub>3</sub>).

The TEM image of RAWOS sample (Fig. 3.27 a) clearly displayed the distinction between γ-Al<sub>2</sub>O<sub>3</sub> (gray) and small size RuO<sub>x</sub> (black) which is non-uniform in shape and size. At the same time, RAWS clearly show the presence of rod-like structures with a length and width of *ca.* 200 and 75 nm, respectively (Fig. 3.27 (b)). Assemblies of nanorods such as this were widespread throughout catalyst samples. The elemental composition measured by EDX data for

the corresponding catalysts can be seen in the right side of the figures. The RAWOS catalyst contains 58.34% oxygen and 9.78% Ru whereas RAWS contain 46.49 % oxygen and 50.94 % Ru (atomic percentage).

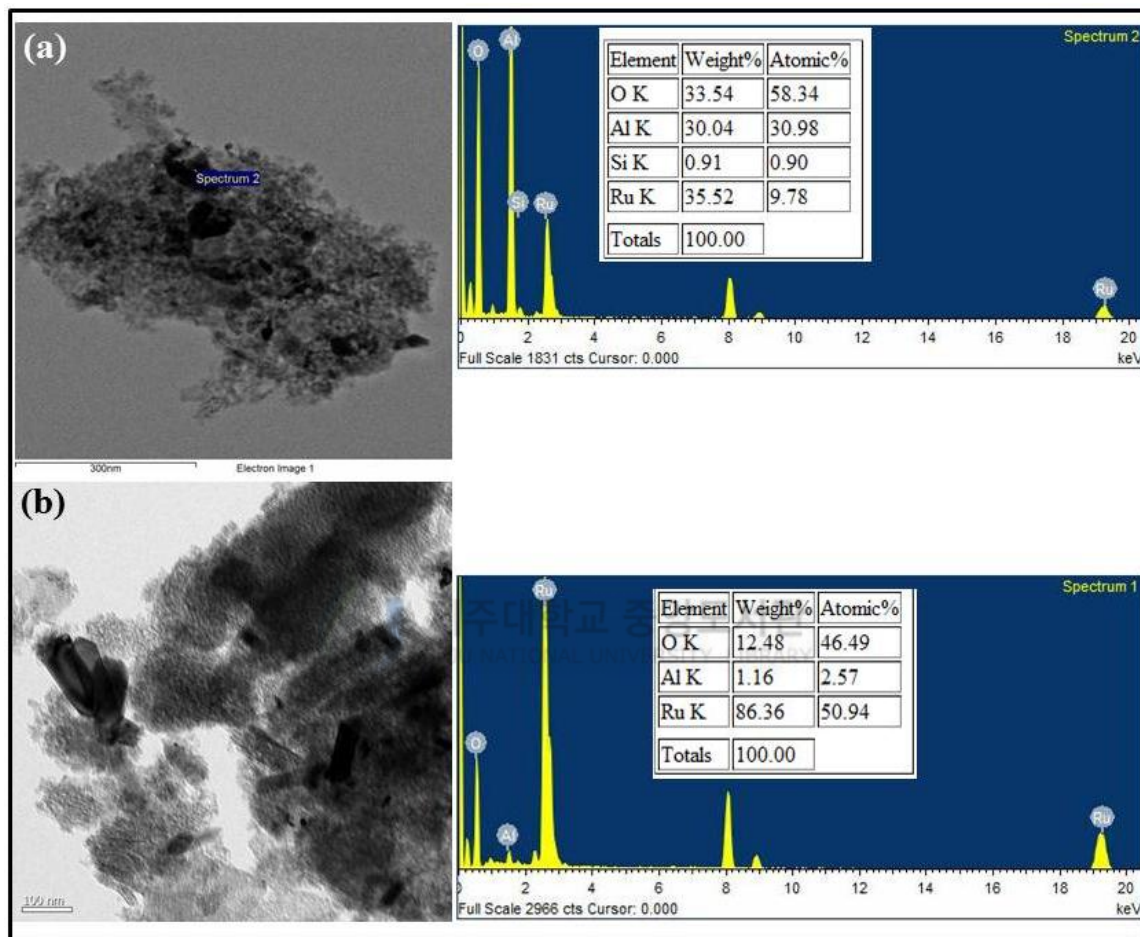


**Figure 3.27** The TEM images of RAWOS (a) and RAWS (b) catalysts along with the EDX spectra. The composition of the catalyst elements are given inside.

The observed one dimensional (1D) growth found in RAWS is proposed to originate from the formation of micelles in PEG solution, which further directs the growth of the catalyst. As noted previously in the literature, the formation of 1D structure is achieved due to the effect of PEG acting as a capping and growth directing agent. The ordered chain structure of PEG

(mainly arising from oxygen in the C-O-C chains) is anticipated to adsorb easily on a ruthenium-rich surface, coordinating with the ruthenium ions forming PEG-Ru<sup>+3</sup> complexes in the colloidal state and confining growth at specific crystal faces [53,54] . Subsequent neutralization with alkaline solution (ammonia) produces PEG-Ru(OH)<sub>3</sub>. Finally heat treatment at high temperature (650 °C) removes PEG and water which results in the ruthenium oxide nanomaterials. This process is shown schematically in Fig. 3.28.

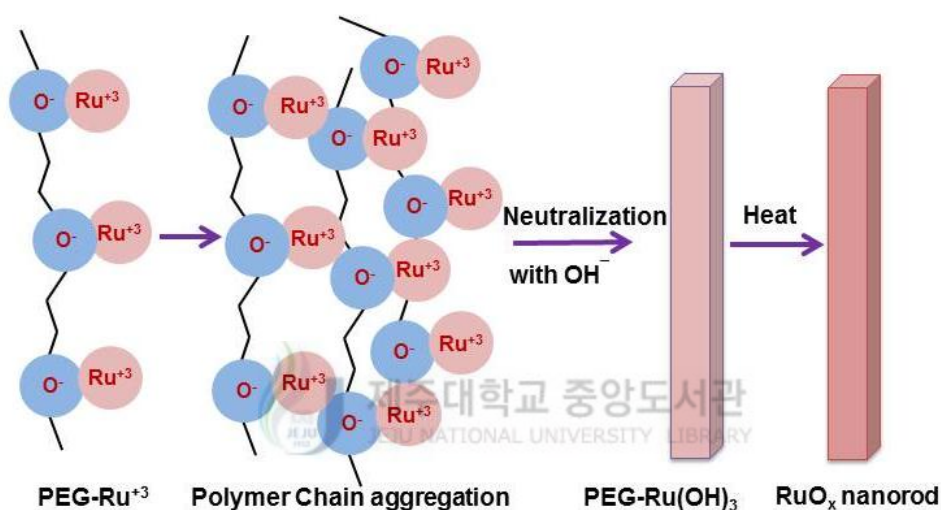


**Figure 3.28** Formation mechanism of 1-D RuO<sub>x</sub> in the presence of PEG.

The phase and crystal structure of the ALVIR, RAWOS and RAWOS catalysts were analyzed by using XRD and given in Fig. 3.29. The diffraction pattern of the as-received alumina shows prominent diffraction peaks at  $2\theta=36.7, 45.8$  and  $66.9^\circ$  corresponding to the (311), (400) and (440) reflections of  $\gamma$ -Al<sub>2</sub>O<sub>3</sub>, respectively (*cf.* JCPDS card no. 00-010-0425). Commonly, commercial  $\gamma$ -Al<sub>2</sub>O<sub>3</sub> is mesoporous with a higher surface area and the most thermodynamically stable phase of alumina [55-57]. The XRD diffractograms of both the synthesized and heat-treated catalyst materials displayed identical peaks although reflections

corresponding to  $\text{RuO}_x$  could not be observed clearly which may due to the inclusion of Ru atoms in the interstitial sites of alumina or it may simply due to the lesser amount of  $\text{RuO}_x$  [58].

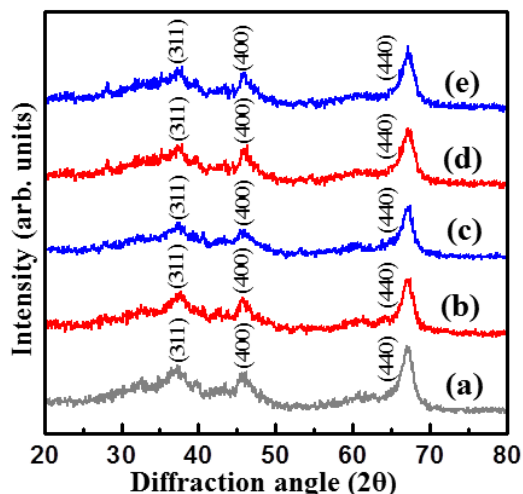


**Figure 3.29** The XRD spectra of the catalysts: The as prepared ALVIR (a), RAWOS (b) and RAWS (c). The RAWOS and RAWS catalysts heat-treated at 650°C are given in (d) and (e), respectively.

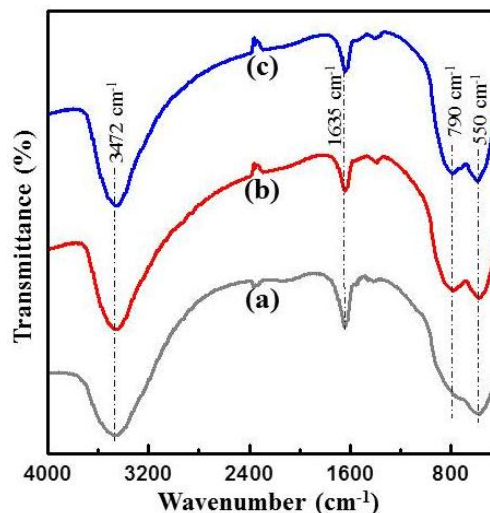


**Figure 3.30** The FTIR spectra recorded for ALVIR, RAWOS and RAWS catalysts (a-c).

The FTIR spectra of the ALVIR, RAWOS and RAWS catalysts are shown in Fig. 3.30 (a-c), respectively. As-received alumina exhibited prominent bands at 550  $\text{cm}^{-1}$  and 790  $\text{cm}^{-1}$  corresponding to the Al ions in octahedral and tetrahedral surrounding (Al-O vibrations), respectively [59]. The band at 1635  $\text{cm}^{-1}$  can be associated with physisorbed water (from exposure prior to analysis) and a broad peak between 3200  $\text{cm}^{-1}$  and 3600  $\text{cm}^{-1}$  indicate OH stretching exhibited by hydroxyl functional groups [60,61]. The FTIR spectra of the RAWOS and RAWS catalysts displayed similar peaks to those observed in spectra for ALVIR. Ru-O vibrations are expected to occur between 600 and 800  $\text{cm}^{-1}$  and thus a distinction between Al-O

and Ru-O bands could not be clearly made. Bands originating from the functional groups associated with PEG (the main C-O-C band at  $1094\text{ cm}^{-1}$ ) in the RAWOS sample were not observed, which implies that the PEG was removed by the heat treatment.

The RAWOS and RAWOS catalysts were additionally characterized using XPS (Fig. 3.31). Spectra were de-convoluted using a Gauss-Laurentzian peak fitting program. The respective high resolution core level Al 2p, Ru 3d and Ru 3p spectra are given for the catalyst RAWOS (Fig. 3.31 a-c) and RAWOS (Fig. 3.31 d-f). The binding energy values observed in the Al 2p spectra of both catalysts correspond to  $\text{Al}_2\text{O}_3$  as expected [62]. Spectra also consisted peaks corresponding to carbon (284.5 eV) and Ru 3d peaks typical for ruthenium oxides (286.2 and 286.0 eV) [63]. Since the Ru 3d and C 1s peaks are very close in terms of binding energy values, spectra in the Ru 3p region were recorded to clarify the ruthenium oxidation state and bonding environment. From the positions and relative intensity of the observed peaks, the RAWOS sample surface consisted of approximately 68 at.% Ru (IV) (typical of  $\text{RuO}_2$  - 462.4 eV) and approximately 32 at.%  $\text{RuO}_3$  (465.0 eV) [64]. By comparison, Ru 3p peaks for the RAWOS sample surface reflected an approximate composition of 62 at.% higher oxides of Ru (i.e.  $\text{RuO}_x$ , where  $x = 3$  mostly) at 464.3 eV and 38 at.% elemental  $\text{Ru}^0$ , (461.8 eV) [63]. It is reported that  $\text{RuO}_3$  was found in all of the surfaces of  $\text{RuO}_2$  and it plays main role in the stability of  $\text{RuO}_2$  [63]. It is clearly seen that when the sample was prepared with a polymer stabilizer such as PEG (RAWOS), it results in the formation of metallic Ru by the reducing activity of ethylene glycol molecules [65].

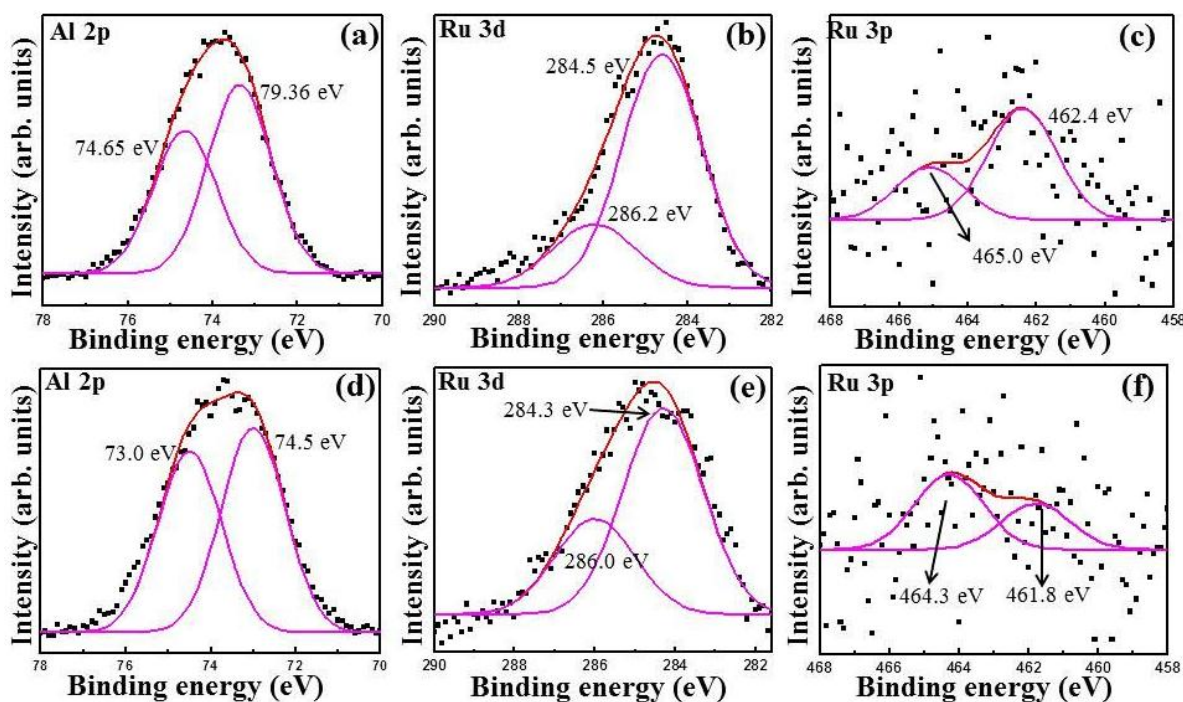


**Figure 3.31** High resolution core level Al 2p, Ru 3d and Ru 3p spectra corresponding to RAWOS (a-c) and RAWS (d-f) catalysts.

The adsorption capacity of gas molecules within the pores of the catalyst is an important step towards understanding the catalyst reaction. This can be determined from the surface and pore-characteristics of the catalyst. The pore volume and pore radius of the catalysts during adsorption and desorption process are listed in Table 7, which confirmed the standard values of the pore size (1.5-100 nm) reported [66]. The linearity of the data (indicating a strong interaction of the ruthenium oxide catalyst with  $N_2$ ) in the relative pressure ( $P/P_0$ ) range of 0.0-0.3 reinforces the suitability of applying the BET model in determining the specific surface area of the catalysts. The ALVIR, RAWOS and RAWS catalysts exhibit BET surface area values of *ca.* 112.2, 138.3 and 128.1  $m^2 g^{-1}$ , respectively. From a comparison of the RAWS and RAWOS sorption isotherm results, the addition of the polymer stabilizer apparently leads to an increase in the pore volume

and pore radius and a decrease in the surface area values ( $10.2 \text{ m}^2 \text{ g}^{-1}$ ). A similar trend has been reported previously when Ni-Al<sub>2</sub>O<sub>3</sub> catalyst was stabilized by cetyltrimethylammonium bromide.

**Table 7** Physisorption results of the catalysts measured by using Barrett-Joyner-Halenda (BJH) method.

Catalyst name	Process	Surface area (m <sup>2</sup> /g)	Pore volume (cc/g)	Pore radius (Mode Dv(r)) Å
ALVIR	Adsorption	102.9	0.2322	30.72
	Desorption	140.7	0.2480	28.18
RAWOS	Adsorption	120.5	0.2475	30.58
	Desorption	168.7	0.2694	24.40
RAWS	Adsorption	119.0	0.2532	30.76
	Desorption	164.8	0.2723	24.54

### 3.4.2 CO oxidation performance of the catalysts

Oxygen concentration and temperature were varied in the range of 0.5-2.5 vol. % and 50-250 °C, respectively in a series of CO oxidation experiments. The inlet concentration of CO was fixed at 2000 ppm. The conversion of CO into CO<sub>2</sub> obtained with the as received  $\gamma$ -Al<sub>2</sub>O<sub>3</sub> (ALVIR) under steady state conditions showed a maximum of 5.6 % at reactor temperature of 175°C. The CO conversion percentage using the RAWOS and RAWS catalyst material is shown in Fig. 3.32 (a-c) at the inlet concentration of oxygen from 0.5-2.5 vol.%, respectively. The plots clearly demonstrate a gradual increase in CO conversion from < 10 % at 50 °C to 100 % at 200 °C. Generally, varying the oxygen content at low temperature did not affect the overall

conversion process significantly but its influence at high temperature is clear. The RAWOS catalyst exhibits substantial activity above 100 °C. Similar behavior was observed on repeating the oxidation experiments with the PEG-stabilized RAWOS catalyst but the CO conversion percentage at each experimental temperature was notably higher. Moreover, total conversion was achieved at 175 °C as compared to 200 °C observed for the equivalent RAWOS catalyst. At low temperature (50 °C and 75 °C), the difference between the materials is almost negligible but when the temperature is increased, a remarkable difference can be noted. An increase in the CO conversion efficiency of about 33 % by RAWOS catalyst was observed in experiments at 125 °C with an O<sub>2</sub> concentration of 1.5%. Above and below this temperature, a gradual decrease in the conversion efficiency can be noted with a slight variation depending on the oxygen concentration. The stability of the catalysts was also confirmed by conducting the experiments continuously for 7 h at 125 °C. These extended experiments showed the repeatability of the performance observed above without any significant change.

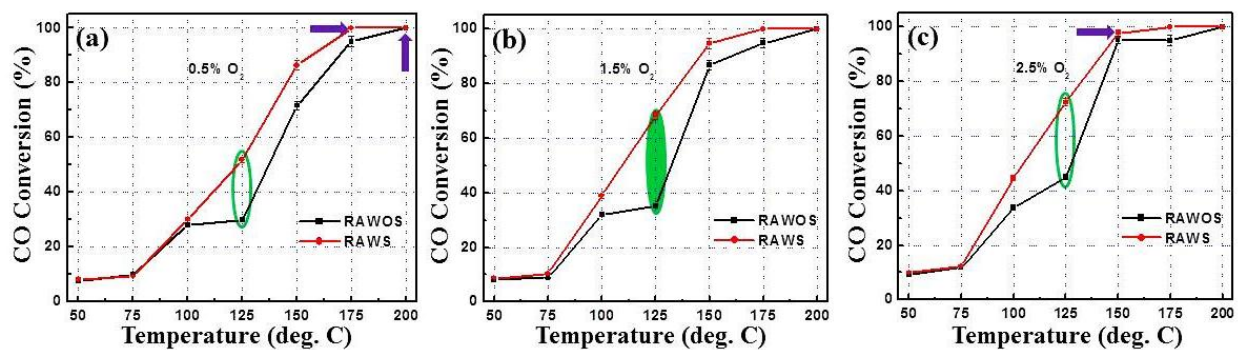


**Figure 3.32** The CO oxidation performance of RAWOS and RAWS catalysts with different concentrations of oxygen.

In order to investigate the performance of the catalysts under real working conditions, water was added to the reactant gas (i.e. CO + H<sub>2</sub>O + O<sub>2</sub>). The experiments were thus performed

in the presence of 2.5 % and 5 % water (by volume) at different temperature. The results of these CO oxidation experiments are represented in Figs. 3.33 (a-b), respectively. The CO conversion efficiency increased depending upon the temperature. For a water content of 2.5 %, full conversion was achieved at 275 °C for the RAWOS catalyst. By contrast, the rod type RAWOS catalysts exhibited 100 % CO oxidation at a reduced temperature of 225 °C (Fig. 3.33 – (a)). Increasing the water content from 2.5 to 5 % resulted in the shift of temperature to 300 °C for the RAWOS material and 250 °C for the RAWOS catalyst, respectively (Fig. 3.33-(b)). In addition, it is very clear that at every reaction temperature, the RAWOS catalyst showed an improved conversion performance over the RAWOS equivalent. As compared to the results obtained under dry conditions, increase in the effective temperature required for full conversion can be understood in terms of the competition between CO and H<sub>2</sub>O adsorption in the reactive sites of the catalysts. This also consistent with the finding that pre-oxidized RuO<sub>x</sub> catalysts are very active in dry conditions, similar to the phenomena exhibited by oxides of copper and cobalt [67,68].

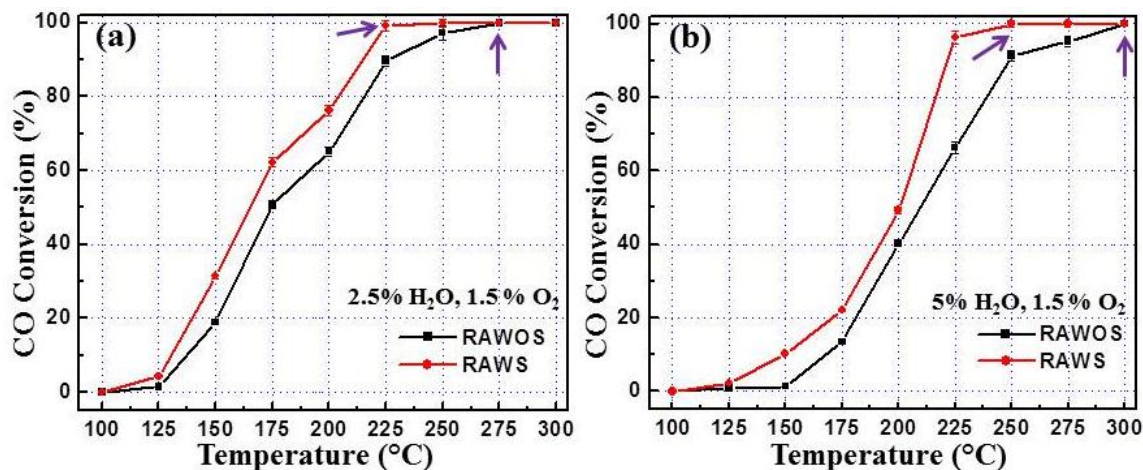


**Figure 3.33** Effect of (a) 2.5 vol. % and (b) 5 vol. % water content on the CO oxidation using RAWOS and RAW catalyst. The inlet oxygen concentration was fixed at 1.5 vol. % .

Second set of experiments were carried out to examine the effect when decreasing the amount of catalyst loading to 0.5 wt.%, results of which are given in Fig. 3.34. The CO oxidation performance exhibited by RAWOS (a), RAWS (b) and the difference between the two (c) is represented. Since the amount of catalyst loading is reduced to half, the total conversion was observed only at 250°C for both catalysts. The conversion at each temperature was less than the conversion percentage observed when using 1wt.% catalyst loading. On comparison, RAWS catalyst exhibited higher conversion efficiency than RAWOS. The overall supremacy of RAWS was noted as 6.1% at 175°C, below this temperature the efficiency difference was gradually decreased (Fig. 3.34 (c)).

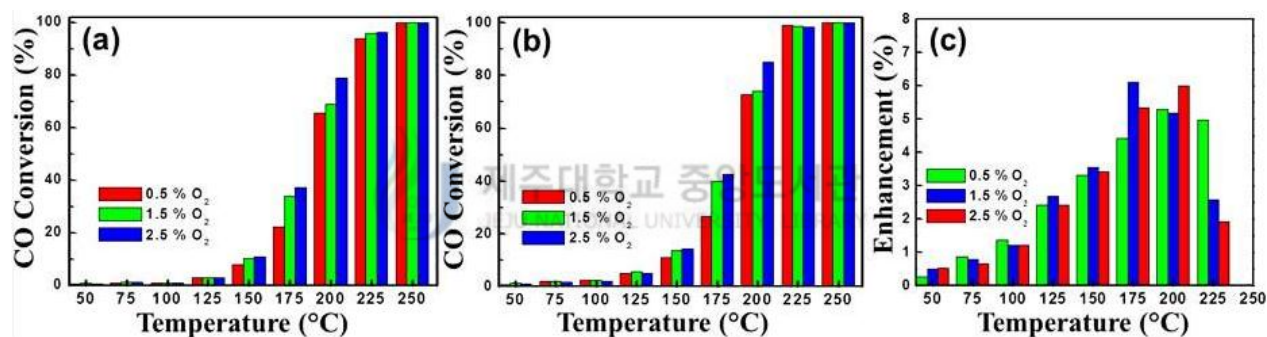


**Figure 3.34** The CO conversion performance corresponding to (a) RAWOS, (b) RAWS and (c) activity difference between RAWOS and RAWS. The experiment was performed at 0.5 wt.% catalyst loading.

### 3.4.3 Discussions

The reason for the enhancement of the catalytic activity in the PEG-stabilized materials results from a combination of factors. First, the increase in the pore volume and pore size would appear to be dominant (Table 7). Second, the stoichiometric and non-stoichiometric ruthenium oxides (and hence variable ruthenium oxidation states) states might be expected to contribute to

the catalyst activity is seen, for example  $\text{MnO}_x$  (where  $x < 2$ ) [69]. Arguments in the literature suggest that metallic Ru as observed in the RAWS material (and as found by XPS), forms bonds with adsorbed ad-layers of oxygen (as a transient surface oxide) *in situ* during CO oxidation and catalytically more active below 500K [70-73]. Third, metallic catalyst on the oxide supports show structure-sensitive (size) catalytic activity and favors towards high CO adsorption when experiments were conducted with Pd and Rh. For example, Zhou *et al* have reported that increase in the CO oxidation capability of Pt nanowires over zero dimensional Pt nanostructures is due to the large crystal facets and a small density of defect sites [74]. This means that the synergistic effect rendered by metallic component combined with rod-structure of  $\text{RuO}_x$  (as a manifestation of shape dependent catalytic activity) also explain such improvements [75]. It is reported that the difference in the geometry of nanomaterials occur due to the changes in the surface atomic arrangement and thus exhibit different electronic structure [76]. The binding strength between the catalyst surface and the adsorbed species (interaction) depends on such atomic arrangements (defect structures) which in turn influence the catalytic activity and selectivity [77,78]. The open coordination sites rendered by the edge and corner atoms than terrace atoms [79] usually found in tetrahedral (in our case, Ru exhibit rutile type and the Ru atoms located in the corner) nanomaterials might significantly affect adsorption energy (activation energy) and bond enthalpy as observed in electron transfer reactions [80]. In addition, the flat sides of  $\text{RuO}_x$  containing large number of surface atoms would increase the contact area with the catalyst support which can facilitate effective charge transfer and the support itself may supply additional reactive sites for the adsorption of reactant molecules [81] which is an important contribution by shape.

Finally, the catalyst dispersion engendered in the PEG-stabilized catalysts contributes significantly to catalyst activity. Figure 3.35 shows the TPR profiles of the RAWOS and RAWS catalysts. The H<sub>2</sub> consumption profiles exhibits a number of maxima at different temperatures, implying the existence of various Ru species on  $\gamma$ -Al<sub>2</sub>O<sub>3</sub>. The H<sub>2</sub>-TPR for RAWOS shows reduction peaks between 100-300 °C. The narrow peaks at *ca.* 168 °C and 225 °C (and 266 °C) correspond to the reduction of RuO<sub>3</sub> and RuO<sub>2</sub> [82,83]. Low temperature peak found at 110 °C refers to the formation of ruthenium from tiny RuO<sub>2</sub> particles (Fig. 3.35 a). By comparison, the RAWS catalyst exhibited a smooth and well defined ruthenium reduction peak with large peak area at low temperature (95.5°C). High temperature peak at 522°C is the result of the reduction of the mesoporous  $\gamma$ -Al<sub>2</sub>O<sub>3</sub> support [84,85] and reasonably a high shoulder peak at 331°C should be the reduction of large RuO<sub>2</sub> nanorod structures. Comparing the peak areas, the amount of H<sub>2</sub> gas consumed by the RAWS catalyst is higher than the un-stabilized catalysts and the reduction events are shifted consistently shifted to lower temperature (by between 35-170°C). One might infer therefore that since the rod-structured catalyst is well-dispersed the formation of oxygen vacancies throughout the RuO<sub>x</sub> is facilitated *via* the facile interaction of gaseous species, which ultimately leads to an enhancement of CO oxidation. Such a size and shape dependent reduction behavior of supported RuO<sub>x</sub> observed now was previously encountered when using CeO<sub>2</sub> catalysts [84].

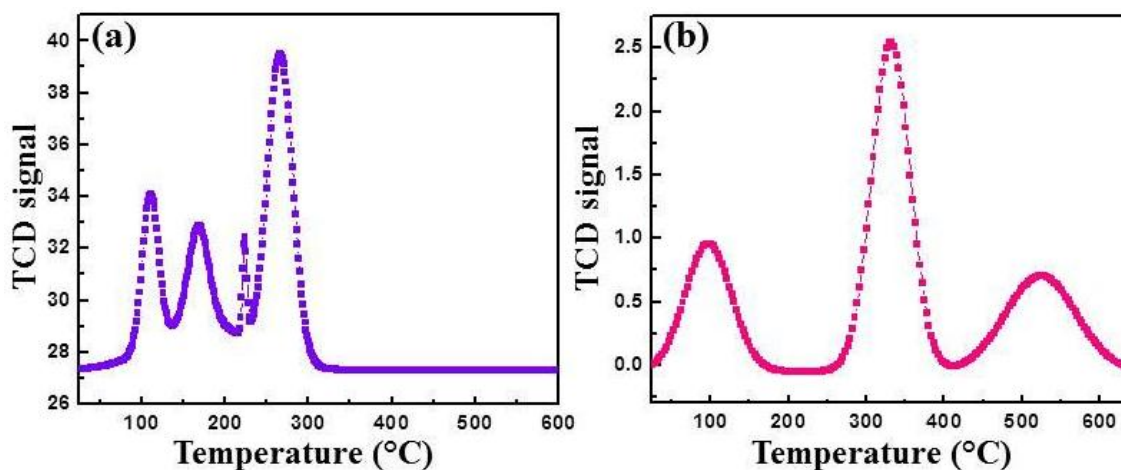


**Figure 3.35** The H<sub>2</sub> consumption (TPR) profiles of the RAWOS (a) and RAWS (b) catalysts.

*This study dealt with the preparation of nano-sized RuO<sub>x</sub> catalysts on mesoporous  $\gamma$ -Al<sub>2</sub>O<sub>3</sub> support by following a chemical co-precipitation route. Two predominant types of catalyst nanomaterial were synthesized; aggregated spheres and dispersed rods. The addition of PEG surfactant was essential in achieving the latter catalyst morphology. Subsequent characterization showed that polymeric surfactant used for stabilization could be removed by heat treatment and did not lead to catalyst poisoning. The surfactant played the principal roles in controlling morphology and pore characteristics of the catalysts. It was observed that the PEG-stabilized rod type nanomaterials showed superior conversion over un-stabilized spherical-shaped materials in the catalytic oxidation of CO. The use of PEG in mediating the shape, size, surface structure and transition metal oxidation state is crucial in tailoring the catalyst performance.*

### 3.5 The DBD Plasma-mediated synthesis of CuO nanomaterials

The FTIR and XRD spectra of the Ar plasma synthesized CuO nanomaterials are given in Figs. 3.36 (a)-(b), respectively. The copper oxide sample exhibited main bands at 530 and 607  $\text{cm}^{-1}$  which are attributed to  $\text{Cu}_2\text{O}$  and CuO stretching [86]. The metal-oxygen vibrations corresponding to Cu-O was observed at 445-910  $\text{cm}^{-1}$  [87]. Peaks around 1645  $\text{cm}^{-1}$  and beyond 3400  $\text{cm}^{-1}$  in all samples refer to the O-H stretching of adventitious water molecules. The diffraction patterns observed for copper oxide consisted mainly of CuO and a small diffraction peak at  $48.7^\circ$  corresponds to metallic copper [88]. The XRD peaks shown by rutile type  $\text{RuO}_2$  contain major peaks around  $28^\circ$ ,  $35^\circ$ ,  $54^\circ$  corresponding to (110), (101) and (211) sets of lattice planes of vibration. Moreover, (101) plane intensity is higher than any other peaks, which showed the growth of one dimensional structures such as nanorods.

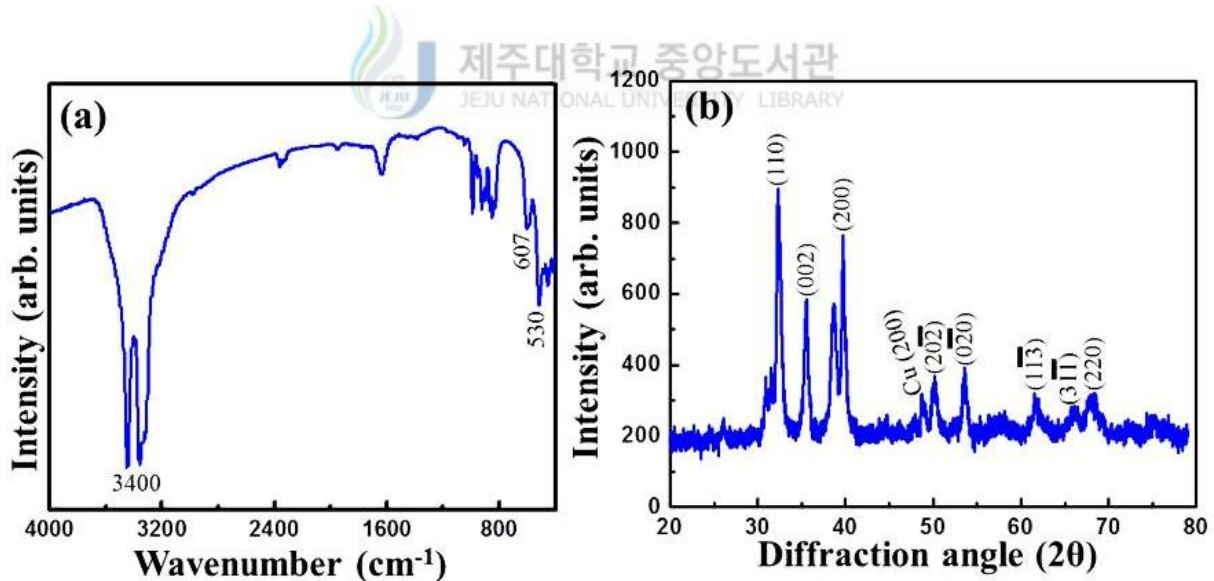


**Figure 3.36** The FTIR (a) and XRD (b) spectra of the Ar plasma synthesized CuO nanomaterials.

The FESEM morphological images of the plasma-synthesized CuO showed cylindrical shape with small dips on the surface (Fig. 3.37 a) whereas the CuO nanomaterials synthesized

using wet chemical technique and commercial samples exhibited aggregated spherical features (Fig 3.37 c-d), respectively. It can be easily seen from the images that the plasma mediated process influenced the morphology, which is very different from the materials prepared from conventional synthesis. Basically, in wet chemical routes, aggregation is a major problem which can be prevented by using stabilizing polymers or surfactants. Since there was no capping agent used for the synthesis, only spherical nanomaterials with varying particle size were observed.

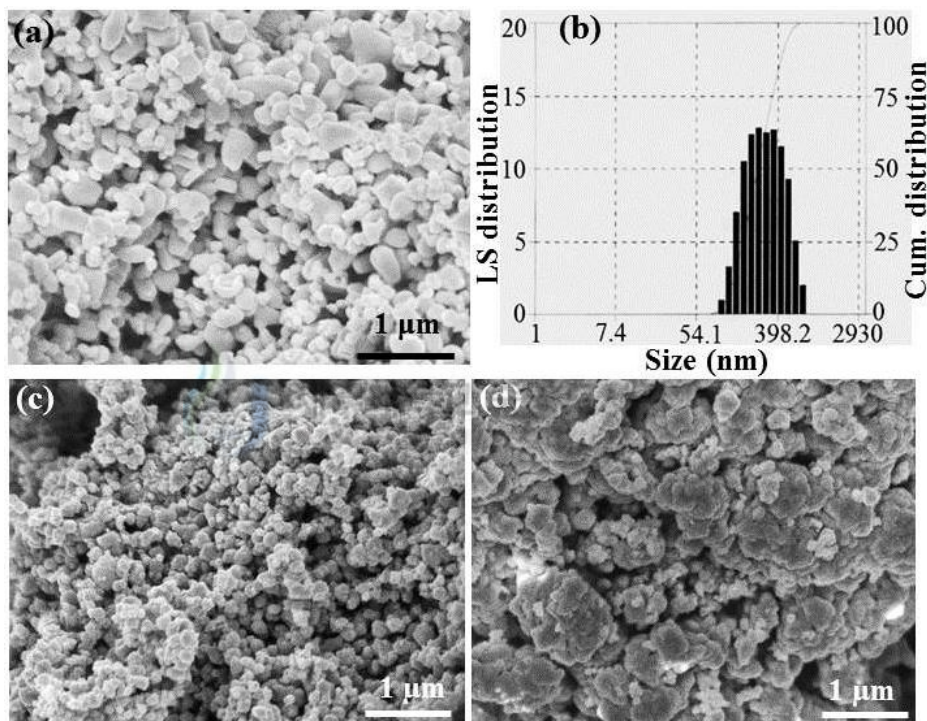


**Figure 3.37** The FESEM images of the Ar plasma synthesized (a), wet chemically synthesized (c) and commercial (d) CuO samples. And (b) shows the particle size distribution of the plasma-mediated CuO NMs.

Particle size analysis was performed for CuO nanomaterials, and the average hydrodynamic diameter was 225 nm. The particle size distribution is also shown in Fig. 3.37 (b) where the size of the nanomaterials versus light scattering distribution (%) along with cumulative percentage is

represented. Further, the nanomaterials might be hydrated in water, which could explain the distribution in higher size range. The average size of the CuO obtained from the particle size analysis confirmed the morphological features obtained by FESEM.

It is important to note that the morphological structures observed for CuO nanomaterials prepared in the presence of plasma was entirely different. It may be due to the plasma characteristics and its specific interaction with each material. The CuO is a p-type semiconductor with a band gap of approximately 1.5 eV [89], leading to the accumulation of electrons which can move easily to the entire surface of the growing particles. When the negative potential increases in a specific region, the growth is driven towards positive potential created by the high voltage electrode, and vice versa. Since the electrons are highly mobile, a perfect nanorod or nanosheet structure could not be obtained (Fig. 3.38). In this case, heat loss is only due to the material's resistance ( $i^2R$  is very less), which is immediately dissipated to the reactor atmosphere and it did not help for material's growth very much. The dips on the surface of CuO observed might be due to spouting-out of water vapors when the heat treatment was carried out. (For reader's information, the CuO nanofibers were grown by using DBD plasma by taking dry  $\text{Cu}(\text{OH})_2$  powder and the mechanism was not explained in detail in the literature [90]).

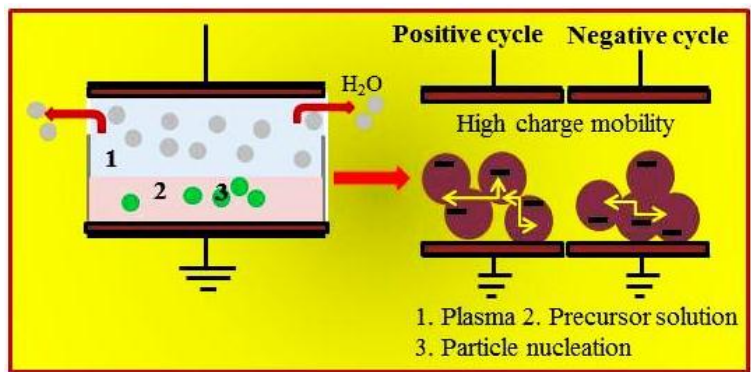


**Figure 3.38** Growth mechanism of CuO in the presence of Ar plasma.

### 3.6 Shape dependent antibacterial performance of CuO NMs

#### 3.6.1. X-Ray diffraction study for structural analysis

The XRD patterns obtained for CuO 75, CuO 100 and HYD 150 samples are given in Fig. 3.39 (a-c), respectively along with standard peaks for Cu<sub>2</sub>O and Cu(OH)<sub>2</sub>. Prominent peaks at the diffraction angle ( $2\theta$ ) 35.4, 38.5 and 48.8° refer to (0,0,2), (2,0,0) and (2,0,-2) lattice planes of vibration of monoclinic CuO NMs (JCPDS file No.48-1548) [91]. The space group of the material is reported to be C2/c (the lattice parameters are:  $a_0=4.688 \text{ \AA}$ ,  $b_0=3.423 \text{ \AA}$ ,  $c_0=5.132 \text{ \AA}$ ,  $\alpha=\gamma=90^\circ$  and  $\beta=99.54^\circ$ ) [92]. Other small diffraction peaks are noted with its respective miller indices in the figure. All samples exhibited a similar diffraction pattern but the intensity of the peaks at 35.4 and 38.5° increased for CuO 100 and HYD 150 (b and c) as compared to CuO 75 (a). It might result from the changes in the nucleation and growth pattern of CuO NMs in which growth favors towards a particular plane. In addition, high purity of the prepared sample was confirmed by the absence of peaks pertaining to impurities.

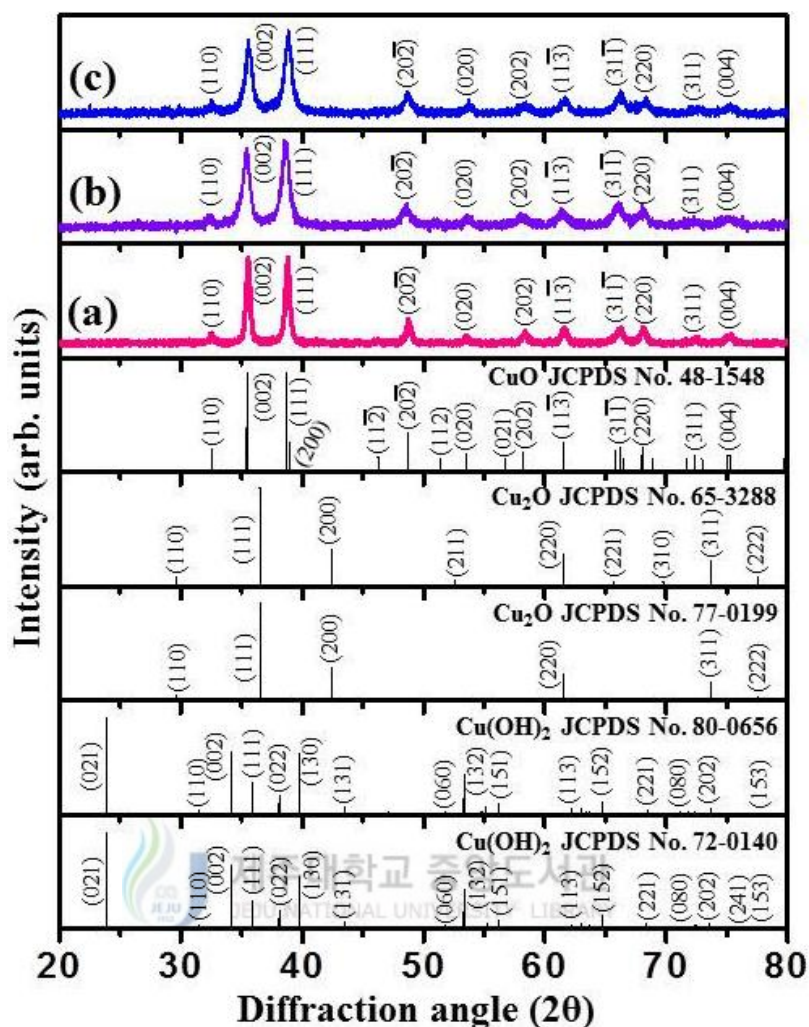


**Figure 3.39** The XRD patterns of copper oxide nanomaterials. (a) CuO 75, (b) CuO 100, and (c) HYD 150. The standard JCPDS data correspond to CuO, Cu<sub>2</sub>O and Cu(OH)<sub>2</sub> are also given.

### 3.6.2. Surface morphological analysis

The FESEM surface morphological images of the samples CuO 75, CuO 100 and HYD 150 are represented in Figs. 3.40 (a-c), respectively when no PEG surfactant was used. The CuO 75 sample exhibited aggregated spherical nanoparticles with diameter <50 nm. It is due to the fact that the nanoparticles tend to aggregate in order to reduce the Gibb's free energy in the absence of any surfactant. It seems that aggregated structures are commonly observed in most of the

methods including microwave irradiation [93]. The CuO 100 exhibited slightly elongated structures with less aggregates as compared to CuO 75. But the HYD 100 exhibited nanoplates of approximately 100 nm length in all sides. It is obvious to note that the preparation method influenced the morphology of the nanomaterials, especially the temperature and pressure parameters played vital roles. It means spherical nanoparticles could be obtained by conventional wet chemical approach but the temperature control is important [94]. On the other hand, hydrothermal method results in the formation of two dimensional structures such as nanoplates/sheets [95,96]. The FESEM images of the CuO 75, CuO 100 and HYD 150 samples prepared with the addition of PEG are represented in Figs. 3.40 (d-f), respectively. The CuO 75 exhibited rice grain-like morphology, similar to which is reported in the literature (spindly nanocrystals of CuO was prepared by using complex, wire explosion system) [97]. In this case, PEG acted as a templating or structure directing agent and also helped to reduce the surface free energy [98,99]. The CuO 100 exhibited a nanoneedle-like structures with length  $> 300$  nm and width of about 50 nm. In this case, temperature and reaction condition played major roles in which the growth is thermodynamically controlled. At the same time, the sample prepared in the hydrothermal condition exhibited a uniform nanoplate structure with each sides ranging  $> 200$  nm with thickness  $< 30$  nm. It is reported in the literature that hydrothermal synthesis of CuO NMs are governed both by growth thermodynamics and the growth kinetics which usually render flower-like structures [100]. When comparing HYD 150 prepared without surfactant, addition of PEG enhanced the size of the nanoplates. Such enhancement in the shape and size control was not observed in other samples.

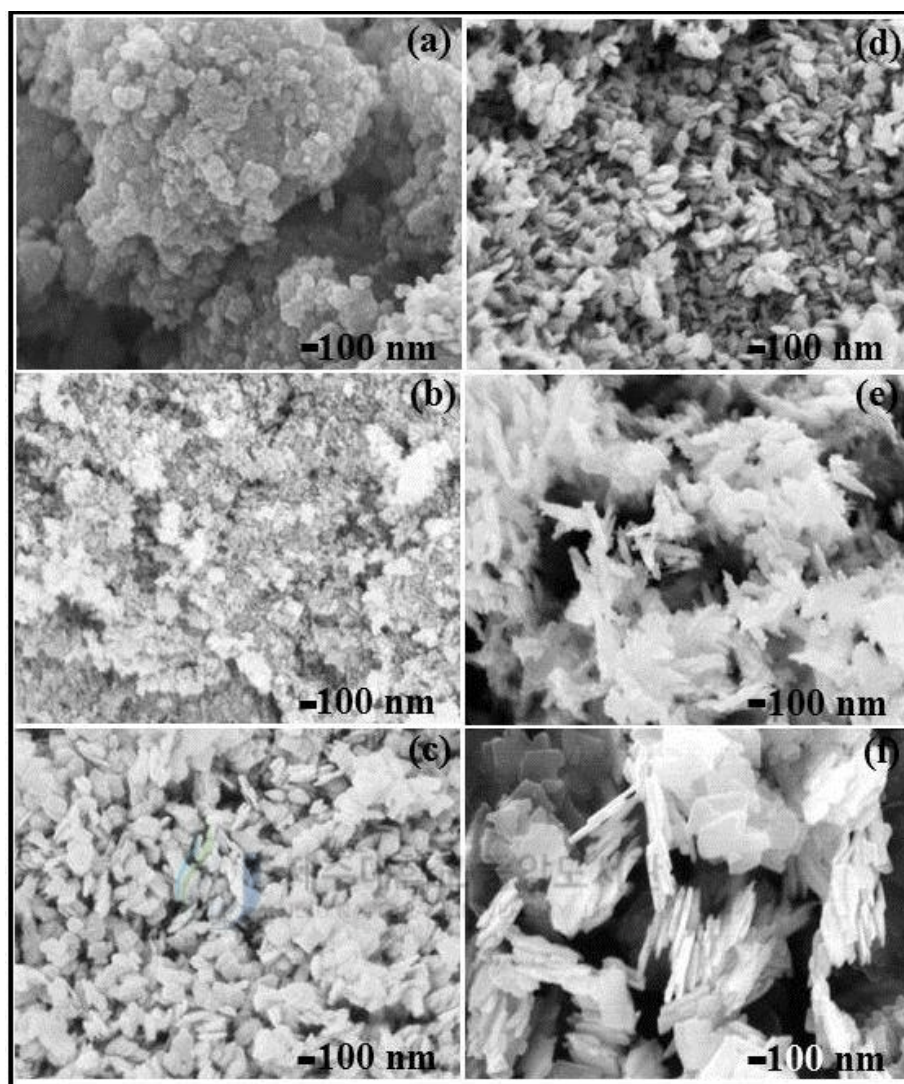


**Figure 3.40** The FESEM images of the CuO 75, CuO 100 and HYD 150 samples prepared in the absence (a-c) and in the presence (d-f) of PEG surfactant, respectively.

For further information about the influence of PEG surfactant on the CuO NMs morphology the FESEM images are given in Fig. 3.41. In this case, 0.0001M (a-c) and 0.0003 M (d-f) concentration of PEG solutions were used and other experimental parameters were maintained identical. It was noticed that, particle size, shape and aggregation were greatly influenced by PEG concentration. For example, when 0.0001M PEG was used at 75 °C, the grain-like morphology was not clearly observed which looked like a spherical particles (Fig. 3.41 a).

Increasing PEG concentration to 0.0003 M increased the size and resulted in aggregated clusters of grain-like CuO NMs (Fig. 3.41 d). Similar phenomena was noted when the experiment was carried out at 100 °C, in which the needle-like particles were aggregated and formed a flower-like morphology (Fig. 3.41 e). In hydrothermal conditions, changing the concentration of PEG did not alter the shape of the CuO NMs to great extent but the size and thickness of the nanosheets were affected much (Figs. 3.41 c and f).

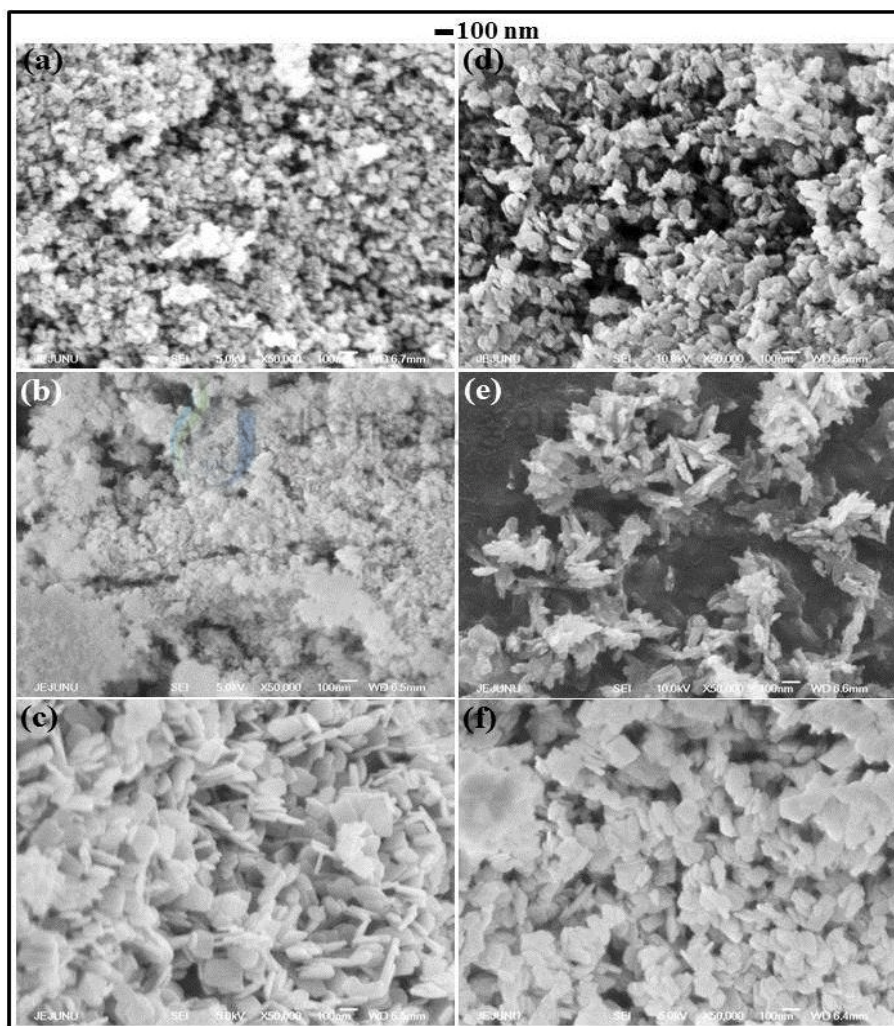


**Fig. 3.41** Effect of PEG addition on the morphology of CuO NMs: CuO 75 (a and d), CuO 100 (b and e) and HYD 150 (c and f) when 0.0001 M and 0.0003 M PEG was used, respectively.

### 3.6.3. Particle size analysis and surface charge measurement

Particle size analysis was performed for CuO 75, CuO 100 and HYD 150 NMs, and the average hydrodynamic diameter was found to be 92, 216 and 193 nm, respectively. The particle size distribution is also shown in Figs. 3.42 a-c, in which the nanomaterials size against light scattering distribution (%) along with cumulative percentage distribution is represented. The particle size values obtained with this method is comparable to the size observed from FESEM. Generally, the nanomaterials might easily be hydrated in water and due to the formation of dielectric layer around the nanomaterial in the liquid media, the particle size observed in this method is slightly higher than the microscopic values obtained.

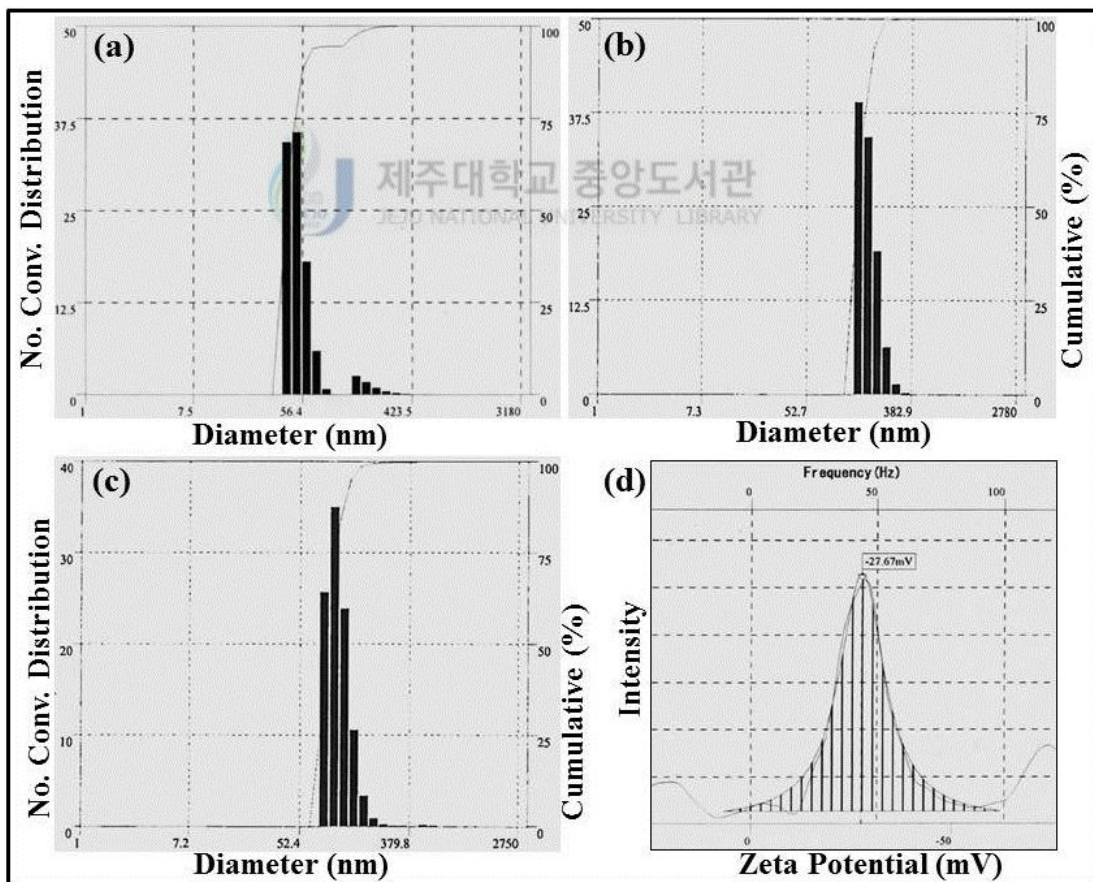


**Figure 3.42** Particle size distribution observed for CuO 75, CuO 100 and HYD 150 (a-c).

Typical zeta potential graph obtained for HYD 150 is given in (d).

The stability of CuO 75, CuO 100 and HYD 150 NMs was analyzed by measuring its surface charge (zeta potential) after dispersion in pure water at 25°C. In suspension state, repulsion between the adjacent particles by charging can be understood from the zeta potential. By definition, the zeta potential represent the potential difference between the dispersion medium and the stationary layer of liquid bound to the dispersed particle. It can be seen from a typical zeta potential graph corresponding to HYD 150 (Fig. 3.42 d), the surface charge value was -27.67 mV. The zeta potential of about -26.72, -25.5 mV was noted for CuO 75, CuO 100, respectively. There are six reasons for a material to acquire surface electrical charges are reported. For metal oxide such as copper oxide, ionization of surface groups (degree of charge development) and the presence of net molecular charge is commonly observed when the interface is deionized water. In addition, the zeta potential value is a function of pH of the dispersion medium. In our case, water was used (pH~7) and in this pH range, most of the nanoparticles including CuO exhibit negative zeta potential values [94]. Even though PEG was used as a non-ionic surfactant, (which played main role in the nanoparticle stabilization and morphology during synthesis) it was later removed by heat treatment. The absence of PEG bands in the FTIR spectra clearly showed this. So the negative value of the CuO nanoparticle should represent the actual surface charge. The zeta potential values exhibited by the particles are very close to the prescribed value of  $\pm 30$  mV for good stability.

#### **3.6.4. Functional group and surface chemical analysis**

The chemical functional group analysis for CuO 75, CuO 100 and HYD 150 nanomaterials were carried out by using FTIR spectrometer and the spectra are given in Fig. 3.43. The samples prepared by all methods exhibited similar chemical identity. A peak found at 520  $\text{cm}^{-1}$  is ascribed due to Cu-O stretching and others at 610 and 668  $\text{cm}^{-1}$  correspond to CuO

nanostructure [101]. A high intensity peak observed at  $3443\text{ cm}^{-1}$  refers to the vibration of O-H molecules. Vibration band at  $1050\text{ cm}^{-1}$  noticed for CuO 75 and CuO 100 corresponding to the coordination of metal (Cu) by O-H [102]. A shift of this peak towards higher wavenumber for needle-like CuO 100 to  $1123\text{ cm}^{-1}$  was noted. Literature suggests that shift in the FTIR spectra result from the changes in the strength of the hydrogen bond. If it is weak, then the intensity associated with absorption coefficient decrease and thus frequency of the band shift gradually [103]. Another reason might be from the mass effect. If the mass of the molecule (Cu-OH) reduces, then the peak shift towards higher wavenumber occurs (since the frequency of vibration is inversely proportional to the mass of the vibrating molecule).

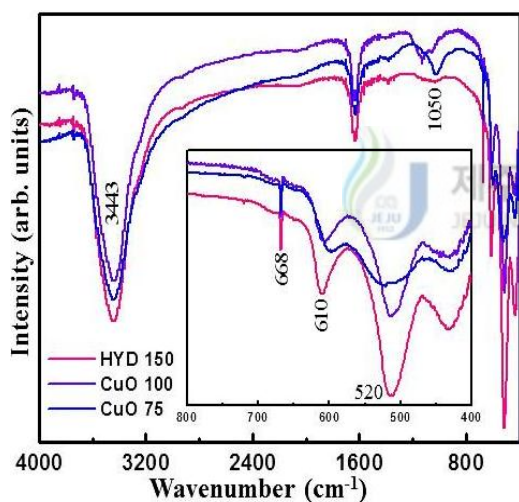


**Fig. 3.43** The FTIR spectra correspond to CuO 75, CuO 100 and HYD 150 nanomaterials.

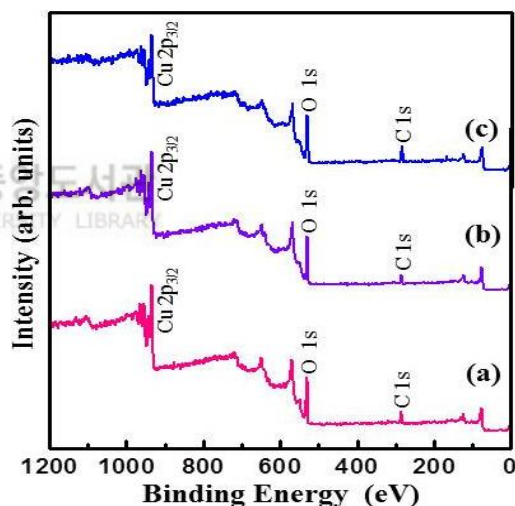


**Fig. 3.44** The XPS survey spectra of CuO 75, CuO 100 and HYD 150 (a-c).

The chemical state of surface of the prepared nanomaterials was also characterized by using XPS spectroscopy, the survey spectra of which are given in Fig. 3.44 (a-c). The presence of copper, oxygen and the adventitious carbon signal were noted down. The high resolution core-

level spectra of Cu  $2p_{3/2}$  and O 1s corresponding to CuO 75, CuO 100 and HYD 150 are given in Figs. 3.45 (a-c) and (d-f), respectively. The Cu 2p spectra of all the samples exhibited two peaks between the binding energy values 933.4-933.8 eV and 935.1-935.3 eV corresponding to CuO and Cu(OH)<sub>2</sub>, respectively [104,105]. The Oxygen spectra also consisted of two peaks around 530 and 532 eV refer to CuO (O<sup>2-</sup>) and adsorbed oxygen, respectively [106,107].

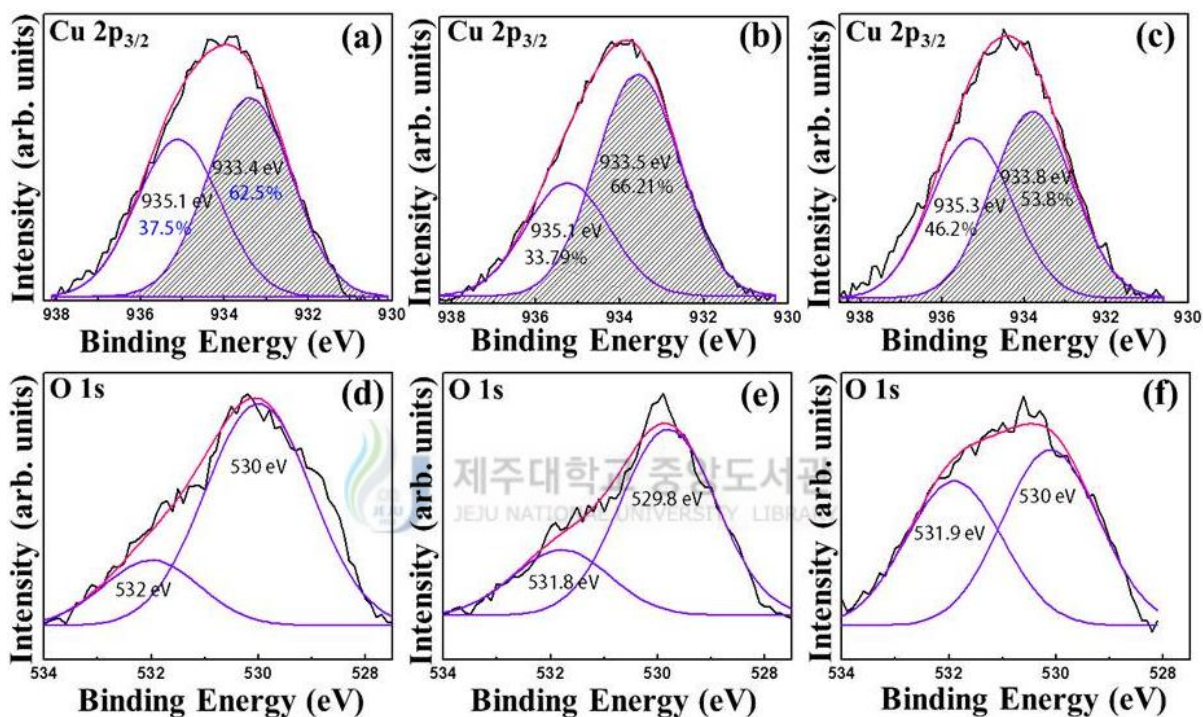


**Fig. 3.45** The high-resolution core level Cu  $2p_{3/2}$  (a-c) and O 1s (d-f) XPS spectra of CuO 75, CuO 100 and HYD 150 samples, respectively. The composition (at.%) of the species present in the sample is noted inside.

### 3.6.5. Results of antibacterial activity

Antibacterial activity of CuO NMs was analyzed against four bacterial strains namely *E. coli*, *S. iniae*, *S. parauberis* and *V. anguillarum*. Figure 3.46 represent the antibacterial activity of CuO NMs against *E. coli* and *S. iniae* using disc diffusion assay. In this method, among the

three samples, CuO 75 showed smaller zone formation against *E.coli* when compared with CuO 100. However, HYD 150 showed significant antibacterial activity with a comparable inhibitory zone formed by silver nanomaterials (+NMC). The diameter of inhibition zone reflects the magnitude of susceptibility of microbes. Antibacterial activity of CuO NMs against *S. iniae* and other bacterial strains are presented graphically in Fig. 3.47. It reveals that HYD 150 exhibits considerable antimicrobial activity against all bacteria particularly *S. iniae* was the most susceptible. Similar pattern was also noted for other two nanomaterials in which CuO 100 was found superior to CuO 75. In addition, the MIC values of three CuO nanomaterials against all the four pathogens are listed in table 8 (also see Fig. 3.48). Similar to disc diffusion assay, the HYD 150 sample showed the lowest MIC of 3.1250  $\mu\text{g/mL}$  for *E. coli* and 1.5625  $\mu\text{g/mL}$  for *S. iniae*, *S. parauberis* and *V. anguillarum* while the highest MIC (6.2500  $\mu\text{g/mL}$ ) was for CuO 100 against all pathogens except *S. iniae* (MIC 3.125  $\mu\text{g/mL}$ ). A drastic reduction in the value of MIC in this study was noted for *E.coli* due to the variation in the size and shape of the CuO NMs used as compared to other reports [108,51].

**Table 8.** The MIC values of the CuO NMs for the tested bacteria.

Bacteria	MIC values of the nanomaterials ( $\mu\text{g/mL}$ )			
	CuO 75	CuO 100	HYD 150	Ag NMs
<i>E. coli</i>	6.2500	6.2500	3.1250	1.5625
<i>S. iniae</i>	3.1250	3.1250	1.5625	1.5625
<i>S. parauberis</i>	3.1250	6.2500	1.5620	0.7813
<i>V. anguillarum</i>	1.5625	6.2500	1.5620	0.7813

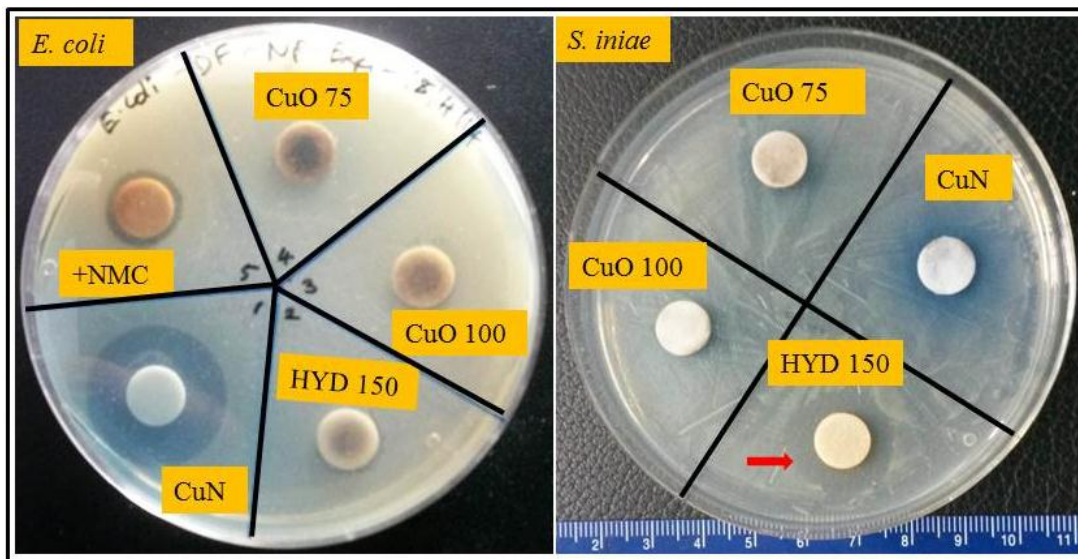


**Figure 3.46** Photographs show the disc diffusion (zone of inhibition) results of CuO NMs against (a) *E. coli* and (b) *S. iniae*. The +NMC refers to positive nanomaterial control (Ag NPs) and CuN refers to the CuO precursor (Copper (II) nitrate trihydrate). Higher zone formation was observed for the CuO precursor but it cannot be used directly as an antibacterial agent as it would harm the total aqueous media after dissolution.

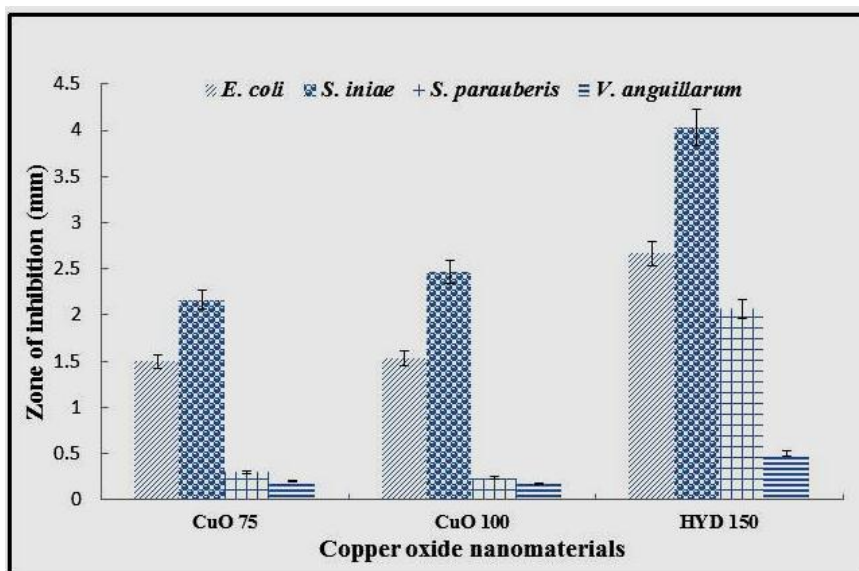


**Figure 3.47** The bar graph shows the value of the inhibition zone against different bacteria by using CuO 75, CuO 100 and HYD 150.

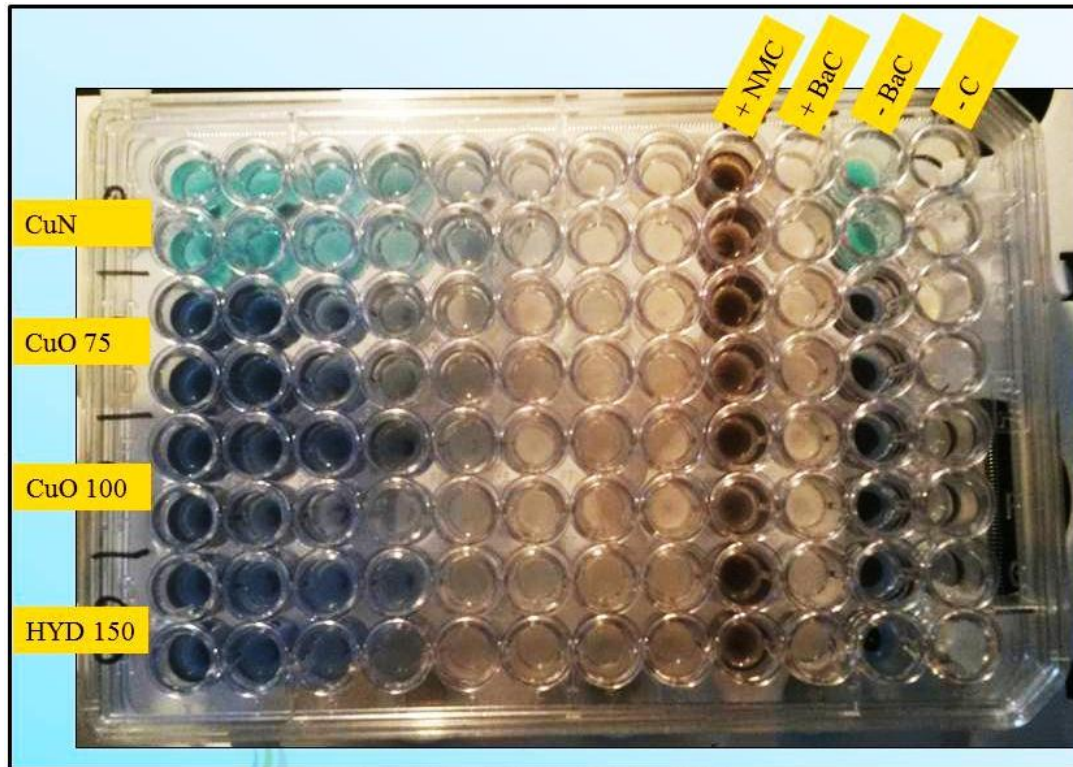


**Figure 3.48** Typical 96-well plate assay used to calculate the MIC values of *E. coli* for the prepared CuO NMs. The +NMC refers to positive nanomaterial control; +BaC refers to positive bacterial control; -BaC refers negative bacterial control and -C refers negative control.

The literature suggests the mechanism for the antibacterial activity of CuO NMs could result from several factors. A commonly observed ‘direct contact mechanism’ occurs between the different shape nanomaterials and the bacterial organelles in a shaker incubator. Grain-like, needle-like and plate-like CuO NMs might interact differently (process such as nanomaterial adsorption/desorption based on surface area, tearing of bacterial cell wall, cutting of the bacterial body by the nanomaterials, etc.) with the bacterial surface which could easily damage the cell [109]. In this case, the morphology of the CuO NMs plays an important role in the bactericidal

effect and thus the plate-like HYD 150 showed more powerful effect. Secondly, the oxidative stress reported based on the elevated reactive oxygen species (such as  $\text{HO}^{\bullet}$ ,  $\text{O}_2^{\bullet 2-}$ ,  $\text{HO}^{2\bullet -}$  and  $\text{H}_2\text{O}_2$ ) levels. As noted in Fig. 3.49, both *S. iniae* (Gram positive) and *E. coli* (Gram negative) bacteria were showed significant elevation in the ROS production with increasing concentrations of CuO NMs. However, the ROS production was lower than Ag NMs. Previous reports on variety of nanoparticles including metal oxide particles induced ROS as one of the basic mechanism of cytotoxicity [110]. Metals including iron (Fe), copper (Cu), chromium (Cr), vanadium (V), and silica (Si) are involved in ROS generation via mechanisms such as Haber-Weiss and Fenton-type reactions [111]. The ROS are either directly bound to the NMs surface or may be generated as free entities in an aqueous suspension [112]. Dissolution of NMs and subsequent release of metal ions can enhance the ROS response [61]. Thirdly, release of copper  $2+$  ions subsequently bind with DNA molecules and disorder DNA strands and eventually affect the biochemical processes [113]. It was confirmed by the ICP-OES analysis, the amount of copper ion released from CuO NMs in *E. coli* and *S. iniae* bacterial cultures are listed in Table 9. As a general understanding that the supernatant would contain only dissolved  $\text{Cu}^{2+}$  whereas the pellet might consist of CuO NMs in addition to  $\text{Cu}^{2+}$ . It can clearly be seen that presence of  $\text{Cu}^{2+}$  in HYD 150 is higher than other CuO NMs in both tested bacterial cultures and the bacterial controls. Considering all the above factors, the bactericidal activity by the CuO NMs should be the combined effect, exact mechanism of which needs further understanding.

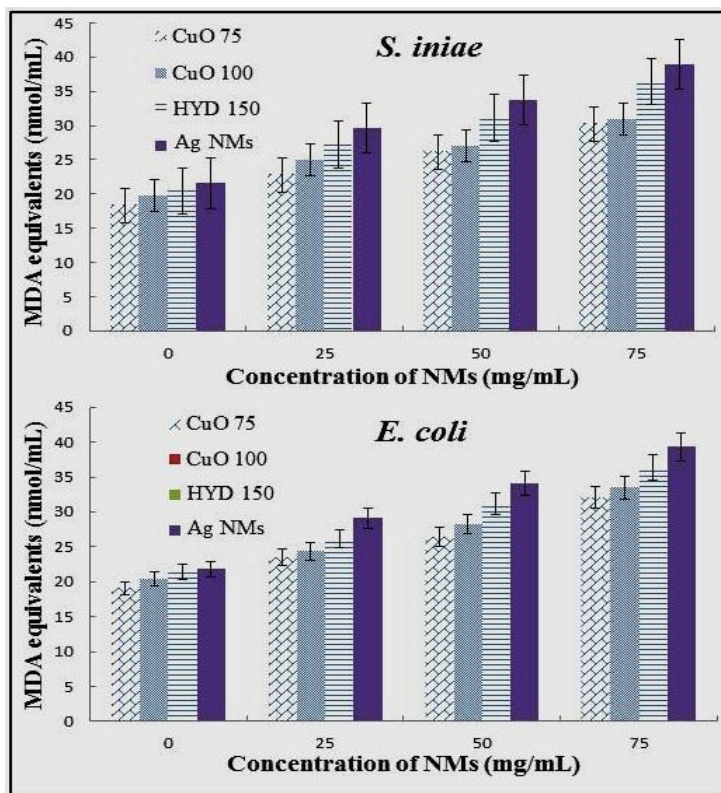


**Figure 3.49** Bar charts show the trends of MDA equivalents with increasing concentration of CuO NMs.

**Table 9.** Copper ions measurement in CuO NMs treated bacterial cultures using ICP-OES .

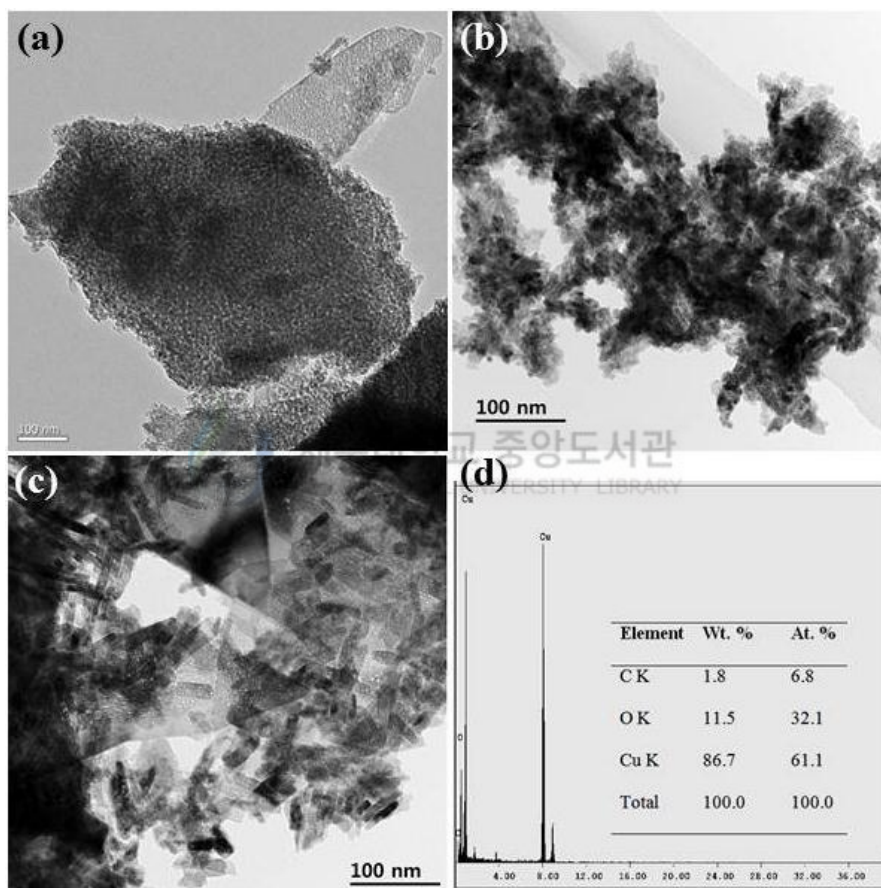
Bacterial medium	Samples	Amount of copper ions (ppm)	
		Pellet	Supernatant
<i>S. iniae</i>	CuO 75	38.17	20.54
	CuO 100	22.51	32.13
	HYD 150	46.33	39.70
	-	0.03	0.96
<i>E. coli</i>	CuO 75	15.00	19.51
	CuO 100	21.37	28.18
	HYD 150	40.56	37.98
	-	0.04	0.52

*In this study, grain-like, needle-like and plate-like CuO nanomaterials were synthesized by different but simple experimental procedure. The prepared nanomaterials exhibit high purity and crystallinity. The stability of the samples was confirmed by the zeta potential analysis. The shape dependent anti-bacterial property of the prepared samples were tested against E. coli, S. iniae, S. parauberis and V. anguillarum by disc diffusion assay and MIC assay. Among the bacteria tested, E.coli and S. iniae were found the most susceptible to CuO NMs. Comparing the shape dependent performance, CuO prepared through hydrothermal method exhibited highest activity than the samples prepared through co-precipitation routes. The increase in the activity of hydrothermally synthesized plate shaped NMs may due to its morphology dependent interaction with the bacterial cell wall, stress-related damage and the release of Cu<sup>2+</sup>. This would lead to protein and nucleic acid denaturation and consequent cell death. It is concluded that plate-like CuO NMs are more effective in inhibiting bacterial activity than grain-like and needle-like CuO nanomaterials.*



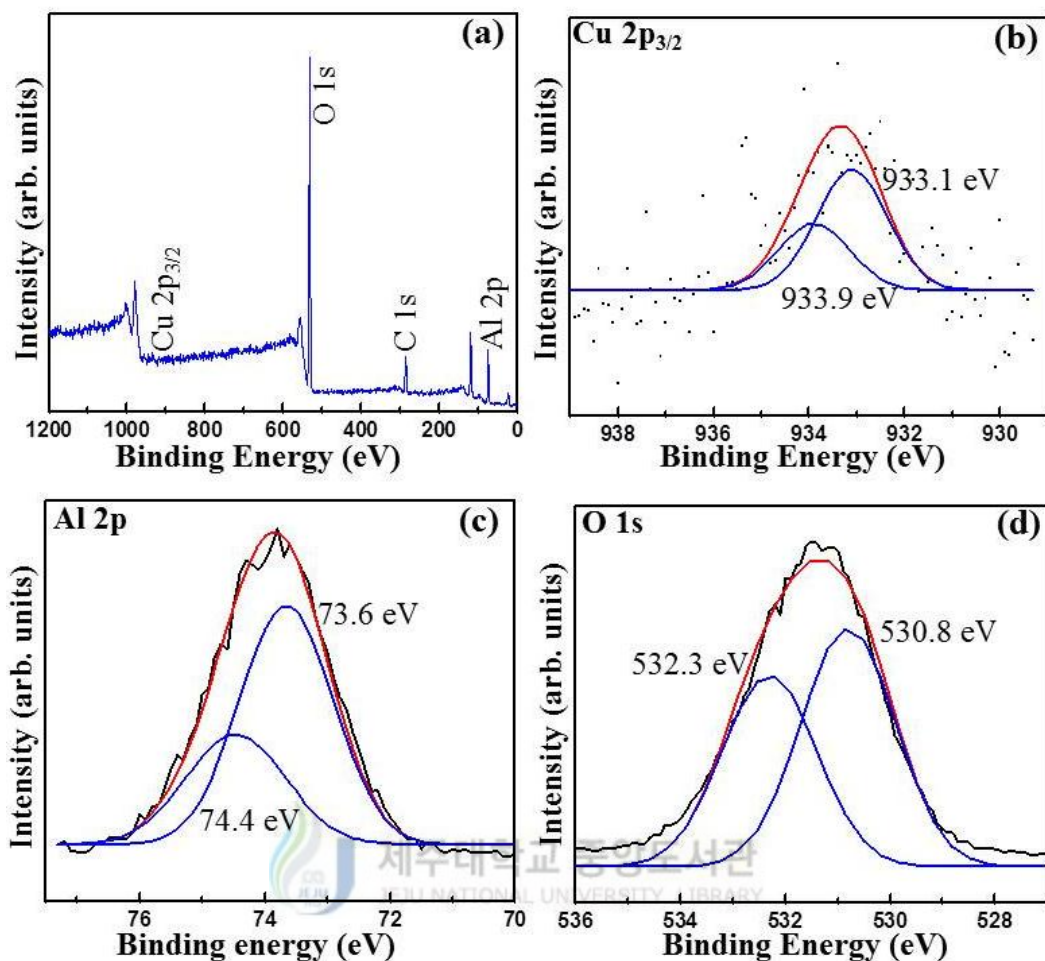
### 3.7 Shape dependent CO oxidation performance of CuO nanomaterials

Figure 3.50 (a-c) shows the TEM image of the  $\gamma$ -Al<sub>2</sub>O<sub>3</sub> support (ALVIR), CuO 75 and CuO 100 respectively. The CuO 75 and CuO 100 clearly showed the rice-grain like and nano needle-like morphologies respectively. The XPS spectra in Fig. 3.51 showed that the Cu 2p spectra mainly consisted of CuO at the binding energy values 933.9 and 933.1 eV, respectively [114,115].



**Figure 3.50** The TEM image of the  $\gamma$ -Al<sub>2</sub>O<sub>3</sub> support (a), CuO 75 (b) and CuO 100 (c). The EDX spectrum of CuO 100 with the elemental composition is shown in (d).

The aluminum 2p spectra consisted of two peaks correspond to Al<sub>2</sub>O<sub>3</sub> (Fig. 3.51 c) and the O 1s spectra also represented the Al<sub>2</sub>O<sub>3</sub> peaks (Fig. 3.51 d).



**Figure 3.51** The XPS survey spectrum (a) and high resolution core level Cu 2p (b), Al 2p (c) and O 1s (d) spectra of CuO 75/ $\gamma$ -Al<sub>2</sub>O<sub>3</sub>.

In order to investigate the shape dependent CO oxidation performance of different shape CuO nanomaterials, 1 wt.% of the synthesized CuO NMs were loaded with  $\gamma$ -Al<sub>2</sub>O<sub>3</sub> support as an ex situ basis. Exactly 10 g catalyst was loaded in a tubular reactor and the CO oxidation experiment was performed by following the same procedures explained in section 2.9.2. The CuO 75/ $\gamma$ -Al<sub>2</sub>O<sub>3</sub> showed the total CO conversion at 300 °C whereas CuO 75/ $\gamma$ -Al<sub>2</sub>O<sub>3</sub> exhibited complete conversion only at 325°C. Also, higher performance of CuO 75/ $\gamma$ -Al<sub>2</sub>O<sub>3</sub> at every experimental temperature is very clear from the fig. 3.52.

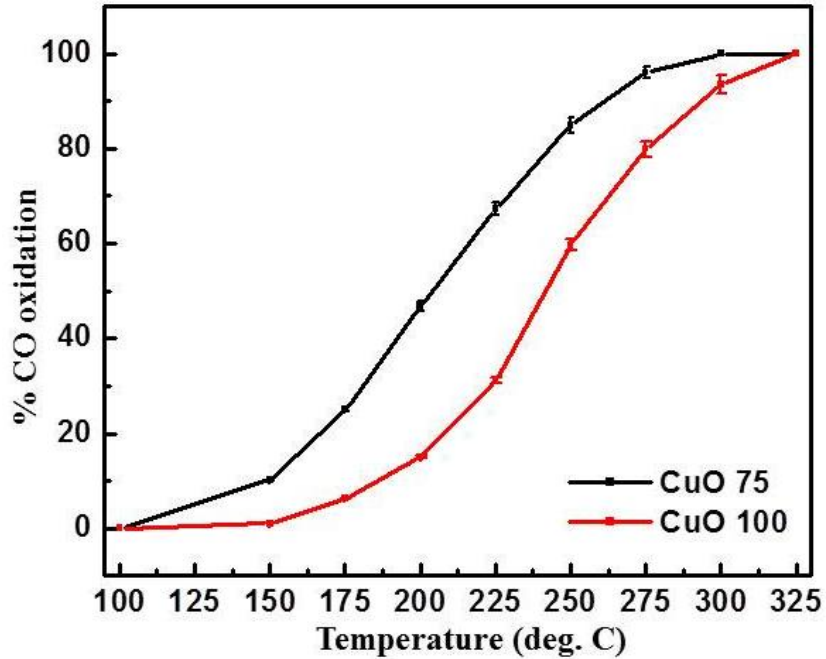


**Figure 3.52** The CO oxidation performance of CuO 75/ $\gamma$ -Al<sub>2</sub>O<sub>3</sub> and CuO 100/ $\gamma$ -Al<sub>2</sub>O<sub>3</sub>.

*This study clearly demonstrated that CuO nanomaterial shapes also an important parameter to determine the catalytic activity. This kind of shape dependent catalytic behavior of nanomaterials are nowadays an active research field, the mechanism for the improvement by shapes needs further investigations.*

### 3.8 Summary and future directions

This dissertation presented the versatility of dielectric barrier discharge plasma reactor for nanomaterials synthesis apart from its traditional usage in surface treatments and toxic gas decomposition applications. An extensive investigation to tailor the desired morphologies of nanomaterials was carried out. The plasma feed gas composition, influence of substrate materials, concentration of precursor solutions and the nature of precursor materials were found to determine the morphological structure. The investigated RuO<sub>2</sub> and CuO nanomaterials are widely used in catalysis, to prepare antibacterial products and in supercapacitor electrodes. Application using RuO<sub>2</sub> nanomaterials are very limited in literature which may be due to its expensive nature. Because of the cost associated with it, the uniqueness and the performance of RuO<sub>2</sub> could not be ruled out. On the other hand, CuO is cheap in terms of cost and also a ubiquitous candidate for many applications. In addition to the materials, size and shape dependent properties come into picture since the uniqueness in the performance strongly corroborated with this. So this research focused on the following themes. Those are (i) novel DBD plasma-mediated nanomaterials synthesis, (b) tailoring of nanomaterial morphology and (c) demonstration of the shape dependent properties towards selected functional applications. When talking about the discussed applications, CO oxidation is an environmentally important and a simple reaction to study. Photocatalysis for the degradation of dyes is also an industrially important reaction. Biological applications such as preparation and testing of antibacterial materials are rapidly growing fields of interest and also a major healthcare theme.

First chapter systematically introduced the DBD plasma, its usage for material synthesis, properties of RuO<sub>2</sub> and CuO nanomaterials and the importance of the selected applications. Significance of nanomaterials size and shapes to enhance the performances were also

emphasized. Second chapter discussed the experimental methods used for the preparation of nanomaterials, catalyst materials and the experimental procedures to carry out CO oxidation, photocatalysis and antibacterial activity. Each and every technical detail was explained in this chapter. The result and discussion part in chapter three clearly stated the observed results and reasonable explanations were given especially when dealing with the shape dependent behavior of nanomaterials. In every possible place, materials synthesis using plasma and conventional wet chemistry were equally dealt with.

Similar to the well-developed vacuum based plasma techniques such as chemical vapor deposition and laser ablation etc. used for nanomaterial preparation, DBD plasma can also be used for the above application with cost and energy efficient manner. In this dissertation, preparation of RuO<sub>2</sub> and CuO nanomaterials only was carried out. Synthesis of various metal and metal oxide nanostructures and composite materials will be carried out in future. Some of the critical issues should be sorted out in the DBD technique for material synthesis. For example, long synthesis time, plasma sustenance, handling issues remains hurdle at this stage. If the stated issues are rectified, it will be a great achievement in the future.

Regarding the application part, establishing a clear structure-property relationship is an important issue. Especially when efforts were made to explain the performance difference arising from shape effects, it was a cumbersome task to systematically prove CO oxidation results. It is due to the intricate phenomena of gas interactions with the catalyst surface. Further understanding would help to overcome the stated problem. These issues will be handled with priority in the days to come.

## References

- [1] G. Oskam, F.d. J.P. Poot, Synthesis of ZnO and TiO<sub>2</sub> nanoparticles, *J. Sol-Gel Sci. Technol.* 37 (2006) 157-160
- [2] G. Antonetti, M. Oubenali, A.M.R. Galletti, P. Serp, G. Vannucci, Novel microwave synthesis of ruthenium nanoparticles supported on carbon nanotubes active in the selective hydrogenation of p-chloronitrobenzene to p-chloroaniline, *Appl. Catal. A* 421–422 (2012) 99-107.
- [3] G. Oskam, Metal oxide nanoparticles: synthesis, characterization and application *J. Sol-Gel Sci. Technol.* 37 (2006)161-164.
- [4] W. Chen, D. Ghosh, J. Sun, M.C. Tong, F. Deng, S. Chen, Dithiocarbamate-protected ruthenium nanoparticles: Synthesis, spectroscopy, electrochemistry and STM studies, *Electrochimica Acta* 53 (2007) 1150-1156
- [5] J. Malek, A. Watanabe, T. Mitsuhashi, Crystallization kinetics of amorphous RuO<sub>2</sub> *Thermochimica Acta* 282-283 (1996) 131-142.
- [6] S. Music, S. Popovic, M. Maljkovic, K. Furic, A. Gajovic A, X-ray photoelectron spectroscopy and micro-Raman analysis of conductive RuO<sub>2</sub> thin films *Mater. Lett.* 56 (2002) 806 -811.
- [7] S. Bhaskar, P.S. Dobal, S.B. Majumder, R.S. Katiyar, X-ray photoelectron spectroscopy and micro-Raman analysis of conductive RuO<sub>2</sub> thin films, *J. Appl. Phys.* 89 (2001) 2987-2922.

- [8] D.D. Sarma, C.N.R. Rao, X-Ray photoelectron spectroscopic studies of ruthenium-oxygen surfaces, *J. Electron Spec. Rel. Phenom.* 20 (1980) 25-45.
- [9] K.S. Kim, N. Winograd, X-Ray photoelectron spectroscopic studies of ruthenium-oxygen surfaces, *J. Catal.* 35 (1974) 66-72.
- [10] M. Rajumon, M.S. Hegde, C.N.R. Rao, Adsorption of carbon monoxide on Ni/Ti and Ni/TiO<sub>2</sub> surfaces prepared *in situ* in the electron spectrometer: A combined UPS-XPS study, *Catal. Lett.* 1 (1988) 351-360.
- [11] G. Illing et al, The strong metal-support interaction (SMSI) in Pt-TiO<sub>2</sub> model catalysts. A new CO adsorption state on Pt-Ti atoms *Surf. Sci.* 206 (1988) 1-19.
- [12] C. Ocal, S. Ferrer, The strong metal-support interaction (SMSI) in Pt-TiO<sub>2</sub> model catalysts. A new CO adsorption state on Pt-Ti atoms *J. Chem. Phys.* 84 (1986) 6474.
- [13] A.J. McEvoy, W. Gissler, ESCA Spectra and Electronic Properties of Some Ruthenium Compounds, *Phys. Status. Solidi A* 69 (1982) K91-K96.
- [14] K. Winer, C.A. Colmenares, R.L. Smith, F. Wooten, Interaction of water vapor with clean and oxygen-covered uranium surfaces, *Surf. Sci.* 183 (1987) 67-99.
- [15] M. Ayyoob, M.S. Hegde, Electron spectroscopic studies of formic acid adsorption and oxidation on Cu and Ag dosed with barium, *J. Chem. Soc. Faraday Trans 1.* 82 (1986) 1651-1662.
- [16] B. Folkesson, ESCA Studies on the Charge Distribution in Some Dinitrogen Complexes of Rhenium, Iridium, Ruthenium, and Osmium, *Acta Chem. Scand.* 27 (1973) 287-302.

- [17] J.G. Serafin, C.M. Friend, Inhibition of C-H and C-O bond activation by surface oxygen: Stabilization of surface phenoxide in the reaction of phenol on oxygen-precovered Mo(110) J. Am. Chem. Soc. 111 (1989) 4233.
- [18] Shen J Y, Adnot A and Kaliaguine S , An ESCA study of the interaction of oxygen with the surface of ruthenium, App. Surf. Sci. 51 (1991) 47-60
- [19] C. Richmonds, M. Sankaran, Plasma-liquid electrochemistry: Rapid synthesis of colloidal metal nanoparticles by microplasma reduction of aqueous cations Appl. Phys. Lett. 93 (2008) 131501-131503.
- [20] N. Mayo, U. Carmi, I. Rosenthal, and R. Avni, Mechanism and kinetics of tetrachlorosilane reactions in an argon-hydrogen microwave plasma, J. Appl. Phys. 55 (1984) 55 4404.
- [21] A. Bogaerts, R. Gijbels, Effects of adding hydrogen to an argon glow discharge: overview of relevant processes and some qualitative explanations, J. Anal. At.Spectrom15 (2000) 441-449
- [22] K. Takechi, M. A. Lieberman, Effect of Ar addition to an O<sub>2</sub> plasma in an inductively coupled, traveling wave driven, large area plasma source: O<sub>2</sub>/Ar mixture plasma modeling and photoresist etching, J. Appl. Phys.90 (2001) 3205-3211
- [23] Y. Matusumi, M. Hiratani, S.Kimura, Hydrogen reduction of a RuO<sub>2</sub> electrode prepared by DC reactive sputtering, J.Mat.Sci.35 (2000) 4093-4098
- [24] A. Ananth, S. Dharaneedharan, M.S. Gandhi, M-S. Heo, Y.S. Mok, Novel RuO<sub>2</sub> nanosheets – Facile synthesis, characterization and application, Chem. Engg. J. 223 (2013) 729–736.

- [25] J.Y. Shen, A. Adnot, S. Kaliaguine, An ESCA study of the interaction of oxygen with the surface of ruthenium, *Appl. Surf. Sci.* 51 (1991) 47-60.
- [26] J. Stoch, H.Q. Dao, T. Szepe, *Bull. Polish. Acad. Sci. Chemistry* 35(1987) 387.
- [27] M.W. Cross, W.K. Varhue, Influence of Electrostatic Forces on the Growth of One-Dimensional Nanostructures, *J. Nanomaterials*. (2012) doi:10.1155/2012/105782
- [28] C. Richmonds, M. Sankaran, Plasma-liquid electrochemistry: Rapid synthesis of colloidal metal nanoparticles by microplasma reduction of aqueous cations, *Appl. Phys. Lett.* 93 (2008) 131501-131503.
- [29] K. Takechi, M.A. Lieberman, Effect of Ar addition to an O<sub>2</sub> plasma in an inductively coupled, traveling wave driven, large area plasma source: O<sub>2</sub>/Ar mixture plasma modeling and photoresist etching, *J. Appl. Phys.* 90 (2001) 3205-3211.
- [30] M.W. Cross, W.J. Varhue, D.L. Hitt, A. Adams, Control of ruthenium oxide nanorods length in reactive sputtering, *Nanotechnology* 19 (2008) 045611-045615.
- [31] B. Zhang, C. Zhang, H. He, Y. Yu, L. Wang, J. Zhang, Electrochemical Synthesis of Catalytically Active Ru/RuO<sub>2</sub> Core-Shell Nanoparticles without Stabilizer, *Chem. Mater.* 22 (2010) 4056-4061.
- [32] V.D. Patake, C.D. Lokhande, Chemical synthesis of nano-porous ruthenium oxide (RuO<sub>2</sub>) thin films for supercapacitor application, *Appl. Surf. Sci.* 254 (2008) 2820-2824.
- [33] Y. Zhao, C. Eley, J. Hu, J.S. Foord, L. Ye, H. He, S.C.E. Tsang, Shape-dependent acidity and photocatalytic activity of Nb<sub>2</sub>O<sub>5</sub> nanocrystals with an active TT (001) surface, *Angew. Chem. Int. Ed.* 51 (2012) 3846-3849.
- [34] C. Galindo, P. Jacques, A. Kalt, Photodegradation of the aminoazobenzene acid orange 52 by three advanced oxidation processes: UV/H<sub>2</sub>O<sub>2</sub>, UV/TiO<sub>2</sub> and VIS/TiO<sub>2</sub>

- Comparative mechanistic and kinetic investigations, *J. Photochem. Photobiol. A* 130 (2000) 35-47.
- [35] C. Siriwong, N. Wetchakun, B. Inceesungvorn, D. Channei, T. Samerjai, S. Phanichphant, Doped-metal oxide nanoparticles for use as photocatalysts, *Prog. Crystal Growth. Char. Mater.* 58 (2012) 145-163.
- [36] S. Music, S. Popovic, M. Maljkovic, K. Furic, A. Gajovic, Influence of synthesis procedure on the formation of  $\text{RuO}_2$ , *Mat. Lett.* 56 (2002) 806-811 .
- [37] S. Zhuiykov, In situ FTIR study of oxygen adsorption on nanostructured  $\text{RuO}_2$  thin-film electrode, *Ionics* 15 (2009) 507-512.
- [38] M. Rozenberg, A. Loewenschuss, Y. Marcus, IR spectra and hydration of short-chain polyethyleneglycols, *Spectrochimica Acta A* 54 (1998) 1819-1826.
- [39] J.Y. Shen, A. Adnot, S. Kaliaguine, An ESCA study of the interaction of oxygen with the surface of ruthenium, *Appl. Surf. Sci.* 51 (1991) 47-60.
- [40] J. Hrbek, Carbonaceous overlayers on Ru (001), *J. Vac. Sci. Technol. A* 4 (1986) 86-89.
- [41] A.J. Mc Evoy, W. Gissler, ESCA spectra and electronic properties of some ruthenium compounds, *Phys. Status Solidi A* 69 (1982) K 91- K96.
- [42] K.S. Kim, N. Vinograd, X-Ray photoelectron spectroscopic studies of ruthenium-oxygen surfaces, *J. Catal.* 35 (1974) 66-72.
- [43] N. Martensson, P.A. Malmquist, S. Svensson, E. Basilier, J.J. Pireaux, U. Gelius, S.K. Nouveau, *J. Chim.* 1 (1977) 191.

- [44] B. Zhang, C. Zhang, H.He, Y.Yu, L.Wang, J. Zhang, Electrochemical Synthesis of Catalytically Active Ru/RuO<sub>2</sub> Core-Shell Nanoparticles without Stabilizer, *Chem. Mater.* 22 (2010) 4056–4061.
- [45] K. Karthikeyan, G.Manivannan, S.J. Kim, K. Jeyasubramanian, M. Premanathan, Antibacterial activity of MgO nanoparticles based on lipid peroxidation by oxygen vacancy, *J. Nanopart. Res.* (2012) 14:1063-1072
- [46] M. Madigan, J. Martinko, Brock Biology of Microorganisms, eleventh ed., Englewood Cliffs NJ: Prentice Hall. 1019, 2005.
- [47] Z.M. Sui, X. Chen, L.Y. Wang, L.M. Xu, W.C. Zhuang, Y.C. Chai, C.J. Yang, Capping effect of CTAB on positively charged Ag nanoparticles, *Physica E*, 33 (2006) 308-314.
- [48] S. Baron, Medical Microbiology, fourth ed., Galveston: University of Texas Medical Branch 849, 1996.
- [49] J.R. Morones, J.L. Elechiguerra, A. Camacho, K. Holt, J.B. Kouri, J.T. Ramirez, M.J. Yacaman, The bactericidal effect of silver nanoparticles, *Nanotechnology* 16 (2005) 2346-2353.
- [50] W. Hu, C. Peng, W. Luo, M. Lv, X. Li, D. Li, Q. Huang, G. Fan, Graphene-based antibacterial paper, *ACS Nano*. 4 (2010) 4317-4323.
- [51] M. Premanathan, K. Karthikeyan, K. Jeyasubramanian, G. Manivannan, Selective toxicity of ZnO nanoparticles toward Gram-positive bacteria and cancer cells by apoptosis through lipid peroxidation, *Nanomedicine: NBM* 7 (2011) 184-192.
- [52] K.R. Raghupathi, R.T. Koodali, A.C. Manna, Size-Dependent Bacterial Growth Inhibition and Mechanism of Antibacterial Activity of Zinc Oxide Nanoparticles, *Langmuir* 27 (2011) 4020 – 4028.

- [53] A. Ananth, S. Dharaneedharan, M.S. Gandhi, M-S. Heo, Y.S. Mok, Novel RuO<sub>2</sub> nanosheets – Facile synthesis, characterization and application, Chem. Eng. J. 223 (2013) 729-736.
- [54] C.C. Vidyasagar, Y. Arthoba Naik, Surfactant (PEG 400) effects on crystallinity of ZnO nanoparticles, Arab. J. Chem. (2012) DOI: 10.1016/j.arabjc.2012.08.002
- [55] Y. Rozita, R. Brydson, A.J. Scott, An investigation of commercial gamma-Al<sub>2</sub>O<sub>3</sub> nanoparticles, J. Phys. Conf. series 241 (2010) 012096-012099.
- [56] B. Xu, T. Xiao, Z. Yan, X. Sun, J.Sloan, S.L. Gonazalez-Cortes, F. Alshahrani, M.L.H.Green, An investigation of commercial gamma-Al<sub>2</sub>O<sub>3</sub> nanoparticles, Microporous Mesoporous Mater. 91 (2006) 293-295.
- [57] A.B. Sifontes, M. Urbina, F. Fajardo, L. Melo, L. Gracia, M. Mediavilla, N. Carrion, J.L. Brito, P. Hernandez, R. Solano, G.Mejias, A. Quintero, Latin American Appl. Res. 40 (2010) 185-191.
- [58] S. Altwasser, R. Glaser, J. Weitkamp, Ruthenium-containing small-pore zeolites for shape-selective catalysis, Microporous Mesoporous Mater. 104 (2007) 281-288.
- [59] M.I.F. Macedo, Sol-Gel Synthesis of Transparent Alumina Gel and Pure Gamma Alumina by Urea Hydrolysis of Aluminum Nitrate, J. Sol-Gel Sci. Technol. 30 (2004) 135-140.
- [60] M.R. Karim, M.A. Rahman, M.A.J. Miah, H. Ahmed, M. Yanagisawa, M. Ito, Synthesis of  $\gamma$ -Alumina Particles and Surface Characterization, The open Colloid Sci. J.4 (2011) 32-36.

- [61] S.A. Hosseini, A. Niaei, D. Salari, Production of  $\gamma$ -Al<sub>2</sub>O<sub>3</sub> from Kaolin, *Open J. Phys. Chem.* 1 (2011) 23-27.
- [62] B.R. Strohmeier, *Surf. Sci. Spectra* 3 (1994) 141-146.
- [63] J.Y. Shen, A. Adnot, S. Kaliaguine, An ESCA study of the interaction of oxygen with the surface of ruthenium, *Appl. Surf. Sci.* 51 (1991) 47-60.
- [64] A.J. McEvoy, W. Gissler, ESCA Spectra and Electronic Properties of Some Ruthenium Compounds, *Phys. Status Solidi A* 69 (1982) K91-K96.
- [65] C. Luo, Y. Zhang, X. Zeng, Y. Zeng, Y. Wang, The role of poly(ethylene glycol) in the formation of silver nanoparticles, *J. Colloid. Inter. Sci.* 288 (2005) 444-448.
- [66] K.Niesz, P.Yang, G.A. Somorjai, Sol-gel synthesis of ordered mesoporous alumina, *Chem.Comm.* (2005) 1986-1987.
- [67] S. Royer, D. Durprez, Catalytic Oxidation of Carbon Monoxide over Transition Metal Oxides, *ChemCatChem* 3 (2011) 24-65.
- [68] G. Salek, P. Alphonse, P. Dufour, S. Guillemet-Fritsch, C. Tenailleau, Low-temperature carbon monoxide and propane total oxidation by nanocrystalline cobalt oxides, *Appl. Catal. B* 147 (2014) 1-7.
- [69] S.A.C. Carabineiro, S.S.T. Bastos, J.J.M. Orfao, M.F.R. Pereira, J.J. Delgado, J.L. Figueiredo, Carbon Monoxide Oxidation Catalysed by Exotemplated Manganese Oxides, *Catal. Lett.* 134 (2010) 217-227.
- [70] K. Reuter, C. Stampfl, M.V.G. Pirovano, M. Scheffler, Atomistic description of oxide formation on metal surfaces: the example of ruthenium, *Chem. Phys. Lett.* 352 (2002) 311-317.

- [71] H. Over, M. Muhler, A.P. Seitsonen, Comment on “CO oxidation on ruthenium: The nature of the active catalytic surface” by D.W. Goodman, C.H.F. Peden, M.S. Chen, *Surf. Sci.* 601 (2007) 5659-5662.
- [72] D.W. Goodman, C.H.F. Peden, M.S. Chen, Reply to comment on “CO oxidation on ruthenium: The nature of the active catalytic surface” by H. Over, M. Muhler, A.P. Seitsonen, *Surf. Sci.* 601 (2007) 5663-5665.
- [73] O.A. Kirichenko, E.A. Redina, N.A. Davshan, I.V. Mishin, G.I. Kapustin, T.R. Brueva, L.M. Kustov, W. Li, C.H. Kim, Preparation of alumina-supported gold-ruthenium bimetallic catalysts by redox reactions and their activity in preferential CO oxidation, *Appl. Catal. B* 134-135 (2013) 123-129.
- [74] W-P. Zhou, M. Li, C. Koenigsmann, C. Ma, S.S. Wong, R.R. Adzic, Morphology-dependent activity of Pt nanocatalysts for ethanol oxidation in acidic media: Nanowires versus nanoparticles, *Electrochim. Acta* 56 (2011) 9824-9830.
- [75] N. Lopez, T.V.W. Janssens, B.S. Clausen, Y. Xu, M. Mavrikakis, T. Bligaard, J.K. Nørskov, On the origin of the catalytic activity of gold nanoparticles for low-temperature CO oxidation, *J. Catal.* 223 (2004) 232-235.
- [76] K.M. Bratlie, H. Lee, K. Komvopoulos, P. Yang, G.A. Somorjai, Platinum Nanoparticle Shape Effects on Benzene Hydrogenation Selectivity, *Nano Lett.* 7 (2007) 3097-3101.
- [77] J. Han, H.J. Kim, S. Yoon, H. Lee, Platinum Nanoparticle Shape Effects on Benzene Hydrogenation Selectivity, *J. Mol. Catal. A* 335 (2011) 82-88.
- [78] Y.H. Kim, J.E. Park, H.C. Lee, S.H. Choi, E.D. Park, Active size-controlled Ru catalysts for selective CO oxidation in H<sub>2</sub>, *Appl. Catal. B* 127 (2012) 129-136.

- [79] D. Zhang, F. Niu, T. Yan, L. Shi, X. Du, J. Fang, Ceria nanospindles: Template-free solvothermal synthesis and shape-dependent catalytic activity, *Appl. Surf. Sci.* 257 (2011) 10161-10167.
- [80] R. Narayanan, M.A. El-Sayed, Shape-Dependent Catalytic Activity of Platinum Nanoparticles in Colloidal Solution, *Nano Lett.* 4 (2004) 1343-1348.
- [81] S. Mostafa, F. Behafarid, J.R. Croy, L.K. Ono, L. Li, J.C. Yang, A.I. Frenkel, B.R. Cuenya, Shape-Dependent Catalytic Properties of Pt Nanoparticles, *J. Am. Chem. Soc.* 132 (2010) 15714-15719.
- [82] R. Lanza, S.G. Jaras, P. Canbu, Partial oxidation of methane over supported ruthenium catalysts, *Appl. Catal. A* 325 (2007) 57-67.
- [83] L. Ma, D. He, Hydrogenolysis of Glycerol to Propanediols Over Highly Active Ru–Re Bimetallic Catalysts, *Top. Catal.* 52 (2009) 834-844.
- [84] P. Betancourt, A. Rives, R. Hubaut, C.E. Scott, J. Goldwasser, A study of the ruthenium–alumina system, *Appl. Catal. A* 170 (1998) 307-314.
- [85] L.P. Bevy (Ed.), *Leading edge catalysis research*, first ed., Nova science publishers, Inc. New York, 2005, pp. 116-117.
- [86] M.R. Johan, M.S.M. Suan, N.L. Hawari, and H.A. Ching, Annealing effects on the properties of copper oxide thin films prepared by chemical deposition, *I. J. Electrochem. Sci.* 6 (2011) 6094-6104.
- [87] A. Ananth, S. Dharaneedharan, M.S. Gandhi, M-S. Heo, and Y.S. Mok, Novel RuO<sub>2</sub> nanosheets – Facile synthesis, characterization and application, *Chem. Eng. J.* 223 (2013) 729-736.

- [88] L. Pan, and Z. Zhang, Preparation, electrocatalytic and photocatalytic performances of nanoscaled CuO/Co<sub>3</sub>O<sub>4</sub> composite oxides, *J. Mater. Sci.:Mater Electron.* 21 (2010) 1262-1269.
- [89] H. Kidowaki, T. Oku, T. Akiyama, A. Suzuki, B. Jeyadevan, and J. Cuya, Fabrication and Characterization of CuO-based Solar Cells, *J. Mater. Sci. Res.* 1 (2002) 138-143.
- [90] Y. Li, P. Kuai, P. Huo, and C-J. Liu, Fabrication of CuO nanofibers via the plasma decomposition of Cu(OH)<sub>2</sub>, *Mater. Lett.* 63 (2009) 188-190.
- [91] M. Estruga, A. Roig, C. Domingo, J.A. Ayllon, Solution-processable carboxylate-capped CuO nanoparticles obtained by a simple solventless method, *J. Nanopart. Res.* 14 (2012) 1053-1061
- [92] J. Wang, S. He, Z. Li, X. Jing, M. Zhang, Z. Jiang, Synthesis of chrysalis-like CuO nanocrystals and their catalytic activity in the thermal decomposition of ammonium perchlorate, *J. Chem. Sci.* 121 (2009) 1077-1081.
- [93] H. Wang, J-Z. Xu, J-J. Zhu, H-Y. Chen, Preparation of CuO nanoparticles by microwave irradiation, *J. Cryst. Growth* 244 (2002) 88-94.
- [94] M.A. Siddiqui, H.A. Alhadlaq, J. Ahmad, A.A. Al-Khedhairi, J. Musarrat, M. Ahamed, Copper oxide nanoparticles induced mitochondria mediated apoptosis in human hepatocarcinoma cells, *PLOS ONE* 8 (2013)1-9.
- [95] J. Zhi-Ang, C. Jiang-Tao, W. Jun, Z. Ren-Fu, Y. De, Z. Fei, Y. Peng-Xun, CuO nanosheets synthesized by hydrothermal process, *Chin. Phys. Lett.* 26 (2009) 086202-086204.
- [96] J.G. Zhao, S.J. Liu, S.H. Yang, S.G. Yang, Hydrothermal synthesis and ferromagnetism of CuO nanosheets, *Appl. Surf. Sci.* 257 (2011) 9678-9681.

- [97] S. Krishnan, A.S.M.A. Haseeb, M.R. Johan, Synthesis and growth kinetics of spindly CuO nanocrystals via pulsed wire explosion in liquid medium, *J. Nanopart. Res.* 15 (2013) 1410-1418.
- [98] M. Cao, Y. Wang, C. Guo, Y. Qi, C. Hu, E. Wang, A simple route towards CuO nanowires and nanorods, *J. Nanosci. Nanotechnol.* 4 (2004) 824-828.
- [99] A.S. Ethiraj, D.J. Kang, Synthesis and characterization of CuO nanowires by a simple wet chemical method, *Nanoscale Res. Lett.* 7 (2012) 70-74
- [100] Y. Zou, Y. Li, N. Zhang, X. Liu, Flower-like CuO synthesized by CTAB-assisted hydrothermal method, *Bull. Mater. Sci.* 34 (2011) 967-971.
- [101] V.V.T. Padil, M. Cernik, Green synthesis of copper oxide nanoparticles using gum karaya as a biotemplate and their antibacterial application, *Inter. J. Nanomedicine* 8 (2013) 889-898.
- [102] M. Huang, Y. Zhang, F. Li, Z. Wang, Alamusi, N. Hu, Z. Wen, Q. Liu, Merging of Kirkendall Growth and Ostwald Ripening: CuO@MnO<sub>2</sub> Core-shell Architectures for Asymmetric Supercapacitors, *Scientific Reports* 4 (2014) 4518-4526.
- [103] S.R. Ryu, I. Noda, Y.M. Jung, Relationship between Infrared Peak Maximum Position and Molecular Interactions, *Bull. Korean. Chem. Soc.* 32 (2011) 4011-4015.
- [104] J. Haber, T. Machej, L. Ungier, J. Ziolkowski, ESCA studies of copper oxides and copper molybdates, *J. Solid State Chem.* 25 (1978) 207-218.
- [105] N.S. McIntyre, S. Sunder, D.W. Shoemith, F.W. Stanchell, Chemical information from XPS—applications to the analysis of electrode surfaces, *J. Vac. Sci. Technol.* 18 (1981) 714 .
- [106] T. Nakamura, H. Tomizuka, M. Takahashi, T. Hoshi, *J. Surf. Sci. Soc. Jpn.* 16 (1995) 515.

- [107] V.D. Borman, E.P. Gusev, Y.Y. Lebedinski, V.I. Troyan, Mechanism of submonolayer oxide formation on silicon surfaces upon thermal oxidation, *Phys. Rev. B* 49 (1994) 5415-5424.
- [108] A. Azam, A.S. Ahmed, M.Oves, M.S. Khan, A.Memic, Size-dependent antimicrobial properties of CuO nanoparticles against Gram-positive and -negative bacterial strains, *Inter. J. Nanomed.* 7 (2012) 3527-3535.
- [109] H. Pang, F. Gao, Q. Lu, Morphology effect on antibacterial activity of cuprous oxide, *Chem. Commun.* (2009) 1076-1078.
- [110] L. Risom, P. Møller, and S. Loft, Oxidative stress-induced DNA damage by particulate air pollution, *Mutation Res.* 592 (2005), 119–137.
- [111] A. M. Knaapen, P. J. A. Borm, C. Albrecht, and R. P. F. Schins, Inhaled particles and lung cancer, part A: mechanisms, *Int. J. Cancer*, 109 (2004), 799–809.
- [112] B. Fubini and A. Hubbard, Reactive oxygen species (ROS) and reactive nitrogen species (RNS) generation by silica in inflammation and fibrosis, *Free Radical Biol. Med.* 34 (2003) 1507–1516.
- [113] J-H. Kim, H.Cho, S-E. Ryu, M-U. Choi, Effects of Metal Ions on the Activity of Protein Tyrosine Phosphatase VHR: Highly Potent and Reversible Oxidative Inactivation by  $\text{Cu}^{2+}$  Ion, *Arch. Biochem. Biophys.* 382 (2000) 72-80.
- [114] N.S. McIntyre, S.Sunder, D.W. Shoesmith, F.W. Stanchell, *J. Vac. Sci. Technol.* 18 (1981) 714.
- [115] A. Gauzzi, H.J. Mathieu, J.H. James, B. Kellett, AES, XPS and SIMS characterization of  $\text{YBa}_2\text{Cu}_3\text{O}_7$  superconducting high  $T_c$  thin films, *Vacuum* 41 (1990) 870-874.

## CHAPTER IV APPENDICES

### 4.1 List of symbols or abbreviations used

FESEM- Field emission scanning electron microscopy

HRTEM-High Resolution transmission electron microscopy

FTIR-Fourier transform infrared

XRD- X-ray diffraction

UV-Vis- Ultraviolet visible

EDX- Energy dispersive x-ray

XPS- X-ray photoelectron spectroscopy

CO- Carbon monoxide

PEG- Polyethylene glycol

RuO<sub>2</sub>- Ruthenium dioxide

CuO- Copper (II) oxide (or Copper oxide)

Al<sub>2</sub>O<sub>3</sub>- Aluminum oxide (or alumina)

MFC- Mass flow controller

SP- Spherical shape

SH- Sheet-like

NM- Nanomaterials

NP- Nanoparticles

NR- Nanorods

RAWOS- Ruthenium oxide supported on alumina prepared in the absence of stabilizer

RAWS- Ruthenium oxide supported on alumina prepared in the presence of stabilizer

ALVIR- Pure alumina

CuO 75 – Copper oxide prepared at 75 °C temperature

CuO 100 – Copper oxide prepared at 100 °C temperature

## 4.2 Calculations used

1. Prepare 1 wt.% RuO<sub>2</sub> loaded in 10 g γ-Al<sub>2</sub>O<sub>3</sub>.

Solution:

$$1 \text{ wt.\% RuO}_2 = 1\text{g}/100 \text{ g} = 0.1 \text{ g RuO}_2$$

$$\text{Required amount of } \gamma\text{-Al}_2\text{O}_3 = 10 - 0.1 = 9.9 \text{ g}$$

To prepare RuO<sub>2</sub> from RuCl<sub>3</sub>:

$$\text{Molecular weight of RuO}_2 = 133 \text{ g mol}^{-1}.$$

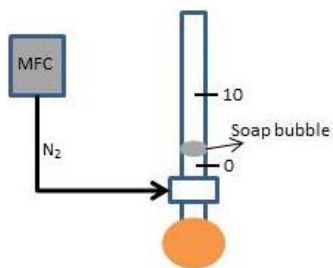
$$0.1\text{g} [1 \text{ mol RuO}_2/133 \text{ g}] = 7.518 \times 10^{-4} \text{ mol}$$

$$7.518 \times 10^{-4} \text{ mol} [207.4 \text{ g}/1 \text{ mol RuCl}_3] = 0.16 \text{ g RuCl}_3$$

So mix 0.16 g RuCl<sub>3</sub> in 9.9 g γ-Al<sub>2</sub>O<sub>3</sub>

2. Calibrate the given mass flow controller for 10 sccm N<sub>2</sub> gas flow

Solution:



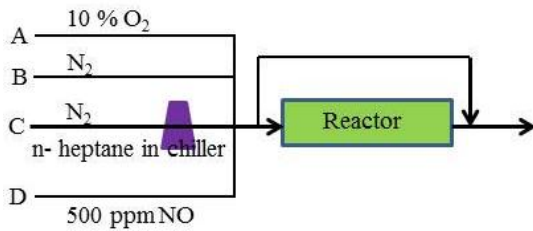
1. First see the total flow (if 200 sccm), then set in the controller 200 sccm in the corresponding gas channel and correct zeroing.

2. Set the MFC value at 10 sccm and calculate the time taken to complete 10 cc in a manual flow calibrator. If it takes 80 seconds then the actual flow is = vol/time = [10 cc/80 sec]\* [60 sec/1 min]=7.5 cc/min

3. To fix 10 sccm flow: 7.5/10 cc=10/x; **x=13.3 sccm**

(Note: To measure flow > 1 L/ min, use bigger calibrator and find out the time to fill 1 L first. Do it reversely as above).

3. NO<sub>x</sub> removal calculations: Find out the flow rates for the given variables in the figure.



Formula of n-heptane: C<sub>7</sub>H<sub>14</sub>

We need C<sub>1</sub>/NO=6 therefore,

$$7C_1H_{14}/500 \text{ ppm}=6$$

Net NO flow= 430 ppm

A: O<sub>2</sub> flow calculation:

$$1 * A = 1000 * 0.1 ; A=100 \text{ sccm}$$

Solution:

[LHS: what we have (100% pure O<sub>2</sub>); RHS = what we want (10% O<sub>2</sub> in 1000 mL)]

(Note: Sometime we need to convert % to ppm, then multiply % with 10000)

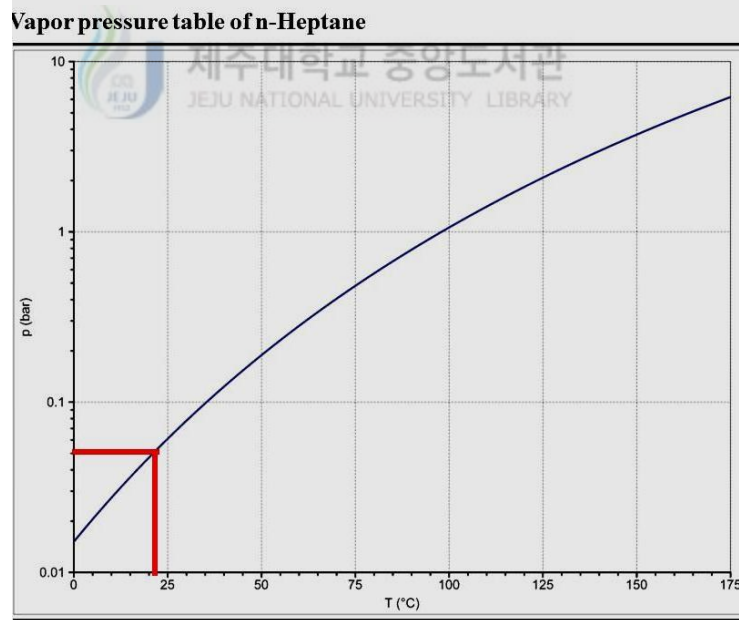
D: NO flow calculation:

$$0.05 * D = 1000 * 500 \times 10^{-6} ; D=8.6 \text{ sccm}$$

(Note: The NO cylinder contains only 5 % NO and remaining N<sub>2</sub>)

C: N<sub>2</sub>+heptane flow calculation:

It is planned to allow 5 % heptane as a reductant to the reaction.



To adjust 5%, we should check with the vapor pressure table of n-heptane to find out the temperature in 1 atm pressure.

$$x/760 \text{ mm Hg} = 0.05; x = 38 \text{ mm Hg or } 0.05 \text{ bar}$$

Required temperature to obtain 0.05 bar is 22 deg.

(always take x bar/1bar as a basis)

0.05 bar \*D=1000\*500\*10<sup>-6</sup>: D=10 sccm.

B: Remaining N<sub>2</sub> flow calculation:

B= 1000-(100+8.6+10)=881.4 sccm.

4. If 5 vol. % water is used in 1 L total flow, calculate the MFC flow rate.

Solution:

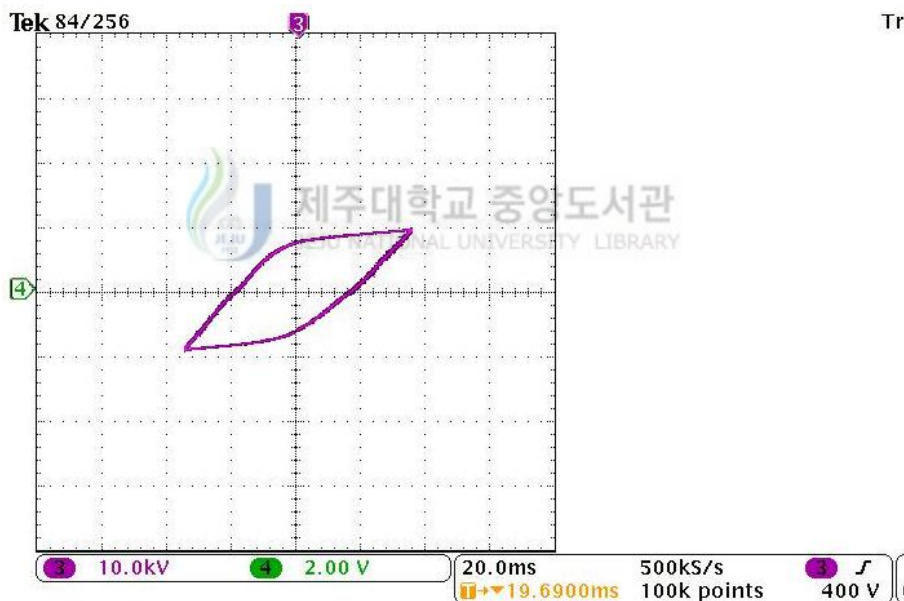
$x/760 \text{ mm Hg} = 0.05$ ;  $x = 38 \text{ mm Hg}$  or 0.05 bar

Required temperature to obtain 0.05 bar is 33 deg.

(always take  $x \text{ bar}/1\text{bar}$  as a basis)

0.05 bar\*a=1000\*5% : D=1000 sccm.

5. Calculate the actual plasma discharge power in the following oscillogram.



Total power = X axis \* Y axis \* frequency

$$= [(10 \cdot 10^3 \text{ V}) \cdot 8] \cdot [(2 \text{ V} \cdot 8)] \cdot 400 \cdot 10^{-6} \text{ S}^{-1}$$

$$= 512 \text{ W}$$

The paper weight correspond to the whole region = 1.6598g

Paper weight of the plasma region= 0.0855g

Therefore, actual discharge power is 512W:1.6598g= x:0.0855g; **x=26.37 W**

(same problem will also be solved by taking the area of the total power and parallelogram area; Just replace area instead of weight)

#### 4.3 List of publications in international journals

1. **A. Ananth**, S. Dharaneedharan, M.S. Gandhi, M-S. Heo, Y.S. Mok, Novel RuO<sub>2</sub> nanosheets – Facile synthesis, characterization and application, *Chem. Eng. J* 223 (2013) 729–736.
2. **A. Ananth**, M.S. Gandhi, Y.S. Mok, Dielectric barrier discharge (DBD) plasma reactor-An efficient tool to prepare novel RuO<sub>2</sub> nanorods, *J. Phys. D: Appl. Phys.* 46 (2013) 155202-155209.
3. M. S. Gandhi, **A. Ananth**, Y.S. Mok, J-I. Song, K-H. Park, Time dependence of ethylene decomposition and byproducts formation in a continuous flow dielectric-packed plasma reactor, *Chemosphere* 91 (2013) 685-691.
4. **A. Ananth**, Y.S. Mok, Synthesis of RuO<sub>2</sub> nanomaterials under dielectric barrier discharge plasma at atmospheric pressure - Influence of substrates on the morphology and application, *Chem. Eng. J.* 239 (2014) 290–298.
5. M. S. Gandhi, **A. Ananth**, Y. S. Mok, J-I. Song, K-H. Park, Effect of porosity of a-alumina on non-thermal plasma decomposition of ethylene in a dielectric-packed bed Reactor, *Res. Chem. Intermed.* 40 (2014) 1483-1493.
6. **A. Ananth**, G. Arthanareeswaran, A.F. Ismail, Y.S. Mok, T. Matsura, Effect of bio-mediated route synthesized silver nanoparticles for modification of Polyethersulfone membranes, *Colloids Surf. A* 451 (2014) 151-160.
7. **A. Ananth**, G. Arthanareeswaran, Y.S. Mok, Effects of in-situ and ex-situ formation of Silica nanoparticles on Polyethersulfone membranes, *Polymer bulletin.* (2014) DOI 10.1007/s00289-014-1226-y
8. K. Krishnamoorthy, **A. Ananth**, Y.S. Mok, S.J. Kim, Plasma assisted synthesis of graphene nanosheets and their supercapacitor applications, *Sci. Adv. Mater.* 6, (2014) 349-353.
9. K. Thiyagarajan, **A. Ananth**, B. Saravanakumar, Y.S. Mok, Sang-Jae Kim, Plasma-induced photo response in few layer graphene, *Carbon*, 73 (2014) 25-33.
10. **A. Ananth**, Y.S. Mok, Dielectric Barrier Discharge Plasma-mediated Synthesis of Several Oxide Nanomaterials and Its Characterization, *Powder Technol.* 269 (2015) 259-266.

11. **A. Ananth**, S. Dharaneedharan, M-S. Heo, Y.S. Mok, Copper oxide nanomaterials: Synthesis, characterization and structure-specific antibacterial performance, *Chem. Eng. J.* 262 (2015) 179-188.

#### **Manuscripts under review**

1. A. Ananth, D. H. Gregory, Y.S. Mok, Synthesis, characterization and shape dependent catalytic CO oxidation performance of ruthenium oxide nanomaterials: Influence of polymer surfactant (under review)
2. A. Ananth, Y.S. Mok, Dielectric barrier discharge (DBD) plasma assisted synthesis of Ag<sub>2</sub>O nanomaterials and Ag<sub>2</sub>O/RuO<sub>2</sub> nanocomposite (under review)

#### **4.4 Patent/s**

1. Method for preparing linear metal nanoparticles, Korean patent No. 1014065880000 (June 03, 2014).



#### 4.5 Contribution to international conferences

1. Oral presentation: **A. Ananth**, K. Thiyagarajan, G. Arthanareeswaran, Y.S. Mok, “ Synthesis and Characterization of Polymeric/Activated Carbon Membranes” and their Utilization in the Treatment of Polluted Water, International Conference On Recycling and Reuse 2012 June 4-6, 2012. (R&R, 2012), Istanbul, Turkey.
2. **A. Ananth**, Y.S. Mok, Plasma treatment studies of RuO<sub>2</sub>/CuO bimetallic nanoparticles: Probing the modifications on structure and chemistry for the possible application in supercapacitor, The 4<sup>th</sup> international conference on microelectronics and plasma technology, (ICMAP 2012), July 4-6, 2012. Ramada plaza Jeju Hotel, Korea.
3. **A. Ananth**, Y.S. Mok, Synthesis, Characterization and CO oxidation application of RuO<sub>2</sub>/  $\gamma$ -Al<sub>2</sub>O<sub>3</sub>catalyst, Jeju national university-Nagasaki university joint symposium on science and technology, June 2013, Jeju National University, Korea.
4. J. O. Jo, Y.S. Mok, **A. Ananth**, Synthesis of spherical and sheet-like RuO<sub>2</sub> nanomaterials under dielectric barrier discharge plasma and their photocatalytic properties, KICHe meeting in fall, October 2013, Daegu. Korea.
5. **A. Ananth**, Y.S. Mok, Dielectric barrier discharge (DBD) plasma mediated synthesis of few oxide nanomaterials and their characterization, 8<sup>th</sup> International conference on Reactive Plasmas/31<sup>st</sup> Symposium on Plasma processing, Feb.4-7,2014, Fukuoka International Congress Center, Fukuoka, Japan.
6. **A. Ananth**, Y.S. Mok, Shape dependent catalytic CO oxidation performance of ruthenium oxide nanomaterials, KICHe, Spring meeting, April 23-25, 2014, Changwon, Korea.
7. **A. Ananth**, Y.S. Mok, Investigation on the NO reduction performance of copper oxide nanocatalysts, 49<sup>th</sup> KSIEC meeting, April30-May 2, 2014, The Suites hotel Jeju/International convention centre, Korea.
8. Oral presentation: **A. Ananth**, Y.S. Mok, Dielectric barrier discharge (DBD) plasma assisted synthesis of silver oxide and ruthenium oxide nanomaterials, 2014 International Symposium on Plasmas for Catalyses and Energy Materials (ISPCEM-2014) September 13-16, 2014; Tianjin, China.

## 4.6 Memories



Photograph taken in front of a Buddha temple in Japan during ICRP 8 conf. 2014.



Photograph of a Buddha temple in Fukuoka, Japan. 2014.



With lab members in BEXCO, Busan, Korea. 2013.



With prof. Dr. Y.S. Mok in Istanbul university, Turkey. 2012



Oral presentation at ISPCEM 2014, Tianjin university, China.



Photograph of Tiananmen square, Beijing. 2014.

#### 4.7 About the author



Mr. A. Ananth was born on May 27<sup>th</sup> 1985 to Mr. Antony-Mrs. Regina Mary in the Kamala puram village, Dindigul district, Tamil Nadu state, India. He received his B.Sc., degree in physics from Bharathidasan University, Tiruchirappalli and M.Sc., degree also in physics from Madras University, Chennai. He worked in a private power plant company in Chennai for a year and later joined in Anna University to do M. Tech. in Nanoscience and technology program. He did a research project in the area of nanocomposite polymer membranes

aiming at water treatment and separation of protein molecules. After the course, he got a post graduate trainee and later as a project assistant opportunity in National aerospace laboratories, Bangalore. His main work was involved in the preparation of solar selective coatings and the formation of plasma assisted superhydrophobic surfaces by employing DC magnetron sputtering technique there. Then he arrived to Jeju National University, Korea for Ph. D program. There, the main research involved in the preparation nanomaterials by DBD plasma assistance and utilization of the materials for applications related to catalysis and biology. He has published several research articles. For contacts, the author can be reached at [sebastiananath@gmail.com](mailto:sebastiananath@gmail.com) and face book identification name Sebastian Ananth.